Geochemistry, Geophysics, Geosystems®

AGU ADVANCING EARTH AND SPACE SCIENCES

RESEARCH ARTICLE
10.1029/2024GC011541

Unveiling the Transition From Paleolake Lisan to Dead Sea Through the Analysis of Lake Paleoshorelines and Radiometric Dating of Fossil Stromatolites

Julius Jara-Muñoz[1], Amotz Agnon[2], Jens Fohlmeister[3], Sara Tomás[4], Jürgen Mey[5], Norbert Frank[6], Birgit Schröder[7], Andrea Schröder-Ritzrau[6], Yannick Garcin[8], Yaniv Darvasi[2], Daniel Melnick[9], Maria Mutti[10], and Manfred R. Strecker[10]

[1]Institute of Geo- and Environmental Research, Hochschule Biberach, Biberach an der Riß, Germany, [2]Institute of Earth Sciences, Hebrew University of Jerusalem, Jerusalem, Israel, [3]Federal Office for Radiation Protection, Berlin, Germany, [4]Department of Geology, Universitat Autònoma de Barcelona, Bellaterra (Barcelona), Spain, [5]Institute of Environmental Science and Geography, University of Potsdam, Potsdam, Germany, [6]Institute of Environmental Physics, University of Heidelberg, Heidelberg, Germany, [7]German Research Centre for Geosciences (GFZ), Climate Dynamics and Landscape Evolution, Potsdam, Germany, [8]Aix Marseille University, CNRS, IRD, INRAE, CEREGE, Aix-en-Provence, France, [9]Instituto de Ciencias de la Tierra, Universidad Austral de Chile, Valdivia, Chile, [10]Institute of Geosciences, University of Potsdam, Potsdam, Germany

Abstract To date, the most complete paleolake-level reconstructions for the late Pleistocene water bodies that once occupied the Dead Sea depression have been based on the combination of dating of lake sediments and terrestrial materials. However, despite these major accomplishments, there is still limited spatial control regarding the water levels, suggesting some degree of uncertainty concerning the magnitude and rate of lake-level changes. Here, we re-examine the late Pleistocene lake-level changes in the Dead Sea during the transition from paleolake Lisan to the present-day Dead Sea. We rely on systematic dating of fossil stromatolites including 84 radiocarbon and 15 U-series ages, stable-isotope measurements, paleobiology, high-resolution topography, and numerical modeling to assess lake-level changes. Our results indicate that the highstand of paleolake Lisan was of shorter duration and the transition between Lake Lisan and the Dead Sea occurred at least 5 Kyrs earlier than previously indicated. By refining the timeline and accuracy of lake-level positions during the transition paleolake Lisan—Dead Sea, our study offers new insights into the regional and local paleo-climatic conditions during the last glacial period in this region.

Plain Language Summary Index points, reflecting the unique position of the water levels in space and time, have been broadly used in marine realms to reconstruct past sea-level changes. Here we study lake-level variations using index points based on geomorphic and biological markers collected along the western and eastern coasts of the Dead Sea. Previous studies indicate that during the last glacial period (20–30 ka), the Dead Sea depression was filled by paleolake Lisan, which lasted 10 Kyrs. As it dried, dozens of paleo-shorelines remained etched in the landscape. Lake level index points estimated from 99 radiometric ages in these paleo-shorelines suggest that Lisan's highstand was shorter and the transition to the Dead Sea occurred 5 Kyrs earlier than previously thought. These novel results suggest an initial and wet period followed by drier conditions, altering the regional paleo-climatic narrative during the last glacial period.

Key Points:

- Lake paleo-shorelines and fossil stromatolites are used to reconstruct lake-level changes during the transition paleolake Lisan-Dead Sea
- Fossil stromatolites were dated using radiocarbon and U-series applying temporal and vertical corrections
- The transition between paleolake Lisan and the Dead Sea occurred ~5 Kyrs earlier than estimated by previous reconstructions

Supporting Information:

Supporting Information may be found in the online version of this article.

Correspondence to:

J. Jara-Muñoz,
jara@hochschule-bc.de

Citation:

Jara-Muñoz, J., Agnon, A., Fohlmeister, J., Tomás, S., Mey, J., Frank, N., et al. (2024). Unveiling the transition from paleolake Lisan to Dead Sea through the analysis of lake paleoshorelines and radiometric dating of fossil stromatolites. *Geochemistry, Geophysics, Geosystems*, *25*, e2024GC011541. https://doi.org/10.1029/2024GC011541

Received 5 MAR 2024
Accepted 26 JUN 2024

Author Contributions:

Conceptualization: Julius Jara-Muñoz, Amotz Agnon, Yannick Garcin, Daniel Melnick, Manfred R. Strecker
Data curation: Amotz Agnon
Formal analysis: Julius Jara-Muñoz, Jürgen Mey, Norbert Frank, Andrea Schröder-Ritzrau
Funding acquisition: Julius Jara-Muñoz, Amotz Agnon, Manfred R. Strecker

1. Introduction

The late Pleistocene and Holocene evolution of lacustrine water bodies in the Dead Sea depression has been a matter of debate over a number of decades (e.g., Bartov et al., 2002; Bookman et al., 2006; Lisker et al., 2009; Torfstein & Enzel, 2017). To date, the most complete lake-level reconstructions for the late Pleistocene have been based on the stratigraphy of lacustrine deposits exposed on the flanks of the Dead Sea depression, yielding exceptionally detailed and precise chronologies of the sediment sequences (e.g., Bartov et al., 2002; Haase-Schramm et al., 2004; Torfstein & Enzel, 2017; Torfstein, Goldstein, Kagan, & Stein, 2013). These studies have identified two main lake-level phases: Lake Lisan that involved the region between the present-day Dead Sea and Lake Kinneret (the Sea of Galilee) (Figure 1a), followed by a pronounced fall in water level and the formation of the Holocene Dead Sea after ~15 ka (Bartov et al., 2002; Torfstein & Enzel, 2017; Torfstein, Goldstein, Kagan, & Stein, 2013). However, despite these major efforts, there has only been limited spatial

Investigation: Amotz Agnon, Jens Fohlmeister, Sara Tomás, Jürgen Mey, Yannick Garcin
Methodology: Julius Jara-Muñoz, Jens Fohlmeister, Sara Tomás, Jürgen Mey, Norbert Frank, Birgit Schröder, Andrea Schröder-Ritzrau, Yannick Garcin, Yaniv Darvasi, Maria Mutti
Project administration: Julius Jara-Muñoz
Resources: Daniel Melnick, Manfred R. Strecker
Software: Julius Jara-Muñoz
Supervision: Amotz Agnon, Jens Fohlmeister, Sara Tomás, Birgit Schröder, Yannick Garcin, Daniel Melnick, Maria Mutti, Manfred R. Strecker
Validation: Jens Fohlmeister, Sara Tomás, Norbert Frank, Birgit Schröder, Andrea Schröder-Ritzrau, Yaniv Darvasi, Maria Mutti
Visualization: Julius Jara-Muñoz, Sara Tomás, Jürgen Mey, Yaniv Darvasi
Writing – original draft: Julius Jara-Muñoz
Writing – review & editing: Amotz Agnon, Jens Fohlmeister, Sara Tomás, Jürgen Mey, Norbert Frank, Birgit Schröder, Andrea Schröder-Ritzrau, Yannick Garcin, Daniel Melnick, Manfred R. Strecker

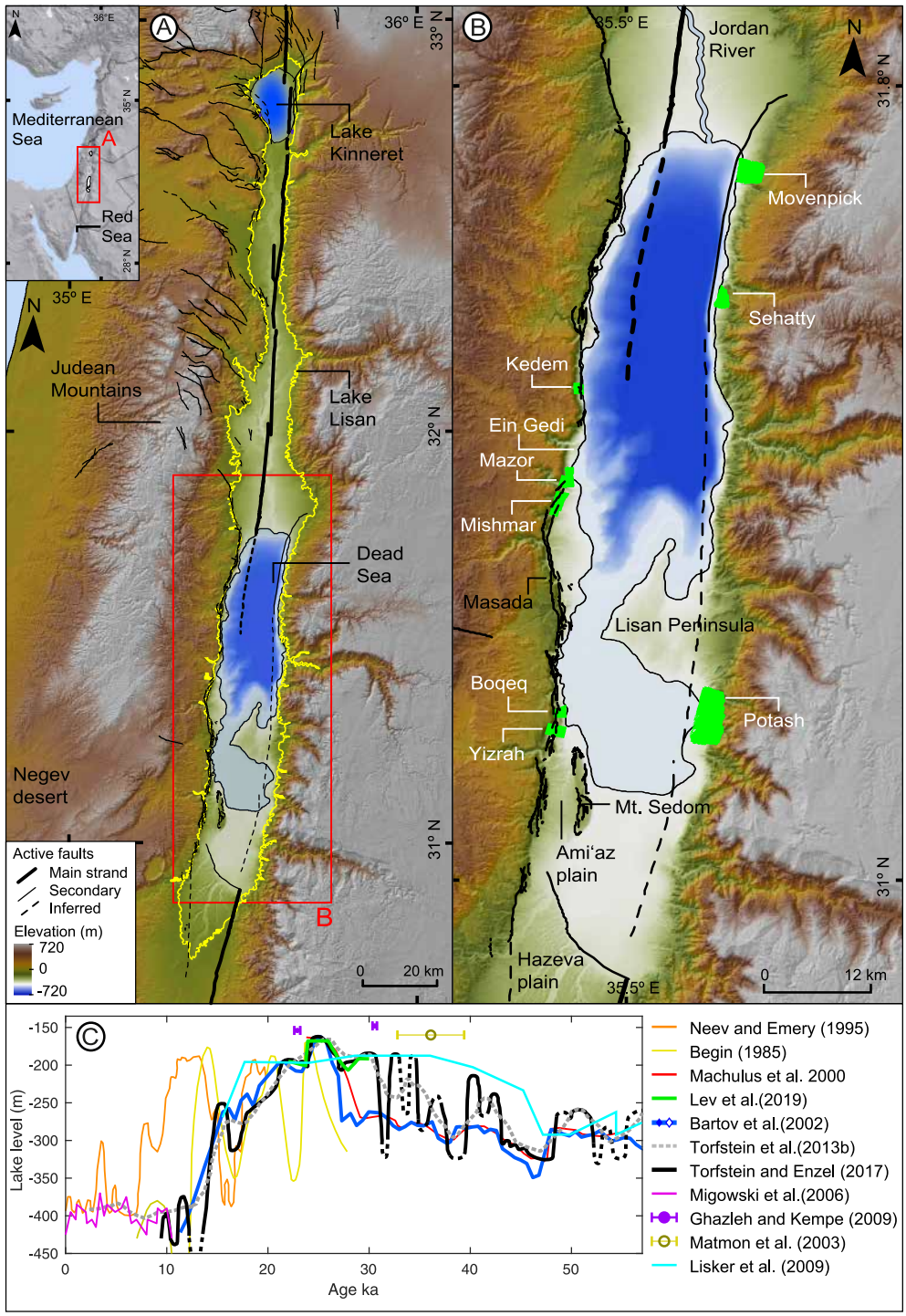

Figure 1. Location of the study area, sampling sites, and previous lake-level reconstructions. (a) Map of the Levant, the yellow line displays the extent of the paleolake Lisan during the Last glacial maximum (Torfstein, Goldstein, Kagan, Stein, & Enzel, 2013) the black lines are active faults (Sharon et al., 2018). (b) The Dead Sea. The light green patches indicate sampling and topographic survey sites. (c) Previous lake-level reconstructions. The gray dashed line is the smoothed version of the lake-level curve by Torfstein, Goldstein, Kagan, Stein, and Enzel, (2013). The black dashed line indicates approximate lake-level positions according to Torfstein and Enzel (2017). The lake-level curve of Lev et al. (2019) represents the Lake Kinneret lake-level reconstruction. ka: kiloyears ago.

control regarding the water levels during this period, more specifically during the transition between paleolake Lisan and the Dead Sea (Bartov et al., 2002; Torfstein, Goldstein, Kagan, Stein, & Enzel, 2013), resulting in considerable uncertainty concerning the magnitude and rate of lake-level changes. The importance of reconstructing the lake-level history during the transition between paleolake Lisan and the Dead Sea is important not only from a paleoclimatic perspective but also from the environmental factors that were conductive to the evolution and migration of hominids in this area (e.g., Miebach et al., 2019; Waldmann et al., 2010), and the potential feedbacks between climate-driven water levels, loading stresses and seismogenesis (e.g., Lu et al., 2021; Marco et al., 1996) among others.

Accurate lake-level reconstructions are fundamental for assessing the impact of forcing mechanisms on different processes in the Dead Sea region. However, the usefulness of such lake-level reconstructions relies on the application of systematic approaches that incorporate all of the known chronological and elevation uncertainties (e.g., Engelhart et al., 2011). In the marine realm, a number of investigations into sea-level changes have established the concept of index points, which reflect the unique position of the water level in space and time (e.g., Garrett et al., 2020; Shennan, 1986); in this context, a group of index points describes trends and patterns of water-level changes through space and time (Horton et al., 2013). These index points can be associated with markers based on geomorphic (e.g., shorelines, strandlines, terraces, etc.), biogenic (e.g., diatoms, stromatolites, mollusks, etc.), and sedimentary features (e.g., buried paleosoils, wave ripples, etc.), with each index point having a suite of vertical and temporal uncertainties that relate to the intrinsic characteristics of the markers, as derived from modern analogs. The concept of index points has also been applied in terrestrial environments to aid lake-level reconstructions (e.g., Chiba et al., 2020), allowing to consider uncertainties that are rarely integrated into these types of reconstructions.

Here we study lake-level variations within the Dead Sea depression using lake-level index points based on geomorphic and biological markers that were collected along the western and eastern coasts of the Dead Sea. We combined high-resolution topography and morphometry, radiocarbon and U-series dating, stable isotope analysis, mineralogy, paleobiology, and numerical modeling to estimate lake-level changes that occurred during the late Pleistocene, but specifically during the transition between the paleolake Lisan highstand and the Dead Sea. Our study emphasizes the importance of assessing spatial and temporal uncertainties in lake-level reconstructions using multiproxy approaches in efforts to decipher the details of lake-level and climatic changes that affected the Dead Sea depression during the late Pleistocene.

2. Lake-Level Reconstructions, Markers and Neotectonics in the Dead Sea Depression

2.1. Lake-Level Changes Within the Dead Sea Depression

The lakes that occupied the Dead Sea depression acted as "amplifier lakes" (Street-Perrott & Perrott, 1990), whose size and depth reflected the changing climatic conditions in the region (Stein, 2001). The Dead Sea depression has been occupied by a series of hypersaline terminal paleolakes since the early Pleistocene, including the lakes Amora, Samra, Lisan, and the present-day Dead Sea (Kaufman et al., 1992; Torfstein et al., 2008, 2009; Waldmann et al., 2009). During the late Pleistocene and Holocene, the Levant region and more specifically the Dead Sea depression experienced substantial changes in the amount and pattern of precipitation and runoff that governed the freshwater influx from rivers and groundwater to the Dead Sea depression (Kushnir & Stein, 2010). Changing proportions between water supply and evaporation finally controlled the amplitude of lake-level variations (Bartov et al., 2003; Enzel et al., 2003; Kushnir & Stein, 2010).

Previous reconstructions of late Pleistocene and early Holocene lake-level changes in the Dead Sea depression have yielded different interpretations regarding the evolution of the lakes that occupied the depression (Bookman et al., 2006; Neev & Emery, 1967; Stein, 2001) (Figure 1c). This resulted in the identification of high-amplitude lake-level oscillations during these periods. U-Th dating of aragonite layers in the Lisan Formation (e.g., Kaufman, 1971; Kaufman et al., 1992) has subsequently provided the highest temporal resolution for the sedimentary lacustrine sequences (Haase-Schramm et al., 2004; Machlus et al., 2000; Schramm et al., 2000; Torfstein, Goldstein, Kagan, & Stein, 2013; Torfstein et al., 2015). The lake-level reconstructions based on these ages suggest that the higher water levels in the paleolake Lisan (∼-180 masl) lasted for ∼14 Kyrs during the coldest part of the last glacial maximum (LGM) (Bartov et al., 2002; Torfstein, Goldstein, Kagan, & Stein, 2013). The transition from paleolake Lisan to the present-day Dead Sea occurred between 15 and 10 ka and was associated with a ∼200 m fall in lake level (Bartov et al., 2002, 2003; Torfstein, Goldstein, Kagan, & Stein, 2013). On

average, the early Holocene was drier than the present day (Kiro et al., 2017; Morin et al., 2019) and comprised high-frequency lake-level oscillations with a maximum amplitude of ~50 m (Migowski et al., 2006) (Figure 1c). The present-day Dead Sea lake-level is −430 masl and is rapidly declining at a rate of >1 m/yr (Lensky et al., 2005).

2.2. The Lisan Formation

The Lisan Formation is a remarkable climatic and lacustrine archive from the late Pleistocene; it consists of millimeter-scale laminations of aragonite and gypsum intercalated with silty detrital layers and thicker, coarser clastic layers of deep lacustrine and fan-delta environments (Haase-Schramm et al., 2004; Stein, 2001). The deposition of the Lisan Formation has been linked to changes in the salinity-controlled stratification of paleolake Lisan (Lazar et al., 2014; Torfstein et al., 2005). Stable stratified (meromictic) water conditions persisted during glacial periods and were characterized by high inflows and lake-level highstands; the water column was divided into a lower, dense, saline layer (hypolimnion) and an upper, less saline surface layer (epilimnion). Meromictic (stratified) water conditions were associated with authigenic aragonite precipitation, whose formation is controlled by the mixing of Ca-rich brine with bicarbonate-rich freshwater from the Jordan River and bicarbonate supply from freshwater springs (Barkan et al., 2001; Katz & Starinsky, 2009; Stein et al., 1997, 2004). In contrast, holomictic (homogeneous) water conditions led to the precipitation of gypsum and halite during arid periods and lake-level lowstands (Neugebauer et al., 2014; Stein et al., 1997; Torfstein et al., 2005). A positive water balance therefore favored meromictic conditions in which any loss by evaporation was compensated by freshwater inflow, while a negative water balance resulted in a reduced epilimnion and holomictic conditions (Stein et al., 1997; Torfstein et al., 2005, 2008). However, detailed analysis of laminated facies in the Lisan Formation suggests an apparent decoupling between the Lisan paleolake levels and the thicknesses of the detrital laminae, which may imply a transport-limited regime of sedimentation (Lu et al., 2020) or complexities not captured in previous lake-level reconstructions.

2.3. Lake-Level Markers in the Dead Sea Depression

Different approaches have been employed to reconstruct lake-level changes in the Dead Sea depression, using lake-level markers, sequence stratigraphy, or a combination of both approaches to obtain absolute and relative lake-level reconstructions (Torfstein & Enzel, 2017). Examples of former lake-level markers described in the Dead Sea depression include caves formed close to the shoreline, paleo-shorelines, and fossil stromatolites.

2.3.1. Caves

A number of authors have focused their investigations on the numerous caves exposed along the Dead Sea depression (Frumkin, 2001; Frumkin & Fischhendler, 2005; Kafri & Yechieli, 2010; Lisker et al., 2009). Lisker et al. (2009) assumed that the caves along the western escarpment of the Dead Sea were inundated or at least reached by lake waters during the paleolake Lisan highstand; these authors used the cave-elevations and the ages of fossil cave-stromatolites to reconstruct minimum lake level estimates (Figure 1c).

2.3.2. Lake Paleo-Shorelines

Lake paleo-shorelines are excellent geomorphic markers of past lake-level positions (e.g., Gilbert, 1890). Lake-shoreline morphology usually comprises a shoreline riser and a tread or platform of lower slope (Figures 2c and 2d); the intersection of the riser with the tread marks the position of the lake-level during shoreline formation (Bowman, 1971). The paleo-shorelines around the Dead Sea form a sequence of closely spaced markers that were generated over a sustained period of lake regression (Bowman, 1971; Bowman & Gross, 1992; Ghazleh & Kempe, 2009; Picard, 1943). Although the elevations and distribution of lake paleo-shorelines around the Dead Sea have been investigated for more than 100 years and have fascinated early explorers and researchers (Bartov, Bookman, & Enzel, 2006; Blanckenhorn, 1912; Bookman (Ken-Tor) et al., 2004; Bookman et al., 2014; Bowman, 1971; Bowman & Gross, 1992; Ghazleh & Kempe, 2009; Huntington, 1911; Neev & Emery, 1967; Picard, 1943), their extent and the variations in their elevations have remained ambiguous, largely due to the lack of precise paleo-shoreline sequence assessments.

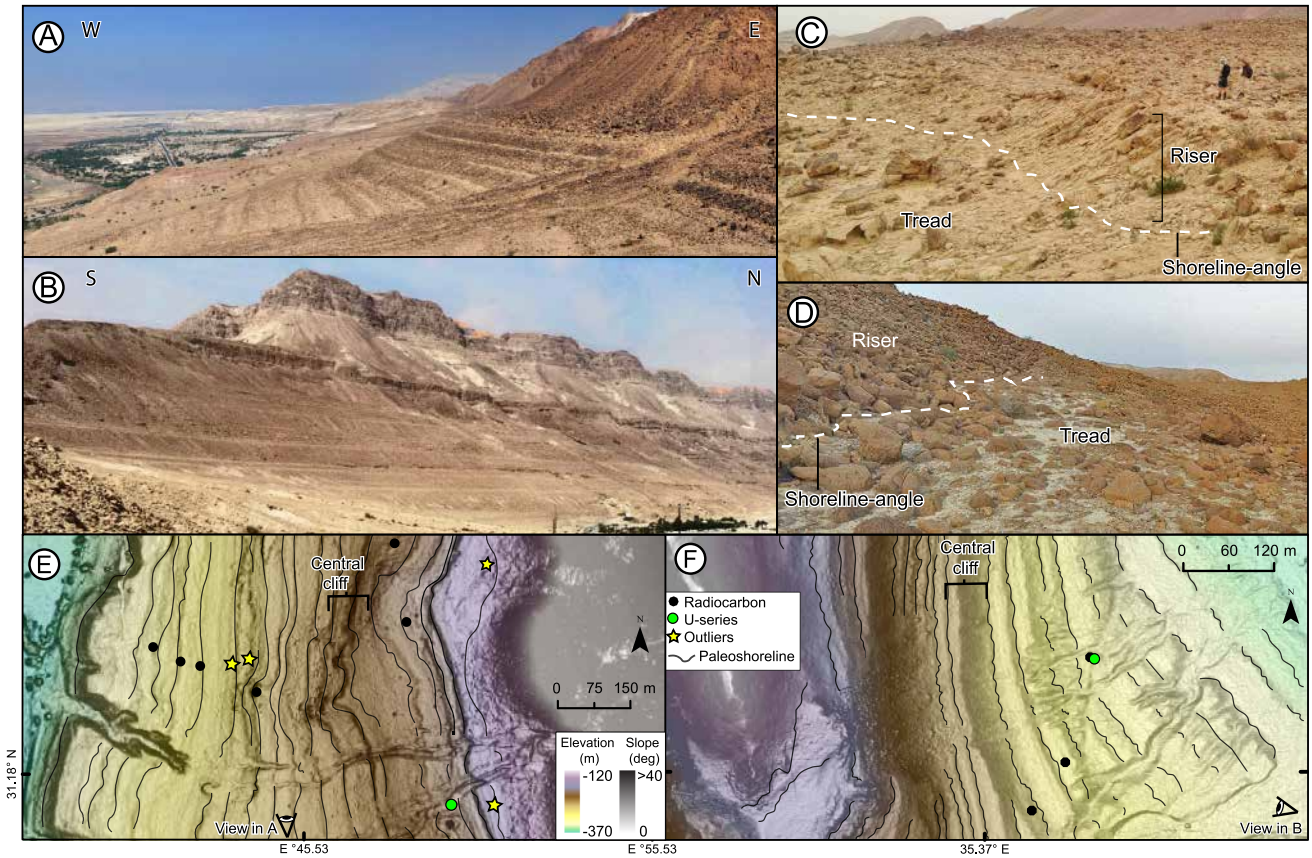

Figure 2. Dead Sea lake paleo-shorelines. (a) and (b) Sequences of lake paleo-shorelines at Potash (a) and Mazor sites (b). (c) Bedrock-carved paleo-shorelines at the Potash site. (d) Typical morphology of paleo-shorelines carved into colluvial deposits at the Mazor site. (e) and (f) High-resolution drone topography and samples collected along the transects at Potash1 (e) and Mazor-3 (f).

2.3.3. Stromatolites

Stromatolites are layered, early lithified, benthic microbial deposits formed by sediment trapping, binding and/or in situ precipitation due to the growth and metabolism of microorganisms, usually cyanobacteria (Dupraz et al., 2009; Riding, 1999; Walter, 1976). Fossil stromatolites associated with paleolake Lisan were described by Bentor and Vroman (1960), Neev and Langozky (1961), Zak (1967), Neev and Emery (1967), Buchbinder et al. (1974), Niemi (1997), Buchbinder (1981), Begin et al. (1985), and Lisker et al. (2009) and developed in lacustrine (nearshore) environments exposed along the flanks of the Dead Sea basin. Lisker et al. (2009) dated fossil cave-stromatolites, suggesting that photosynthetic bacterial growth and the formation of stromatolites may even take place within dimly lit cave environments. Although stromatolites have been described in detail in the Dead Sea, very little is known about their biotic and abiotic growth mechanisms as well as the type of microbial communities involved during their formation.

Because stromatolites usually develop in shallow-water environments, they have been used as lake-level gauges and recorders of lake-level variations (e.g., Cohen et al., 1997; Lisker et al., 2009; Mackey et al., 2018; Petryshyn et al., 2016). In the Dead Sea basin, Begin et al. (1985) and Neev & Emery (1967) dated fossil stromatolites and organic matter using the radiocarbon method. However, due to the inaccuracy of old beta-counting methods and the potential effects of contamination by young carbonate, these lake-level reconstructions involve significant uncertainties (Bookman et al., 2006; Stein, 2001). In addition to radiocarbon dating, Uranium-series geochronology has been applied to fossil stromatolites from the eastern slopes bordering the Dead Sea (Ghazleh & Kempe, 2009). Although only two ages were obtained and the datable aragonite was characterized by low ^{238}U, the ages approximate the timing of the maximum extent of paleolake Lisan (Figure 1c). Based on these findings, in this study, we focus on the application of stromatolites as proxies for reconstructing lake-level changes in the Dead Sea in combination with dating methods such as Uranium-series and radiocarbon.

2.3.4. Neotectonics in the Dead Sea Depression

The origin of the Dead Sea depression has been associated with the protracted motion of the Dead Sea Fault (DSF), a plate boundary transform fault that separates the Arabian and Sinai plates (Garfunkel, 1981). This fault has recorded more than 100 km of left-lateral displacement at rates of ∼5 m/Kyr since the Miocene (Ferry et al., 2007; Klinger et al., 2000; Masson et al., 2015). The Dead Sea depression is one of the largest pull-apart basins, extending for 150 km in N-S direction and with a width of 18 km. The basin results from a releasing bend possibly coupled with lithospheric erosion induced by thermal weakening (Petrunin et al., 2012). Extension and subsidence in the Dead Sea basin have led to the accumulation of 6 to 10-km-thick sedimentary sequences (Ben-Avraham et al., 2010). The Dead Sea depression is symmetrical and has been developed within two overlapping strands of the DSF, the western and eastern faults. The western Quaternary faults, active since at least 2.6 Ma, have been mapped in detail and are represented by sub-parallel anastomosed fault strands exposed along the coast (Sharon et al., 2018). In the northern region of the Dead Sea, the eastern faults are well-exposed, but their manifestation becomes less distinct in the southern part of the basin because of their offshore location. The eastern and western faults are in turn segmented by transverse faults that provide kinematic linkages and divide the Dead Sea depression in sub-basins of different depths (Lazar et al., 2006; Wetzler et al., 2014). Seismicity in the Dead Sea depression is distributed in the form of independent clusters along the main fault strands of the DSF, suggesting segmented fault activity (Wetzler et al., 2014).

Deformation rates at Holocene timescales in the Dead Sea region have been estimated from the outstanding exposure of offset channels and fault scarps (Ferry et al., 2007), recording left-lateral displacement rates of ∼5 m/Kyr. Instead, vertical deformation-rate estimates have remained limited to local observations. For instance, based on the Quaternary Lisan deposits, suggesting subsidence rates between 0.3 and 2 m/kyr (Bartov, Agnon, et al., 2006; Gardosh et al., 1990; Lisker et al., 2009). In contrast, deformation associated with a salt-diapir intrusion of the Mount Sodom, at the southern terminus of the Dead Sea, indicates fast uplift rates between 6 and 9 m/Kyr for the last 14 ka (Frumkin, 1996, 2009; Weinberger, Begin, et al., 2006; Weinberger, Lyakhovsky, et al., 2006).

3. Methods

Next, we describe the techniques used for the sampling and analysis of fossil lake shorelines and associated stromatolites, as well as the temporal and spatial corrections that we applied to the corresponding lake-level index points to derive the lake-level history of the paleolake Lisan period and the transition to the present-day Dead Sea.

3.1. Sampling of Fossil Shorelines and Stromatolites and Field Surveying

We surveyed, mapped and sampled a sequence of lake paleo-shorelines at eight different sites distributed along the western and eastern slopes of the Dead Sea. The sampling of lake paleo-shorelines at each site was focused on collecting in situ fossil stromatolites, often attached to bedrock and preserved in living positions. The morphology, internal structure and composition of fossil stromatolites were analyzed to elucidate the possible factors controlling their formation. Moreover, we studied 10 polished slabs and 10 thin sections to characterize the different fabrics, mineralogy, and biogenic structures of the stromatolites, using optical- and scanning electron (SEM) microscopy, X-ray diffraction and energy-dispersive spectroscopy (EDS).

In addition, we carried out photogrammetric drone surveys at each site (see details in SP1 in Supporting Information S1) to map the paleo-shorelines and complemented this data with geomorphic field observations.

3.2. Radiocarbon and Uranium-Series Dating, Analytical Procedures

Interpretation of radiocarbon ages from non-terrestrial samples can be complicated unless there is a temporal framework available from a different dating method. We therefore combined radiocarbon and U-series dating of fossil stromatolites to obtain a high-resolution chronology of lake-level variations.

We collected carbonate for radiocarbon dating of stromatolites (aragonite/calcite) by breaking off small fragments of the stromatolite core and soaking them in 1% HCl between 60 and 30 s to remove any coatings of young carbonate, obtaining 20–30 mg of sample material. Radiocarbon dating was carried out at the Poznań Radiocarbon Laboratories (Poland), following the method proposed by Brock et al. (2010).

U-series dating was carried out at the Institute for Environmental Physics, University of Heidelberg (Germany). We collected ~100 mg fragments of white carbonate layers or nodules from stromatolites (aragonite/calcite). The samples were dissolved in HNO_3, and spiked with the gravimetrical Tri-Spike ^{229}Th, ^{233}U and ^{236}U. Isotopes were measured using a Neptune MC-ICPMS. Further details of the sample handling, U and Th purification and measurement protocol can be found in Wefing et al. (2017). We used a secular equilibrium reference material HU-1 and an analytical blank injected into the MC-ICPMS to carry out rigorous quality checks on device performance. For age calculation, the resulting $^{234}U/^{238}U$ and $^{230}Th/^{238}U$ activity ratios were estimated using the half-lives of Cheng et al. (2000).

3.3. Temporal Correction of U-Series Ages

Obtaining accurate U-series ages from lake carbonates is often challenging because they can contain significant amounts of detritus that may alter the initial Th and U concentrations, and because of the presence of hydrogenous Th (e.g., Haase-Schramm et al., 2004; Torfstein, Goldstein, Kagan, & Stein, 2013). A number of authors have proposed different correction procedures for the presence of water-derived Th in carbonates (Haase-Schramm et al., 2004; Schramm et al., 2000).

As expected during high lake levels, the increased inflow may transport additional insoluble Th to the lake, which then precipitates within the aragonite, potentially increasing the amount of hydrogenous Th in the samples. However, Haase-Schramm et al. (2004) showed that the impact of hydrogenous Th on the calculated age becomes more significant with older samples. For instance, in a sample of 56 ka, hydrogenous Th can result in ages approximately 2 ka older, while for samples younger than 30 ka, the effect is around 0.5 ka or less. Additionally, Haase-Schramm et al. (2004) showed that for isochron ages, the effect of hydrogenous Th is even smaller and about a few hundred years older. Such an impact is relatively large in view of the precision of U-series dating and for samples with small analytical errors; however, it is relatively insignificant for samples that have been affected by detrital contamination, whose correction introduces larger uncertainties in the age calculation. In addition, the effect of hydrogenous Th has about the same range in all aragonite samples from other studies as well (Haase-Schramm et al., 2004; Torfstein, Goldstein, Kagan, & Stein, 2013). Thus, the relative effect of hydrogenous Th on the U-series dating results within the various studies should be negligible. We therefore, did not include this correction in our age calculations.

Under the assumption that the system has remained closed, moderate to high detrital contamination may still have a significant effect on the results of U-series dating. In order to deal with this issue, U-series isochron techniques have been developed to correct the detrital contribution of U and Th in "dirty carbonates" and to estimate detritus-free carbonate ages (e.g., Osmond et al., 1970; Rosholt, 1976). The isochrons are determined by plotting the activity ratios of coeval multiple subsamples from a single sample of the same age and fitting a linear regression. Depending on the isochron method used, the $^{234}U/^{238}U$ and $^{230}Th/^{238}U$ activity ratios of detritus-free carbonate are estimated either from the y-axis intercepts (for Osmond-type isochrons) or from the regression slope (for Rosholt-type isochrons) (Osmond et al., 1970; Rosholt, 1976). The activity ratios for the detritus-free carbonate endmember are then used to calculate the age of the set of sub-samples. The uncertainties of activity ratios derived from isochrons are estimated using the standard error at the axis intercept (Equations 1 and 2) and the goodness of fit compared using the R-squared (Equation 3).

$$S = \frac{1}{n-2} * \sum [y - (bx + a)]^2 \tag{1}$$

$$SE0 = S * \sqrt{\frac{1}{n} + \frac{(\bar{x})^2}{\sum (x - \bar{x})^2}} \tag{2}$$

$$R^2 = 1 - \frac{\sum (y - \hat{y})^2}{\sum (y - \bar{y})^2} \tag{3}$$

where S is the standard error, a and b are the coefficients of the linear regression, and n is the number of elements. SE0 is the standard error at intercept, y is the ordinate values of the isochron, $\bar{x}$ and $\bar{y}$ are the mean of abscissa and ordinate values (x and y), and $\hat{y}$ is the ordinate value predicted from the linear model.

3.4. Temporal Correction of Radiocarbon Ages

The radiocarbon reservoir age (RA) is the difference between the measured radiocarbon age (C) and the atmospheric radiocarbon age (Atm) at a defined calendar time (T) (Stuiver et al., 1986) (Equation 4):

$$RA\ (T) = C(T) - Atm(T) \tag{4}$$

However, although this formula is apparently simple, estimating the reservoir uncertainties can be difficult when calendar ages are poorly known or include non-symmetric uncertainties (e.g., Soulet, 2015). To determine the RA, we compared paired radiocarbon and U-series ages collected from stromatolites. Both ages were combined using an uncalibration-convolution process (Soulet, 2015), which fully propagates the uncertainties associated with the RA, including the uncertainties in radiocarbon and calendar ages (U-series ages) and uncertainties in the calibration curve, using the 1-sigma uncertainties of each variable. Calculations were performed using the software Radcal (Soulet, 2015) and the IntCal20 calibration curve (Reimer, 2020), for details see Soulet (2015). The resulting combined probability density functions (PDFs) were used to determine the RA, reported as the median, and 1σ, and 2σ errors calculated directly from the PDF. The evolution of RA through time was reconstructed using a nearest neighbor interpolation, reporting 1σ and 2σ confidence intervals.

The uncertainties in corrected and calibrated radiocarbon ages were estimated by combining the analytical errors in radiocarbon ages, the RA uncertainty, and the uncertainty in the atmospheric calibration curve. We propagated the uncertainty in RA and the analytical error in radiocarbon ages according to Equation 5:

$$\mathrm{E}_{RA} = \sqrt{Ea^2 + RAe^2} \tag{5}$$

where E_{RA} is the uncertainty in an RA-corrected radiocarbon age, Ea is the analytical error (1-sigma) in a radiocarbon age, and RAe is the error (1-sigma) in the RA at the time. Following the reservoir corrections, the radiocarbon ages were calibrated using IntCal20 and Matcal software for Matlab® (Lougheed & Obrochta, 2016), and the uncertainties were then incorporated using the Bayesian Higher Posterior Density (HPD) method of Matcal. We report the resulting ages using the median of the probability distributions and as cal. ka BP (kiloyears ago before 1950 C.E.), including the 1σ and 2σ confidence intervals.

3.5. Vertical Corrections

To compensate for factors that may have altered the original altitudinal position of the dated stromatolites, we applied geomorphic, hydro-isostatic, and tectonic corrections. The final output consists of calibrated and corrected lake-level index points that can be used to carry a lake-level reconstruction.

3.5.1. Geomorphic Corrections

The geomorphic correction includes the vertical uncertainties of stromatolite samples with respect to lake-level. Most of the stromatolites sampled were not located directly at the shoreline-angle between riser and tread (i.e., the cliff foot) (Figures 2c and 2d), which reflects the position of the lake-level at the time when the paleo-shoreline was formed. Because the stromatolites may have been built at different water depths, the sample elevation may have underestimated the lake-level position at the time. In order to compensate for this source of uncertainty, we used high-resolution drone topography to map the lake paleo-shorelines and shoreline-angles and validated them in the field. We then estimated the difference in elevation between the stromatolite sample, usually located on the shoreline tread, and the elevation of the shoreline-angle associated with the nearest paleo-shoreline in the uphill direction, which represents the probable water depth at which the stromatolite lived and was therefore included as a unidirectional vertical uncertainty.

3.5.2. Hydroisostatic Rebound and Sediment Loading

The contemporary lake-level fall of the Dead Sea has been shown to have resulted in hydro-isostatic uplift (Nof et al., 2012). Accordingly, the change in water volume during the transition from the paleolake Lisan to the present-day Dead Sea should also have resulted in hydro-isostatic rebound. To quantify this effect in our lake-level reconstruction, we used a thin-shell flexural model (Ventsel et al., 2002), which approximates the lithosphere as an elastic plate overlying an inviscid substratum; it is therefore time-invariant and only yields the

steady-state deflection that results when a load is in isostatic equilibrium with the upper mantle. Because the level of paleolake Lisan rose over several millennia starting from an already elevated position, and because of the relatively weak rheology of the upper mantle in this region (Petrunin et al., 2012), we assumed that mantle flow kept pace with filling the lake basin and that isostatic equilibrium therefore prevailed. Based on this premise we assume that the deflection in this region has already decayed completely; we therefore regard the pattern and magnitude of the modeled lithospheric deflection and hydro-isostatic rebound as being equivalent.

To model the lithospheric deflection, we extracted the volumetric loads from the topo-bathymetric digital elevation model of the Dead Sea (Hall, 1997), the elevation of the Lisan highstand shoreline and the present-day Dead Sea lake level. Despite the fact that Lake Lisan waters had a density of ~1.12 t/m^3 (Katz et al., 1977), we used a density of 1 t/m^3 in order to account only for the evaporated water mass, while the salt remains in the lake. We used a Young's modulus of 100 GPa and a Poisson's ratio of 0.25 following previous modeling studies in the Dead Sea (Mechie et al., 2005; Nof et al., 2012; Steinberg et al., 2014). To account for the effective elastic thickness (T_e) we performed a sensitivity test comparing flexural models using T_e of different window-sizes published by Pérez-Gussinyé et al. (2009) (see SP6 and Figure SP7 in Supporting Information S1). In addition, we included the effect of sediment accumulation that would have counteracted isostatic rebound. We created loading models using sedimentation rates between 0.6 and 1 m/Kyr based on Schramm et al. (2000) and Bartov et al. (2002) with a mean density of 2,250 kg/m^3 (Choi et al., 2011; Wetzler et al., 2015). Finally, the net isostatic rebound was obtained by subtracting the deflection patterns derived from water unloading and sediment loading and was used to correct the present-day elevation of each sample. T_e estimates and volumetric loads are based on present-day gravity and topography; therefore, the lithospheric response from these signals represents an approximation of processes occurring at present.

3.5.3. Tectonic Displacements

We calculated tectonic vertical displacements between different sites using the elevation of the highstand shoreline at the top of the sequence, which is a distinctive geomorphic feature that can be observed at all sites. Furthermore, the approximate age of this marker is known from previous studies (e.g., Bartov et al., 2002; Torfstein, Goldstein, Kagan, Stein, & Enzel, 2013) as well as from new data generated by us. Under the assumption that vertical displacement rates have been constant through time, the relative vertical displacement rate is obtained by dividing vertical displacements at each site by the age of the highstand shoreline according to Equation 6:

$$Vd = (z1 - z2)/Ht \tag{6}$$

where Vd is the relative vertical displacement rate, $z1$ and $z2$ are the elevations of the highstand shoreline at different sites, and Ht is the age of the highstand. We used the 0.3 m/Kyr subsidence estimated at the Masada Plain (Bartov, Agnon, et al., 2006), which is close to our site Mishmar and considered as a reference site (See Section 5.3.2 for more details on this choice). To estimate an absolute vertical displacement rate, the 0.3 m/Kyr subsidence rate was added to the relative vertical displacement rates for each site. The lake-highstand age and the elevation errors were then propagated to estimate the uncertainty in the vertical displacement rate. The error in sample elevation is in the range of centimeters and was therefore not included in the error calculation (Equation 7).

$$\delta Vd = Vd * \sqrt{\left(\frac{\sqrt{(\delta z1)^2 + (\delta z2)^2}}{z1 - z2}\right)^2 + \left(\frac{\delta Ht}{Ht}\right)^2} \tag{7}$$

where δVd is the vertical displacement rate error, $\delta z1$ and $\delta z2$ are the errors in the highstand elevation measurements, and δHt is the error in the highstand age. We estimated the amount of vertical displacement and used it to correct the sample elevation. The errors in the corrected sample-elevation were calculated using Equation 8.

$$\delta Se = \sqrt{\delta Vd^2 * \delta St^2} \tag{8}$$

where δSe is the error of the corrected sample elevation, δVd is the error in vertical displacement rate, and δSt is the error in the sample age.

3.6. Stable Isotope and X-Ray Diffraction Analyses

We analyzed $\delta^{18}O$ and $\delta^{13}C$ from fossil stromatolite carbonates to reconstruct the paleoclimatic and paleo-hydrological conditions during the time span of the lake-level reconstruction. The analyses were carried out in the Stable Isotope Laboratory at the GFZ-Potsdam (Geoforschungzentrum Potsdam, Germany). Our analytical strategy involved two different approaches: (a) the use of a single stable isotope analysis ($\delta^{18}O$ and $\delta^{13}C$) for each individual stromatolite and (b) multiple subsampling along a track for an individual stromatolite. We selected two stromatolite samples with regularly layered textures to carry out subsampling at 0.5 mm intervals along tracks 30–40 mm long. Each sample and subsample comprised 20–40 μg of carbonate, obtained using a microdrill (Sherline 5410) and a two-axis compound table module of 0.02 mm precision. The sampled material was processed in a KIEL-IV automated carbonate-reaction device. To decompose the sample, we used 103% H_3PO_4 at 70°C for 10 min, followed by the cryogenic purification of the released CO_2 and subsequent transfer into the MAT253 (Thermo Fisher Scientific) isotope ratio mass spectrometer (IRMS). The isotope composition is given in delta notation relative to the VPDB (Vienna Pee Dee Belemnite) standard calibrated against the international reference standard (NBS19) and an internal laboratory standard (C1) with an analytical precision of <0.07‰ for $\delta^{18}O$ and $\delta^{13}C$. In addition, the mineralogy of powder preparations from stromatolite samples was analyzed using X-ray diffraction, in order to obtain quantitative estimates of the mineral phases, we used the Rietveld refinement technique. This analysis was complemented with semi-quantitative EDS element mapping of polished thin sections.

3.7. Lake-Level Curve Reconstruction

We used the stromatolites as markers to reconstruct lake-level changes in the Dead Sea based on three main assumptions: (a) Stromatolites formed close to the coeval lake level. (b) Each stromatolite formed a closed chemical system without posterior diagenetic effects. (c) Possible vertical displacements and associated uncertainties since the time of stromatolite formation can be accounted for. The validity of these assumptions is of utmost importance for the reliability of our results and is discussed in detail in Sections 5.1 and 5.2.

We used a random sampling approach to explore the effect of vertical and temporal uncertainties on the lake-level curve and to estimate the confidence intervals of our reconstruction. Each temporally and vertically corrected stromatolite sample was first randomly perturbed according to its vertical and temporal uncertainties, assuming normally distributed uncertainties, following the method proposed by Stanford et al. (2011). We then fitted a smoothing spline to the perturbed values using a bin size of 60 years. The degrees of freedom of the spline were obtained automatically using cross validation (Green & Silverman, 1993). This random sampling procedure was repeated 1,000 times, obtaining the same number of fitted splines. We then stacked the spline values at each time bin, calculating the percentiles of their distribution, corresponding to the 68% and 95% (1 and 2-sigma) confidence intervals. We also used the median value to graphically represent the best estimate and trend of lake-level variations.

4. Results

4.1. Sampling Sites and Sampling Material

We surveyed and sampled lake paleo-shorelines exposed along the coast of the Dead Sea. The paleo-shorelines are usually exposed as a sequence of dozens of individual steps carved into the colluvium and occasionally into bedrock (Figures 2a and 2b). The paleo-shoreline morphology comprises a riser and a tread (Figures 2c and 2d). The riser is an erosional feature usually formed by rounded blocks of reworked colluvial material or forming small cliffs carved into bedrock. The paleo-shoreline tread has a lower slope than the riser and is usually overlain by an apron of fine sediments. The intersection between the tread and riser is defined as the shoreline angle, a marker that resembles the former lake-level position when the paleo-shoreline was formed. The different colors of the treads and risers form a characteristic pattern of dark and light fringes that facilitates their identification in the field (Figures 2c and 2d).

We carried out 13 transects across the lake paleo-shoreline sequences exposed along the eastern and western coasts of the Dead Sea (Figures 1b, 2e and 2f), collecting 84 fossil stromatolite samples for radiocarbon dating (27 in the eastern coast, 57 in the western coast of the Dead Sea) and 15 samples for U-series dating of fossil stromatolites (12 in the western coast and 3 in the eastern coast). The samples were collected at elevations between −365 and −170 masl with uncalibrated ages ranging between 40.1 and 9.7 ka. We distinguished two groups of ages on the basis of probability-density and age-elevation plots (Figure 3a); ages younger than 27.5 ka were usually characterized by a normal age-elevation pattern (ages become older with increasing shoreline elevation) while ages older than 27.5 ka display a scattered vertical distribution and usually occur in the context of irregular accumulations of stromatolites adjacent or above a partly preserved steeper zone or "central cliff zone" at the central part of the paleo-shoreline sequence (Figures 3b–3n). The central cliff zone is an erosional feature, often irregular, formed by one or two adjacent cliffs (SP2 in Supporting Information S1).

The growth morphologies and internal fabrics of fossil stromatolites vary from well-laminated (alternations of darker and lighter laminae) to poorly laminated forms with a spongy appearance (Figures 4a and 4b). Well-laminated stromatolites occurred in the form of crusts filling fractures in the bedrock or as the matrix of extensive tabular deposits of carbonate breccias partly covering the topography. Spongy stromatolites form dome and cauliflower structures on the tread of lake paleo-shorelines (Figures 4d–4f). These structures are usually overlying or transition laterally into beach gravels and blocks. Spongy stromatolites contain abundant irregular to sinuous cavities or fenestrae (50 μm–6 mm diameter), which increase their porosity. We also observed fenestrae filled with detrital material (e.g., quartz grains) or rimmed by calcite and isopachous cements (Figure 4c; See details in SP3 in Supporting Information S1). We attempted to remove the potential contamination effect of these young materials by leaching small fragments from the core of the stromatolites in 1% HCl (See Section 3.2). However, it is possible that some fraction of young material remained, leading to the occurrence of the outlier samples that were identified using statistical methods described in SP4 in Supporting Information S1. In addition, we included four samples with evidence of transport from an identified source in transects Boqueq-1 and Mazor-1 to increase the chronological control of these particular areas (See SP2 in Supporting Information S1).

We observed a correspondence between the age, the specific fabric of stromatolites, and the morphology of lake paleo-shorelines. For instance, at the central cliff zone, we found mostly laminated stromatolites with uncalibrated radiocarbon ages older than 27.5 ka, covering extensive areas or attached to the bedrock and filling fractures. Instead, spongy stromatolites occur as centimetric to metric dome structures attached on the sediment apron of well exposed lake paleo-shorelines, with uncalibrated radiocarbon ages younger than 27.5 ka. A detailed description of the sampling transects is provided in SP2, Figures SP1 and SP2 in Supporting Information S1.

4.2. Mineralogy of Fossil Stromatolites

The X-ray diffraction and EDS analyses indicate that the stromatolites are composed mostly of aragonite, low-magnesium calcite (LMC), high-magnesium calcite (HMC) and minor proportions of silicates and accessory minerals (Figures 4g–4j; See details in Tables SP1 and SP2 in Supporting Information S1). The younger samples (43 uncalibrated radiocarbon ages younger than 27.5 ka) are dominated by aragonite (usually higher than 60%) and minor proportions of HMC (<20%). In general, the ∼70% of the younger samples contain more than 60% of aragonite and HMC together, both usually considered primary carbonates. The content of LMC calcite is usually lower than 20%, only five samples display more than 50% of LMC. The dominant carbonate in the older samples (31 uncalibrated radiocarbon ages older than 27.5 ka) is aragonite (usually higher than 30%) and minor proportions of HMC calcite (<15%). In general, the ∼40% of the older samples contain more than 60% of aragonite and HMC together. The content of LMC ranges between 0% and 90%. Silicates and accessory minerals (<5%) are often present in the darker detrital and micritic layers and in the filling of fenestrae.

4.3. Uranium-Series Ages and Temporal Calibrations

We measured the U and Th isotopic compositions of 32 samples obtained from 15 fossil stromatolites; three samples were obtained from sites along the eastern coast of the Dead Sea and 12 samples from sites along the western coast (Table 1). The samples generally yielded ^{238}U values higher than 2,500 ng/g. Twenty-three coeval ages were obtained from multiple dating of six fossil stromatolite specimens, analyzed using the isochron method (Figure 5).

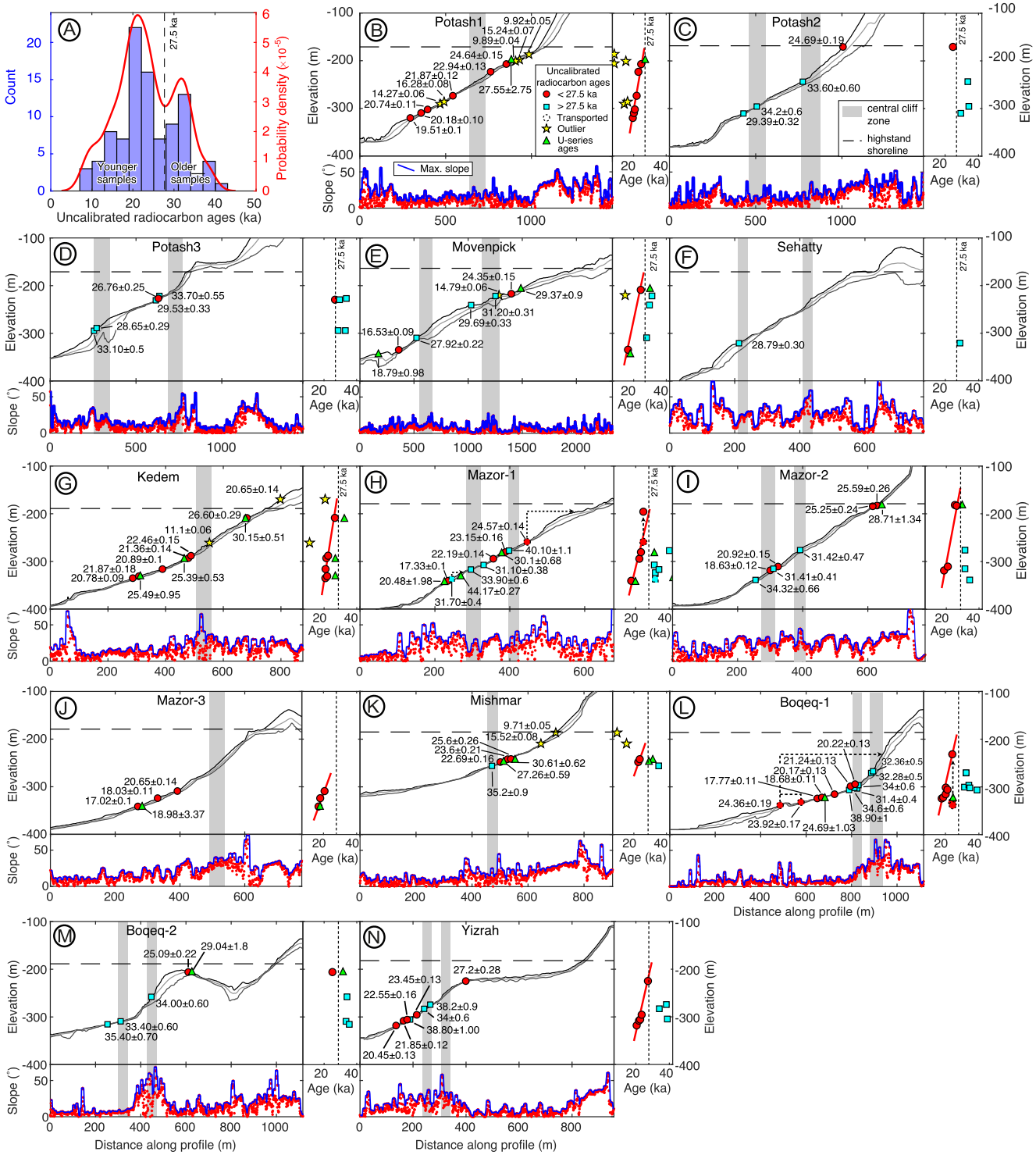

Figure 3. Topographic swath profiles, sampling locations for radiocarbon and U-series dating, and age-elevation plots. (a) Histogram and probability distribution of uncalibrated radiocarbon ages from fossil stromatolites in the Dead Sea. Note the bimodal population separated at 27.5 ka. B-N) Sampling transects and topographic swath profiles extracted from high-resolution drone topography showing the sample locations. Younger radiocarbon samples are shown as red circles and older samples as light blue squares; the data of these points are presented in Table 4. U-series samples are denoted by green triangles, the data of these points are presented in Table 1. The labels represent uncalibrated radiocarbon and U-series ages (ka: kiloyears ago). The dashed line indicates the elevation of the lake highstand. Age-elevation plots are shown on the right-hand side; the slope values along the swath-profile area (red dots) are shown beneath the profiles, and the blue line is the maximum slope. The grayed areas denote the central cliff zone.

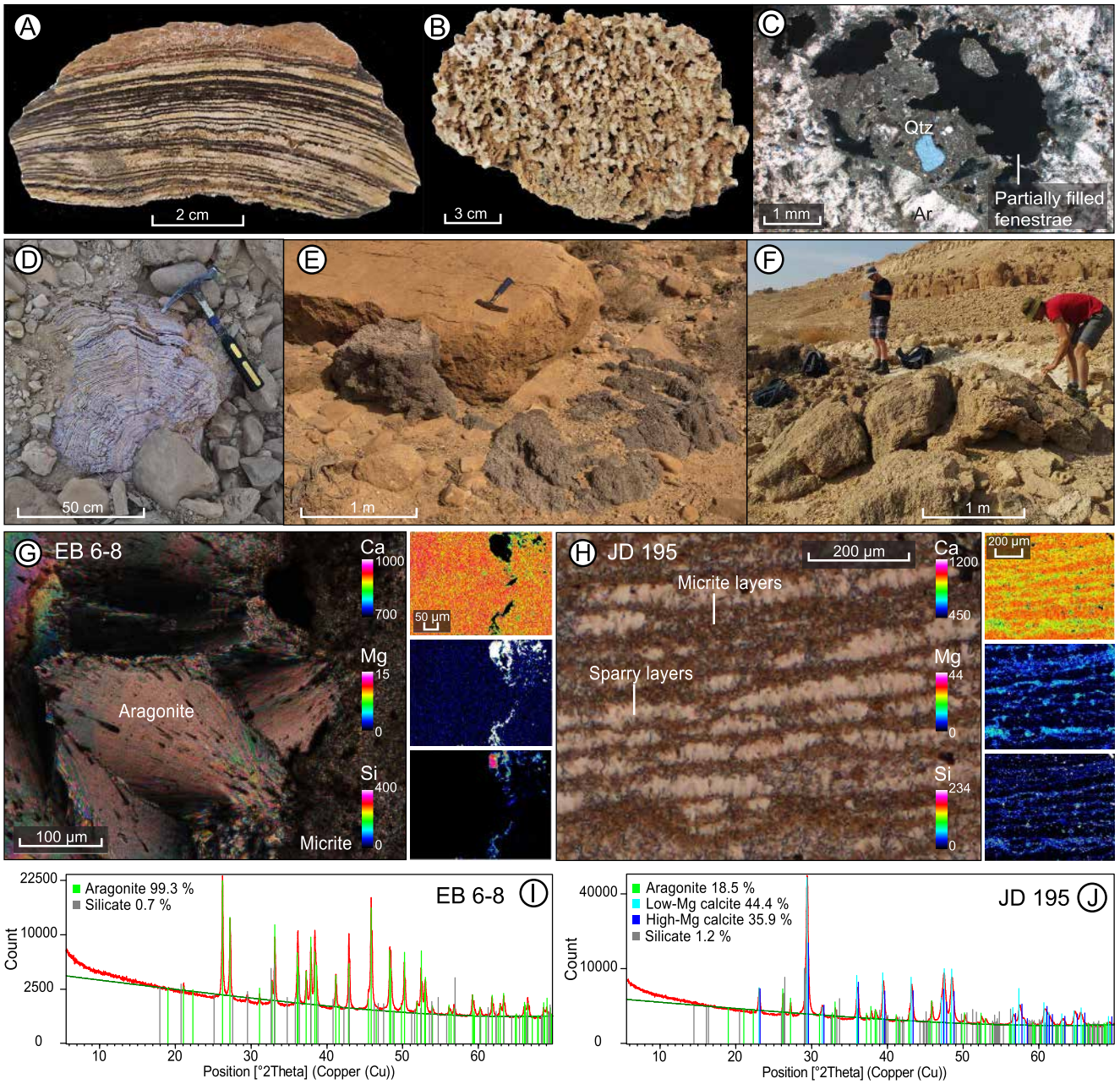

Figure 4. Growth morphologies, internal fabrics, and mineralogy of fossil stromatolites. (a) Well-laminated stromatolite fabric, (b) Spongy stromatolite fabric, (c) partially filled fenestrae, (d) laminated stromatolite with domal morphology, (e) stromatolite crusts filling fractures on bedrock, (f) large stromatolite with domal morphology. (g) and (h) EDS analyses of spongy and laminated stromatolites, respectively; the insets show the relative concentrations of calcium (Ca), magnesium (Mg) and silica (Si). (i) and (j) X-ray diffraction analyses of the samples in (g) and (h).

The initial activity ratios obtained from the intercept and slope of the isochrons ranged between 0.24 and 0.35 $^{230}Th/^{238}U$ and between 1.4 and 1.53 $^{234}U/^{238}U$ for Rosholt and Osmond type isochron diagrams (Table 2, Figure 5). In all cases the Rosholt isochrons have positive slopes and higher R-squared values (>0.95) than Osmond isochrons, leading to more robust linear regressions (Figure 5). The ages derived from the activity ratios obtained from both isochron types are very similar. However, the Rosholt isochrons display a broader range of activity ratios resulting in more robust linear regressions with higher R-squared (Figure 5); therefore, we selected the Rosholt isochrons as the preferred results to estimate the initial activity ratios and ages. The isochron-calibrated ages were on average 3.5 Kyrs younger than the subsample ages. The uncertainties (2-sigma) of

Geochemistry, Geophysics, Geosystems

10.1029/2024GC011541

Table 1
U-Series Ages of Fossil Stromatolites

Sample	Type	Elevation (m)	238U (ng/g)	Error (ng/g)	232Th (ng/g)	Error (ng/g)	230Th/238U (act. Ratio)	Error (abs)	230Th/232Th (act. Ratio)	Error (abs)	d234U o/oo	Error (abs.)	Age uncorr. (ka)	Error (ka)	d234U (ini) o/oo	Error (abs.)	Age corr. (ka)	Error (ka)
UEG 5-6	(Un)	−280.4	6248.442	0.383	78.249	0.105	0.372	0.001	91.083	0.208	490.39	0.43	30.87	0.07	533.94	1.12	30.10	0.68
UEG 5-11	(Rs)	−341.3	3511.315	0.176	199.775	0.263	0.267	0.001	14.436	0.036	406.01	0.61	22.78	0.05	428.38	4.13	18.97	3.37
UJD 11	(Rs)	−351.0	3806.386	0.197	67.745	0.101	0.248	0.001	42.554	0.114	472.58	0.63	19.92	0.05	498.36	1.54	18.79	0.98
UMET8-2	(Rs)	−293.0	4300.899	0.133	42.071	0.050	0.318	0.000	99.740	0.191	481.55	0.49	26.00	0.04	517.39	0.93	25.40	0.53
UEB6-14	(Un)	−322.2	3886.241	0.179	73.951	0.099	0.315	0.001	51.004	0.109	476.64	0.48	25.88	0.05	511.09	1.58	24.69	1.03
UEB7-27	(Rs)	−205.9	3215.655	0.151	104.954	0.136	0.370	0.001	34.862	0.082	472.88	0.66	31.08	0.07	513.32	2.71	29.04	1.80
UIS14-1	(Rs)	−208.6	6360.648	0.281	59.679	0.122	0.368	0.001	120.900	0.377	479.36	0.73	30.73	0.09	521.99	1.10	30.15	0.51
UIS18-2	(Un)	−241.0	4148.949	0.176	46.942	0.089	0.371	0.001	101.401	0.300	469.62	0.79	31.32	0.08	512.06	1.25	30.61	0.62
UEG5-2	(Un)	−325.0	5889.511	0.277	27.319	0.043	0.500	0.001	331.021	0.783	466.74	0.57	44.46	0.10	528.80	0.76	44.17	0.27
UEG5-8	(I,Rs)	−340.6	4068.013	0.208	47.035	0.067	0.253	0.001	67.065	0.182	406.79	0.69	21.48	0.05	431.32	1.09	**20.48**	**1.98**
UEG5-8	(I,Rs)	−340.6	2513.307	0.203	284.963	0.585	0.345	0.001	9.276	0.033	414.11	1.50	30.10	0.10	441.25	8.72		
UEG5-8	(I,Rs)	−340.6	3399.116	0.265	72.761	0.153	0.307	0.001	43.728	0.211	421.90	1.59	26.22	0.13	452.57	2.36		
UEG5-8	(I,Rs)	−340.6	3319.416	0.284	125.614	0.320	0.308	0.001	24.765	0.122	434.65	1.95	26.03	0.13	464.65	3.57		
UIS62	(I,Rs)	−183.0	4851.696	0.283	65.821	0.111	0.373	0.001	84.430	0.222	479.87	0.66	31.25	0.08	522.93	1.30	**28.71**	**1.34**
UIS62	(I,Rs)	−183.0	4648.030	0.254	45.191	0.097	0.364	0.001	115.632	0.413	477.69	0.96	30.37	0.10	519.61	1.31		
UIS62	(I,Rs)	−183.0	4528.710	0.327	64.502	0.120	0.383	0.001	82.061	0.257	473.22	0.85	32.36	0.10	517.25	1.46		
UIS62	(I,Rs)	−183.0	4579.766	0.377	84.463	0.140	0.376	0.001	62.262	0.168	477.75	0.78	31.50	0.08	520.56	1.73		
UIS19 B	(I,Rs)	−242.0	4510.924	0.246	128.914	0.215	0.372	0.001	40.090	0.112	470.46	0.89	31.36	0.08	511.47	2.48	**27.26**	**0.59**
UIS19 B	(I,Rs)	−242.0	6146.125	0.284	106.761	0.176	0.356	0.001	63.377	0.162	472.78	0.74	29.74	0.07	512.65	1.59		
UIS19 B	(I,Rs)	−242.0	4742.853	0.521	62.363	0.156	0.356	0.001	82.534	0.320	479.99	0.87	29.55	0.10	520.59	1.42		
UIS19 B	(I,Rs)	−242.0	3713.273	0.362	122.633	0.219	0.385	0.001	35.569	0.117	467.62	1.18	32.71	0.10	509.90	2.92		
UIS8	(I,Rs)	−330.8	4668.744	0.206	84.150	0.131	0.326	0.001	55.480	0.143	467.58	0.60	27.07	0.07	503.14	1.55	**25.49**	**0.95**
UIS8	(I,Rs)	−330.8	4156.665	0.211	161.502	0.466	0.343	0.001	27.264	0.128	466.98	1.34	28.65	0.12	502.88	3.37		
UIS8	(I,Rs)	−330.8	4389.912	0.270	94.676	0.170	0.323	0.001	45.682	0.158	466.65	1.04	26.79	0.09	501.48	1.99		
UJD192	(I,Un)	−216.0	2847.016	0.177	59.039	0.102	0.358	0.001	52.672	0.176	467.65	1.10	30.03	0.10	507.15	2.03	**29.37**	**0.90**
UJD192	(I,Un)	−216.0	2555.029	0.161	154.736	0.204	0.408	0.001	20.527	0.052	458.03	0.89	35.19	0.09	500.45	4.91		
UJD192	(I,Un)	−216.0	2754.670	0.211	206.741	0.430	0.382	0.001	15.500	0.050	462.16	0.89	32.50	0.09	499.80	6.17		
UJD192	(I,Un)	−216.0	2603.710	0.168	209.440	0.344	0.385	0.001	14.610	0.046	465.30	1.19	32.78	0.10	503.11	6.69		
UJD192	(I,Un)	−216.0	1643.827	0.105	691.491	0.939	0.429	0.001	3.109	0.010	481.39	2.18	36.63	0.11	490.60	28.24		
UJD1921	(I,Un)	−206.0	2432.117	0.164	79.209	0.156	0.513	0.001	48.045	0.156	470.63	1.23	45.70	0.15	532.44	2.99	**27.55**	**2.75**
UJD1921	(I,Un)	−206.0	2734.849	0.193	83.186	0.159	0.523	0.002	52.480	0.226	475.38	1.90	46.56	0.24	539.40	3.32		
UJD1921	(I,Un)	−206.0	2920.077	0.271	81.701	0.179	0.491	0.002	53.472	0.220	478.36	2.01	43.04	0.19	537.66	3.22		

Note. Rs: Sample used for radiocarbon reservoir, I: Endmember of U-series isochron, Un: Unpaired sample. All errors are 2-sigma. Bold numbers are isochron corrected ages.

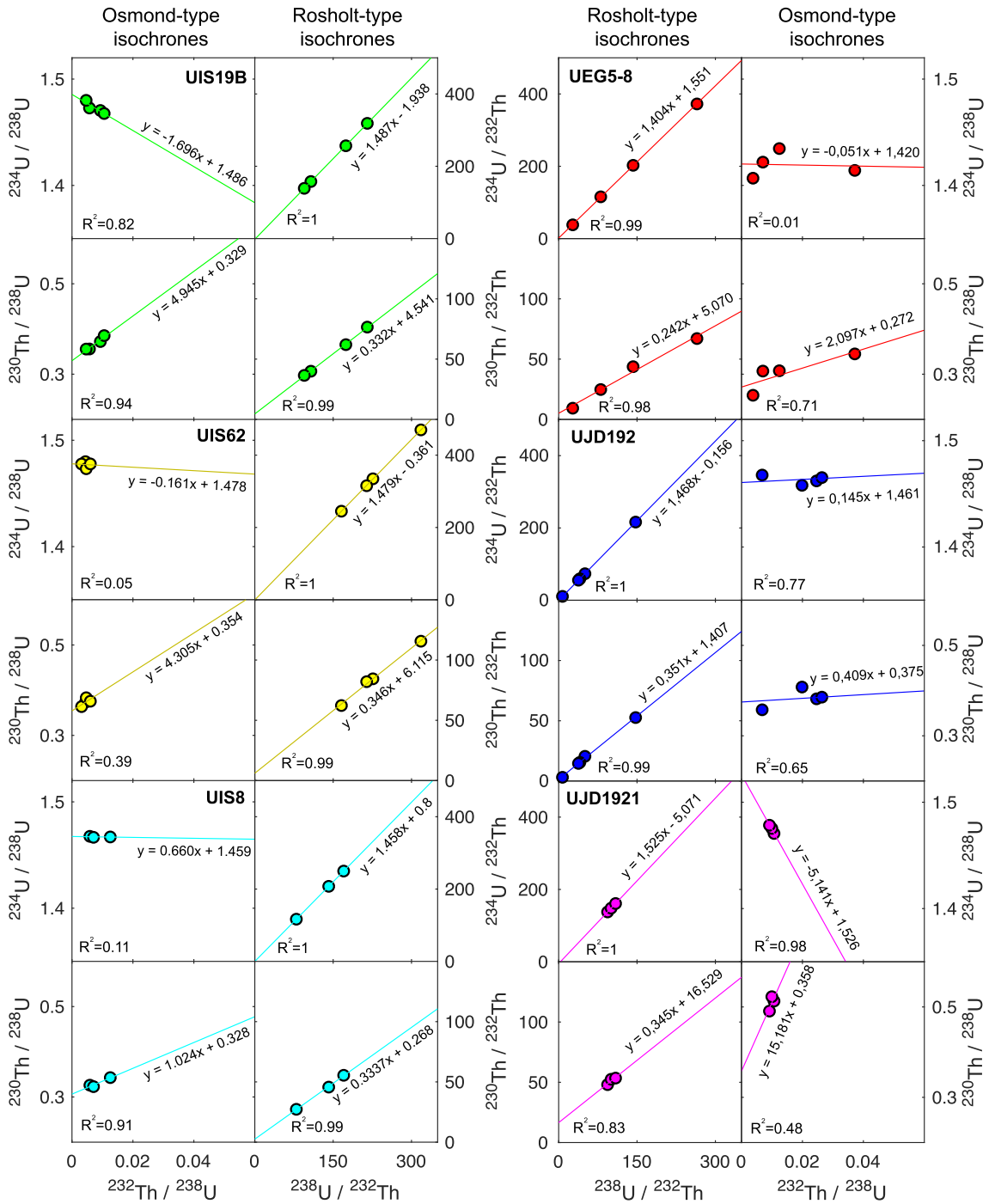

Figure 5. Isochron calibration of U-series ages including Osmond and Rosholt diagrams.

isochron-calibrated ages range between 0.6 and 2 Kyrs, except for sample UJD1921 with an arbitrary uncertainty of 2.75 ka, which is significantly higher than the range of uncertainties of subsample values and probably associated with the dispersion of samples and the standard error of linear regressions. Sample UJD1921 is problematic because of its extremely large age error as the three subsamples do not span a large range; we assigned an arbitrary 10% error to its age. Despite the large error, we decided to include the UJD1921 isochron-calibrated age in the lake-level reconstruction because of the scarce number of ages obtained from the higher lake

Table 2
Results of Isochron Calibration of U-Series Ages

Isochron	No. ages	234U/238U	Error	230Th/232Th (ini.)	Error	230Th/238U	Error	Age (ka)	Error (Kyrs)
(a)									
UEG5-8	4	1.420	0.011	2.097	0.944	0.272	0.019	22.90	1.70
UIS62	4	1.478	0.008	4.305	3.753	0.354	0.018	29.50	1.60
UIS19 B	4	1.486	0.004	4.945	0.896	0.330	0.007	27.03	0.60
UIS8	3	1.459	0.010	1.024	3.079	0.328	0.026	25.26	0.76
UJD192	5	1.461	0.003	0.409	0.173	0.375	0.011	31.85	1.07
UJD1921	3	1.526	0.008	15.181	15.657	0.358	0.156	28.73	2.87[a]
(b)									
UEG5-8	4	1.404	0.008	5.070	3.241	0.242	0.021	20.50	2.00
UIS62	4	1.479	0.007	6.114	3.477	0.346	0.015	28.70	1.30
UIS19 B	4	1.487	0.005	4.541	0.942	0.333	0.006	27.26	0.59
UIS8	3	1.458	0.014	0.268	5.349	0.334	0.037	25.49	0.95
UJD192	5	1.468	0.002	1.407	0.702	0.351	0.009	29.37	0.90
UJD1921	3	1.525	0.008	16.529	15.528	0.345	0.153	27.54	2.75[a]

Note. (a) Osmond-type isochron (b) Rosholt type isochron results. [a]Arbitrary 10% error of isochron-calibrated age.

paleo-shorelines; its age estimate was taken with caution and its activity ratios were not considered when estimating the average initial $^{230}Th/^{232}Th$ ratios.

The isochron intercepts with the 1:1 equilibrium line in the Rosholt diagram provide an estimate of the initial $^{230}Th/^{232}Th$ ratio of a detrital component, under the assumption that ^{234}U, ^{238}U and ^{230}Th are in secular equilibrium in the detrital material. The same approach was previously used by Haase-Schramm et al. (2004) and Torfstein, Goldstein, Kagan, and Stein (2013) to date the aragonite layers of the Lisan Formation. The initial detrital $^{230}Th/^{232}Th$ component of fossil stromatolites ranged between 2.2 and 9.4 (Figure 6a); we calculated an averaged value of 2.6 ± 2.2 as the initial $^{230}Th/^{232}Th$ activity ratio and the corresponding error (standard deviation). This correction is similar to the 3.7 ± 0.37 used by Haase-Schramm et al. (2004) and the values of 1 ± 0.1 to 6 ± 1.8, used by Torfstein, Goldstein, Kagan, and Stein (2013). For a comprehensive evaluation of the average detrital component of paleolake Lisan, we used all isochrons provided from the Lisan Formation with three or more subsamples (Haase-Schramm et al., 2004; Torfstein, Goldstein, Kagan, & Stein, 2013), combining them with our stromatolite isochrons. We then determined the maximum likelihood probability and standard deviation of the initial $^{230}Th/^{232}Th$ (Figures 5a and 5b), obtaining a value of 2.7 ± 2.35 (Figure 6b). We used this value to correct the measured $^{234}U/^{238}U$ and $^{230}Th/^{238}U$ activity ratios of individual samples and of each isochron subsample (Table 1). The detritus-corrected ages are younger than the original ages, showing differences between 0.5 and 5 Kyrs.

Our ages were plotted against initial $\delta^{234}U$ values including the results from Torfstein, Goldstein, Kagan, and Stein (2013) and Haase-Schramm et al. (2004) based on the analysis of the aragonitic layers of the Lisan Formation (Figure 6c). The matching between our and previous estimates confirms the validity of the U-series dating approach for fossil stromatolites. We used an evolution plot to compare the initial range of $^{234}U/^{238}U$ ratios from stromatolites and those from the Lisan Formation and to corroborate our results (Figure 6d). The evolution plot is based on the assumption that the stromatolites were initially formed in equilibrium with the $^{234}U/^{238}U$ of the lake water, which remained constant. Our results show convergence toward initial $^{234}U/^{238}U$ ratios of between 1.43 and 1.54, which is a relatively narrow range, and similar to the range proposed by Torfstein, Goldstein, Kagan, and Stein (2013) for the sequences of the Lisan Formation (1.5–1.55 $^{234}U/^{238}U$). The distribution of samples between 20 and 40 ka isochrons portrays the progressive decay of $^{234}U/^{238}U$ from its initial value under the assumption of closed-system conditions.

4.4. Radiocarbon Ages and Temporal Calibrations

To estimate the radiocarbon RA during the Lake Lisan highstand period, we compared nine paired radiocarbon and U-series ages from stromatolites (Tables 1 and 3). The calendar (U-series ages) ages ranged between 18.79

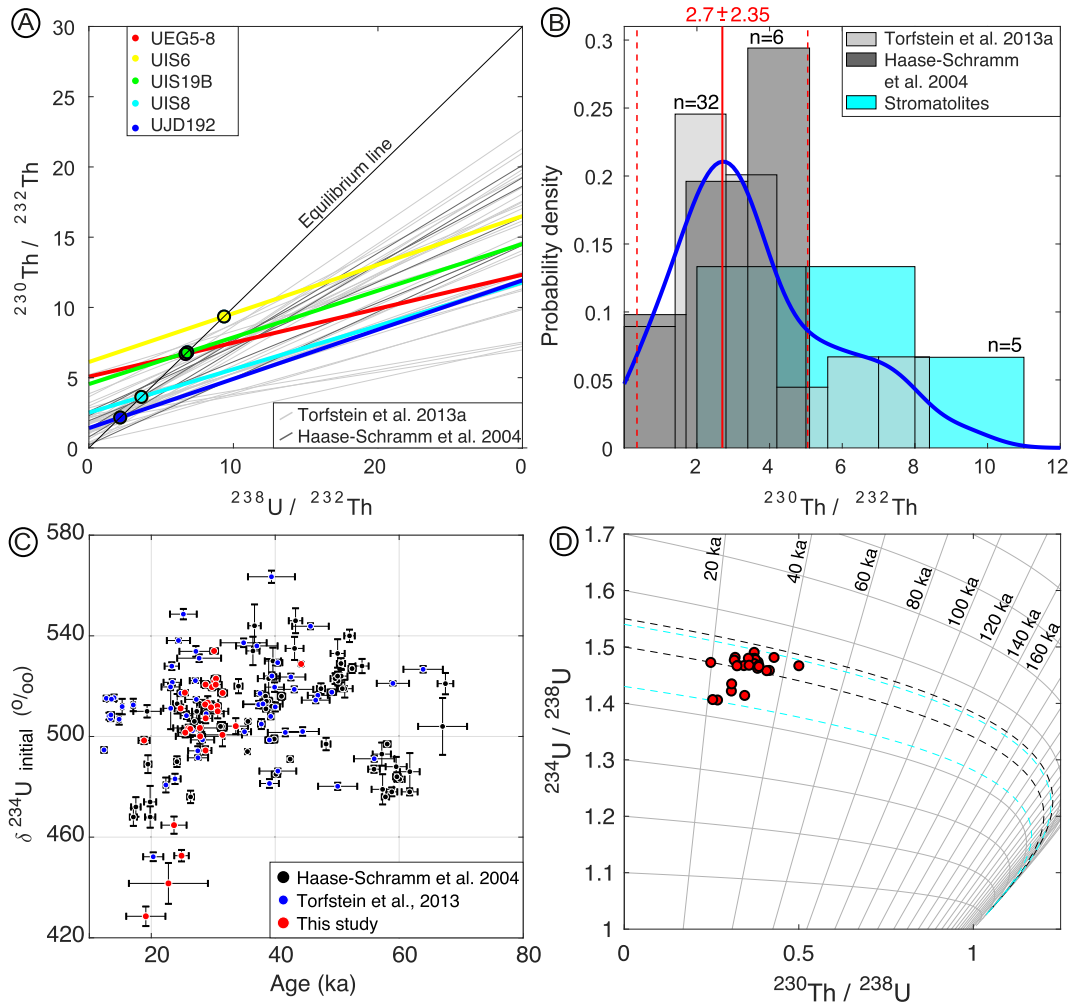

Figure 6. Isochron intercepts used to correct initial d^{234}U values and evaluation of the consistency of U-series dating of fossil stromatolites. (a) Comparing isochrons from the Lisan Formation and stromatolites, the intersection with the equilibrium line indicates the detrital ^{230}Th/^{232}Th component. (b) Histograms of equilibrium line intercepts, the blue line is the mixture of all isochrons. We found a value of 2.7 ± 2.35 used to correct single sample U-Th ages, where n is the number of isochrons. (c) U-series ages and initial δU^{234} from stromatolites compared with estimates from the Lisan Formation. (d) Evolution plot of U-series ages from fossil stromatolites. The dashed black lines indicate the range estimated by Torfstein, Goldstein, Kagan, and Stein (2013), while the light blue dashed lines indicate the range determined from fossil stromatolites.

and 30.14 ka (Table 3). RA estimates based on the comparisons between radiocarbon and isochron-calibrated U-series ages yielded lower 1-sigma values ranging between ∼0.4 and ∼0.8 Kyrs, while RA estimated between individual U-series and radiocarbon ages generally displayed higher 1-sigma values than isochron-calibrated ages, ranging between ∼0.3 and ∼1.5 Kyrs. The median RA varied between 0.17 and 1.18 Kyrs (Figures 7a and 7b, Table 3), while the combined probability distribution yielded a median of 0.65 Kyrs (Figure 7a). The evolution of RA was marked by contrasting changes (Figure 7b). The oldest RA estimate at 30.14 ka yielded 0.67 kyrs and was extrapolated to 46 ka, at 29 ka the RA was low reaching 0.18 Kyrs, followed by an abrupt increase to 1.07 Kyrs at 28.71 ka; between 28.71 and 25.39 ka the RA decreased gradually to 0.28 kyrs, it remained constant until 20.48 ka and increased abruptly to 1.04 Kyrs at ∼19 ka.

After applying the RA-correction and atmospheric calibration, the resulting radiocarbon ages were older than the initial ages. The RA-corrected and calibrated radiocarbon ages from fossil stromatolites ranged between 18.88 and 43.21 ka with 1-sigma errors ranging between 0.2 and 1.7 Kyrs and 2-sigma errors between 0.5 and 3.2 kyrs (Table 4, Figures 8a and 8b).

Table 3
Paired Radiocarbon and U-Series Ages Used to Estimate the Radiocarbon Reservoir Age

Sample Radiocarbon	Sample U-series	U-series (ka)	Error 1-sigma (Kyrs)	Uncal. radiocarbon (ka)	Error 1-sigma (Kyrs)	Median RA (Kyrs)	1-sigma bounds −	(Kyrs) +	2-sigma bounds −	(Kyrs) +
JD11C	UJD11	18.794	0.492	16.530	0.090	0.999	0.519	1.475	0.216	1.866
EG 5-11A	UEG5-11	18.975	1.686	17.020	0.100	1.048	−0.359	2.590	−1.075	3.387
EG 58-A	UEG5-8[a]	20.481	0.988	17.330	0.100	0.283	−0.456	1.080	−0.928	1.632
MET 8-2A	UMET8-2	25.397	0.263	21.360	0.140	0.284	0.037	0.553	−0.194	0.741
IS8C	UIS8[a]	25.494	0.476	21.870	0.180	0.704	0.064	1.145	−0.297	1.412
IS19BC	UIS19B[a]	27.265	0.296	23.600	0.210	0.616	0.175	1.095	−0.113	1.328
IS-62	UIS6-2[a]	28.708	0.670	25.590	0.260	1.077	0.338	1.689	−0.057	2.186
EB 7-27C	UEB7-27	29.036	0.902	25.090	0.220	0.176	−0.683	1.049	−1.327	1.670
IS14C	UIS14-1	30.145	0.256	26.600	0.290	0.673	0.249	1.165	0.002	1.459

[a]Isochron-calibrated age.

4.5. Vertical Corrections and Lake-Level Reconstruction

We applied vertical corrections that considered hydro-isostatic adjustment, tectonic displacements, and geomorphic corrections that represent uncertainties related to the initial position of the sample. The temporally calibrated and vertically corrected samples were used to generate a lake-level curve (Figures 8a–8d).

Geomorphic correction was only possible for the younger samples, where the morphology was closely linked with the stromatolite deposit. The maximum height difference was measured between the stromatolite position and the shoreline angle of the nearest paleo-shoreline riser in the uphill direction from the sampled stromatolite. The height differences were less than 7 m and averaged 1.3 m, resembling the water depth at which the stromatolites were formed. For the older samples, located at the central cliff, the absence of clear paleo-shoreline morphologies hinders the application of the geomorphic correction.

The net isostatic rebound values ranged between 3.6 and 4.2 m. The highest net rebound occurred at the Kedem and Sehatty sites; these values were subtracted from the present-day elevation of each dated sample location (Figure SP8 in Supporting Information S1). The faster tectonic subsidence of 0.48 m/Kyr determined for the Kedem site corresponds to positive vertical displacements of 11–14 m. In contrast, the slower subsidence of 0.05 m/Kyr at the Boqeq site resulted in 1–2 m of positive vertical displacements (see Table 5, SP6 and Figure SP8A-B in Supporting Information S1), which we added to the respective sample elevations (Figure 8c).

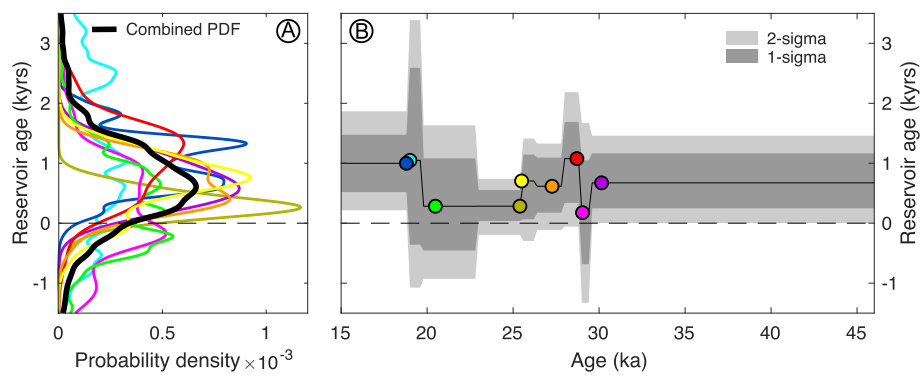

Figure 7. Radiocarbon reservoir. (a) Reservoir age probability density functions (PDFs) of each paired U-series and radiocarbon ages from fossil stromatolites. The black line is the mixture of all PDFs. (b) Evolution of radiocarbon-age reservoir and associated 1 and 2-sigma errors based on the PDFs in A (ka: kiloyears ago, kyrs: kiloyears).

Geochemistry, Geophysics, Geosystems

10.1029/2024GC011541

Table 4
Radiocarbon Ages of Fossil Stromatolites, Temporal Calibrations and Stable Isotopes

Site	Sample	Uncalib, 14C (ka)	Error (Kyr)	Elevation uncorrected (masl)	Elevation corrected (masl)	Elevation error (m)	UTM X	UTM Y	$\delta^{18}O$ (‰)	$\delta^{13}C$ (‰)	RA-corr, (ka)	Error 1-sigma (Kyrs)	Calib, Age (ka)	Max, range 2-sigma (ka)	Min, range 2-sigma (ka)	Max, range 1-sigma (ka)	Min, range 1-sigma (ka)
Boqeq	EB 6-13A	17.77	0.11	−324	−327	3	724926	3452160			16.77	0.11	20.30	21.71	21.52	20.84	19.61
Boqeq	EB 6-14A	18.68	0.11	−322	−325	3	724896	3452181	0.08	5.76	17.68	0.11	21.45	22.62	20.24	22.07	20.86
Boqeq	EB 6-15A	20.17	0.13	−315	−318	3	724833	3452191	1.85	6.50	19.89	0.13	24.05	25.78	22.47	24.85	23.09
Boqeq	EB6-21C	20.22	0.13	−302	−304	3	724766	3452070	1.26	5.26	19.94	0.13	24.11	25.81	22.50	24.93	23.16
Boqeq	EB 6-17A	21.24	0.13	−306	−308	3	724787	3452090	1.80	4.95	20.96	0.13	25.21	27.07	23.49	25.94	24.28
Boqeq	EB 6-12A	23.92	0.17	−332	−253	3	724993	3452180	1.46	5.96	23.92	0.17	28.14	28.81	27.52	28.43	27.79
Boqeq	EB 6-11A	24.36	0.19	−338	−252	3	725000	3452250	1.69	6.18	24.08	0.19	28.28	28.96	27.72	28.58	27.90
Boqeq	EB7-27C	25.09	0.22	−206	−208	3	724717	3451440	1.67	6.43	24.81	0.22	29.06	29.93	28.35	29.49	29.34
Boqeq	EB 6-19A	31.40	0.40	−301	−303	4	724751	3452120	1.31	0.72	30.73	0.40	35.17	36.31	34.21	35.65	34.55
Boqeq	EB 6-232A	32.28	0.45	−271	−273	4	724686	3452030	1.16	4.31	31.61	0.45	36.01	37.51	34.67	36.60	35.32
Boqeq	EB 6-23A	32.36	0.45	−270	−273	4	724688	3452040	1.73	4.09	31.69	0.45	36.10	37.64	34.68	36.69	35.38
Boqeq	EB7-25C	33.40	0.60	−309	−311	5	725193	3451180	1.23	−0.16	32.73	0.60	37.45	39.43	35.80	38.35	36.33
Boqeq	EB 6-22A	34.00	0.60	−296	−298	5	724755	3452030	−0.61	4.88	33.33	0.60	38.15	39.91	36.32	39.13	37.18
Boqeq	EB 7-26A	34.00	0.60	−258	−260	5	724704	3451550	1.62	3.96	33.33	0.60	38.15	39.91	36.33	39.13	37.18
Boqeq	EB 6-20A	34.60	0.60	−302	−304	5	724760	3452110	0.83	6.39	33.93	0.60	38.83	40.64	36.98	39.70	37.71
Boqeq	EB 7-24A	35.40	0.70	−315	−317	5	725225	3451160	0.74	4.33	34.73	0.70	39.87	41.45	37.65	40.90	39.15
Boqeq	EB 6-16A	38.90	1.00	−307	−308	5	724785	3452110	1.80	6.28	38.23	1.00	42.44	44.20	41.20	43.03	41.76
Yizrah	EB 6-1A	20.45	0.13	−318	−313	3	725206	3449437	1.56	6.52	20.17	0.13	24.37	26.00	22.67	25.23	23.60
Yizrah	EB 6-2A	21.85	0.12	−308	−303	3	725161	3449495	1.61	4.24	21.57	0.12	25.89	27.43	24.20	26.89	26.52
Yizrah	EB 6-4A	22.55	0.16	−306	−300	3	725097	3449577	1.53	6.24	22.55	0.16	26.86	28.61	25.43	27.46	26.01
Yizrah	EB 6-3A	23.45	0.13	−296	−290	3	725068	3449579			23.45	0.13	27.63	28.27	27.22	27.81	27.36
Yizrah	EB6-9C	27.20	0.28	−225	−218	3	724913	3449760	1.72	4.99	26.58	0.28	30.75	31.72	29.93	31.15	30.29
Yizrah	EB 6-7A	34.00	0.60	−283	−273	4	725043	3449630	2.18	6.52	33.33	0.60	38.15	39.91	36.33	39.13	37.18
Yizrah	EB 6-8A	38.20	0.90	−274	−263	4	725031	3449710	1.93	6.39	37.53	0.90	42.00	43.25	40.63	42.51	41.40
Yizrah	EB 6-5A	38.80	1.00	−305	−293	5	725095	3449550	2.28	5.09	38.13	1.00	42.38	44.15	41.13	42.96	41.70
Kedem	IS9	20.78	0.09	−335	−327	3	727332	3488512	0.02	7.41	20.50	0.09	24.72	26.35	23.04	25.56	25.39
Kedem	IS10	20.89	0.10	−316	−308	3	727222	3488534	1.08	6.21	20.61	0.10	24.83	26.44	23.08	25.66	24.00
Kedem	MET 8-2A	21.36	0.14	−293	−285	3	727102	3488200	0.05	6.97	21.08	0.14	25.34	27.09	23.80	26.02	24.33
Kedem	IS8C	21.87	0.18	−331	−323	3	727309	3488544	0.84	6.85	21.59	0.18	25.91	27.54	27.49	26.90	26.53
Kedem	MET 8-1A	22.46	0.15	−288	−280	3	727088	3488258			22.46	0.15	26.78	28.41	25.30	27.38	25.96
Kedem	IS14 C	26.60	0.29	−209	−198	3	726890	3488460	1.96	5.54	25.98	0.29	30.28	31.12	29.23	30.92	29.89
Movenpick	JD11	16.53	0.09	−351	−352	2	745969	3513160	−4.55	7.28	15.53	0.09	18.88	20.15	17.82	19.35	18.28

Geochemistry, Geophysics, Geosystems

10.1029/2024GC011541

Table 4
Continued

Site	Sample	Uncalib, 14C (ka)	Error (Kyr)	Elevation uncorrected (masl)	Elevation corrected (masl)	Elevation error (m)	UTM X	UTM Y	$\delta^{18}O$ (‰)	$\delta^{13}C$ (‰)	RA-corr, (ka)	Error 1-sigma (Kyrs)	Calib, Age (ka)	Max, range 2-sigma (ka)	Min, range 2-sigma (ka)	Max, range 1-sigma (ka)	Min, range 1-sigma (ka)
Movenpick	JD195	24.35	0.15	−225	−224	3	746565	3512760	−1.37	−0.94	24.07	0.15	28.26	28.87	27.72	28.55	27.91
Movenpick	JD1910	27.92	0.22	−326	−324	3	746106	3513270	0.36	4.37	27.03	0.22	31.22	32.96	30.04	31.75	30.42
Movenpick	JD12	29.69	0.33	−257	−255	4	746541	3513540			29.02	0.33	33.39	34.49	31.94	34.23	32.44
Movenpick	JD198	31.20	0.31	−238	−235	4	746724	3513840	0.27	−0.34	30.53	0.31	34.99	36.09	34.16	35.40	34.46
Potash	JD1928	19.51	0.10	−337	−337	3	741884	3452363	0.30	6.83	18.46	0.10	22.56	26.29	19.38	24.11	20.66
Potash	JD1915	20.18	0.10	−325	−325	3	741947	3452330	0.32	7.36	19.90	0.10	24.06	25.78	22.48	24.86	23.11
Potash	JD1926	20.74	0.11	−318	−318	3	741992	3452320	0.05	6.97	20.46	0.11	24.68	26.32	23.02	25.56	25.38
Potash	JD1923	21.87	0.12	−289	−289	3	742120	3452260	1.76	7.11	21.59	0.12	25.91	27.45	24.22	26.89	26.53
Potash	JD1927	22.94	0.13	−239	−239	3	742435	3452600	1.24	6.13	22.94	0.13	27.22	27.98	26.32	27.71	26.59
Potash	JD1917	24.64	0.15	−222	−222	3	742462	3452420	0.41	3.54	24.36	0.15	28.54	29.13	27.88	28.91	28.18
Potash	JD7	24.69	0.19	−185	−184	3	742389	3450220			24.41	0.19	28.60	29.19	27.86	29.03	28.26
Potash	JD2	26.76	0.25	−246	−245	3	741951	3448190	1.62	4.70	26.14	0.25	30.43	31.17	29.32	30.92	30.03
Potash	JD5	28.65	0.29	−309	−308	4	741604	3448540	−0.54	−2.01	27.57	0.29	31.90	33.91	30.33	32.86	32.40
Potash	JD10	29.39	0.32	−326	−325	4	741854	3450880	−0.93	0.36	29.21	0.32	33.57	35.62	31.52	34.53	32.62
Potash	JD1	29.53	0.33	−246	−244	4	741951	3448190	0.93	3.78	29.03	0.33	33.37	34.74	31.72	34.27	32.53
Potash	JD4	33.10	0.50	−309	−308	4	741604	3448540	−1.39	−5.22	32.43	0.50	37.01	39.07	35.60	37.80	36.06
Potash	JD8	33.60	0.60	−259	−257	4	742231	3450770	−1.01	1.13	32.93	0.60	37.70	39.61	36.07	38.65	36.60
Potash	JD3	33.70	0.55	−243	−241	4	741972	3448640	−0.60	1.07	33.03	0.55	37.81	39.55	36.19	38.82	36.86
Potash	JD9	34.20	0.60	−311	−309	4	741922	3450840	1.99	6.50	33.53	0.60	38.36	40.17	36.49	39.32	37.38
Sehatty	JD13	28.79	0.30	−337	−329	4	743187	3499420	0.44	6.91	27.71	0.30	32.06	34.08	30.62	32.91	31.12
Mazor	EG 5-11A	17.02	0.10	−341	−343	2	725871	3477900	2.35	4.80	16.02	0.10	19.43	20.56	18.53	19.94	18.83
Mazor	EG 5-8A	17.33	0.10	−341	−342	2	725887	3478786	1.58	5.61	16.33	0.10	19.78	20.97	18.71	20.32	19.15
Mazor	EG 5-12A	18.03	0.11	−324	−325	2	725838	3477761	1.29	4.00	17.03	0.11	20.63	22.02	19.49	21.24	19.93
Mazor	IS6	18.63	0.12	−319	−320	2	725752	3478102	0.72	6.52	17.63	0.12	21.39	22.55	20.17	22.04	20.81
Mazor	EG 5-13A	20.65	0.14	−309	−310	3	725794	3477697	0.07	7.04	20.37	0.14	24.58	26.28	22.96	25.55	25.37
Mazor	IS2	20.92	0.15	−311	−312	3	725758	3478260	1.61	2.65	20.64	0.15	24.86	26.78	26.48	25.70	24.03
Mazor	EG 5-4A	22.19	0.14	−294	−295	3	725772	3478787	1.91	5.72	21.91	0.14	26.26	27.78	24.63	27.15	25.61
Mazor	EG 5-6A	23.15	0.16	−280	−281	3	725741	3478770	1.95	6.31	23.15	0.16	27.44	27.91	26.67	27.68	27.24
Mazor	EG 5-1A	24.57	0.14	−259	−201	3	725681	3478773	0.37	6.21	24.29	0.14	28.46	29.08	27.85	28.78	28.08
Mazor	IS5	25.25	0.24	−182	−182	3	725473	3478360	1.74	−2.83	24.97	0.24	29.26	30.02	28.61	29.67	28.85
Mazor	IS62	25.59	0.26	−183	−184	3	725460	3478258	1.74	−2.82	24.91	0.26	29.20	30.72	30.46	29.98	28.56
Mazor	EG 5-5A	31.10	0.38	−307	−307	4	725800	3478760	0.13	5.10	30.43	0.38	34.92	36.12	33.96	35.38	34.37
Mazor	IS3	31.41	0.41	−315	−315	4	725761	3478200	1.26	4.85	30.74	0.41	35.18	36.33	34.20	35.67	34.55

Geochemistry, Geophysics, Geosystems

10.1029/2024GC011541

Table 4
Continued

Site	Sample	Uncalib, 14C (ka)	Error (Kyr)	Elevation uncorrected (masl)	Elevation corrected (masl)	Elevation error (m)	UTM X	UTM Y	$\delta^{18}O$ (‰)	$\delta^{13}C$ (‰)	RA-corr, (ka)	Error 1-sigma (Kyrs)	Calib, Age (ka)	Max, range 2-sigma (ka)	Min, range 2-sigma (ka)	Max, range 1-sigma (ka)	Min, range 1-sigma (ka)
Mazor	IS4	31.42	0.47	−276	−276	4	725674	3478210	0.80	3.36	30.75	0.47	35.20	36.47	34.12	35.74	34.54
Mazor	EG 5-2A	31.70	0.40	−337	−325	4	725880	3478820	−1.35	6.81	31.03	0.40	35.45	36.59	34.38	35.99	34.82
Mazor	EG 5-3A	33.90	0.60	−317	−316	4	725833	3478810	1.17	−1.80	33.23	0.60	38.04	39.81	36.26	39.05	37.08
Mazor	IS1	34.32	0.66	−339	−338	4	725828	3478260	1.18	4.41	33.65	0.66	38.49	40.46	36.59	39.49	37.44
Mazor	EG 5-7A	40.10	1.10	−277	−276	5	725727	3478840	1.18	−0.70	39.43	1.10	43.22	45.05	41.97	43.91	42.39
Mishmar	IS18 C	25.60	0.26	−241	−236	3	725158	3476623	2.01	4.03	24.90	0.16	29.19	30.73	30.47	29.99	28.52
Mishmar	IS19AC	22.69	0.16	−248	−244	3	725186	3476590	1.30	5.98	22.69	0.21	26.99	28.71	25.67	27.71	26.13
Mishmar	IS19BC	23.60	0.21	−242	−238	3	725157	3476619	1.72	6.26	23.60	0.26	27.80	28.56	27.28	28.06	27.37
Mishmar	IS15C	35.20	0.90	−256	−248	4	725398	3476870	−0.48	0.17	34.53	0.90	39.58	41.59	37.15	40.88	38.50
Mishmar	IS16[a]	9.71	0.05	−186			725096	3476890	1.44	5.10							
Potash	JD1921[a]	9.89	0.04	−206			742678	3451880	2.30	2.80							
Potash	JD1930[a]	9.92	0.05	−188			742675	3453110	0.07	2.45							
Kedem	IS11C[a]	11.10	0.06	−261			727047	3488750	2.84	2.38							
Potash	JD1925[a]	14.27	0.06	−306			742064	3452320	−1.04	5.11							
Movenpick	JD191[a]	14.79	0.06	−237			746551	3512870	2.25	3.42							
Potash	JD1918[a]	15.24	0.07	−204			742666	3451960	0.70	3.62							
Mishmar	IS17C[a]	15.52	0.08	−210			725079	3476720	2.04	4.23							
Potash	JD1924[a]	16.28	0.08	−301			742090	3452350	0.41	6.26							
Kedem	IS13C[a]	20.65	0.14	−170			726813	3488570	1.96	3.15							

Note. RA corr.: Age corrected for radiocarbon reservoir age. Calib.: Atmospherically calibrated age. [a]Outliers.

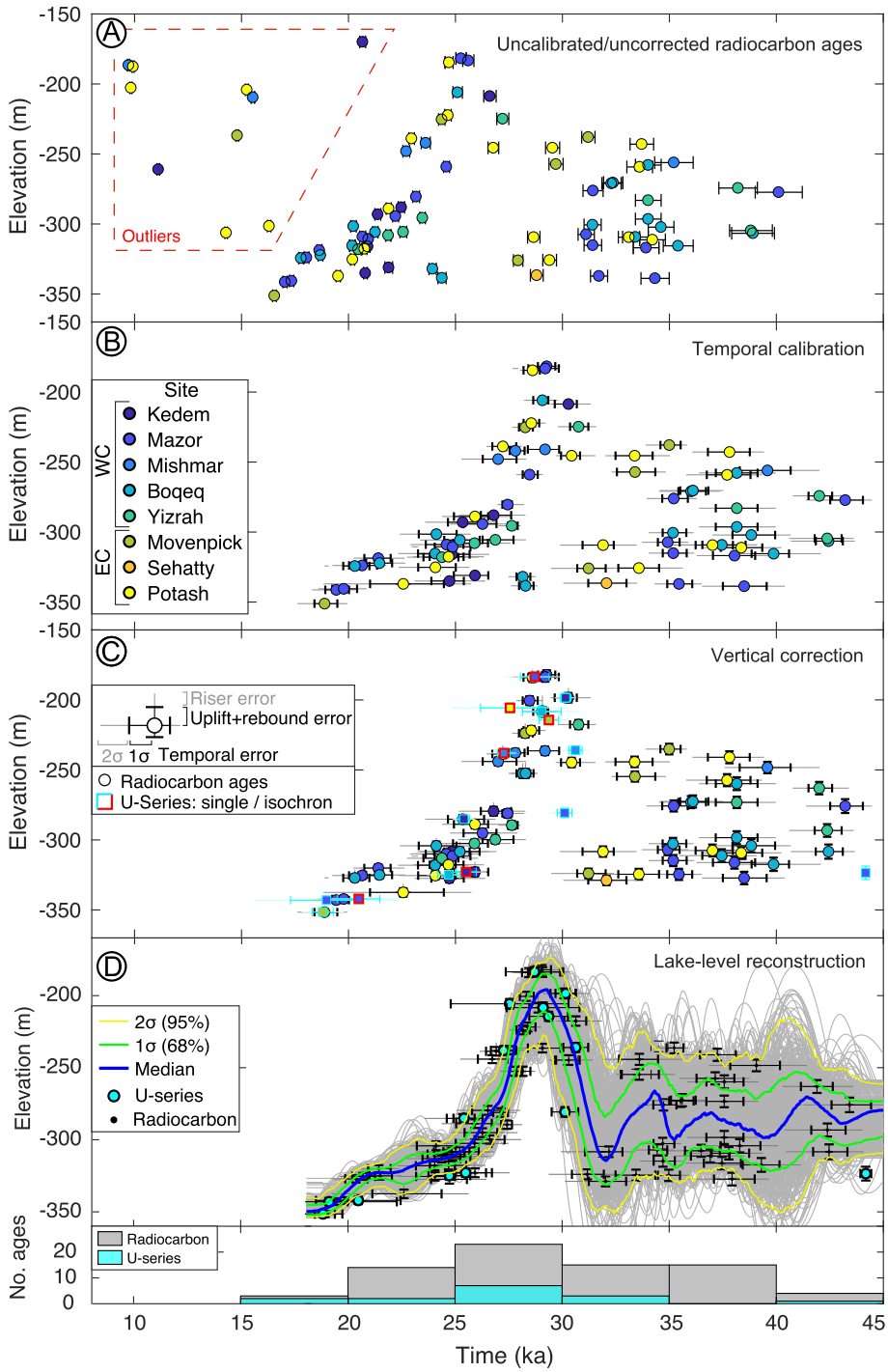

Figure 8. Temporal calibrations and spatial corrections of lake-level markers based on radiocarbon and U-series ages, and lake-level reconstruction. (a) Uncalibrated and uncorrected radiocarbon ages, excluded outlier samples are enclosed by red dashed lines. (b) RA-corrected and calibrated radiocarbon ages. EC and WC: Eastern and Western coasts of the Dead Sea. (c) Vertically corrected and temporally calibrated radiocarbon and U-series ages. In most cases the vertical errors are smaller than the marker size. (d) Lake-level reconstruction, gray lines are iterated smoothing splines generated from randomly optimized samples. The histogram in the lower panel displays the distribution of ages and the contributions of the two different dating methods.

Table 5
Elevations of Highstand Shorelines and Tectonic Vertical Displacement Rates

Site	Highstand elevation (m)	Error (m)	Highstand elevation corrected[a] (m)	Relative elevation difference[b] (m)	Relative vertical displacement rate (m/Kyr)	Error (m/Kyr)	Absolute vertical displacement rate[c] (m/Kyr)	Error (m/Kyr) (m/Kyr)
Kedem	−188.00	3	−192.23	−5.09	−0.18	0.11	−0.48	0.11
Mazor	−178.00	3	−182.15	4.98	0.17	0.11	−0.13	0.11
Mishmar	−183.00	3	−187.13	0.00	0.00	0.10	−0.30	0.10
Boqeq	−176.00	3	−179.78	7.35	0.25	0.11	−0.05	0.11
Yizrah	−185.00	3	−188.75	−1.62	−0.06	0.10	−0.36	0.10
Movenpick	−180.00	3	−184.14	2.99	0.10	0.11	−0.20	0.11
Sehatty	−185.00	3	−189.21	−2.08	−0.07	0.11	−0.37	0.11
Potash	−179.00	3	−182.73	4.41	0.15	0.11	−0.15	0.11

[a]Highstand elevation corrected by hydro isostatic rebound. [b]Elevation difference with respect to site Mishmar. [c]Absolute vertical displacement rate in reference to the subsidence rate of 0.3 m/Kyr estimated by Bartov, Agnon, et al. (2006). Negative values indicate subsidence.

4.6. Lake-Level Reconstruction

The distribution of spatially corrected sample elevations and temporally calibrated radiocarbon ages and U-series ages displays a distinct pattern of lake-level variations between 45 and 18 ka. We identified two distinct age groups within the lake-level reconstruction, younger ages (<30 ka) and older ages (>30 ka), both displaying different trends and scatter. The high level of variability in the older ages relates to greater chronological errors and scattered distributions between −320 and −250 masl overlapping with the location of the central cliff zone observed in all topographic profiles. In contrast, younger ages are less scattered, have smaller errors, and are distributed within a relatively narrow band. The 10 outlier samples identified using statistical methods (See SP4 and Figure SP5 in Supporting Information S1) are younger than 20 ka, they are notoriously separated from the trend of the narrow band of younger ages (Figure 8a) and are probably affected by contamination by young carbonate materials (see Section 4.1). These outlier samples were excluded from our lake level reconstruction. The remaining samples were temporally calibrated and spatially corrected. The temporal calibration of radiocarbon ages resulted in temporal offsets toward older ages, this can be appreciated in the slight offset of the ages in Figure 8b toward older values in comparison with uncorrected/uncalibrated ages Instead, the vertical correction, which include tectonic, isostatic and geomorphic corrections, generally resulted in positive vertical offsets; this can be observed as a slight difference in elevation between Figures 8b and 8c. Finally, we applied the random sampling approach (See Section 3.4) on the corrected and calibrated samples in order to obtain a lake level curve with confidence intervals observed in Figure 8d.

Assuming that stromatolites grow approximately at a water depth that is close to lake-level positions (see Section 5.1 and SP3 in Supporting Information S1), the scattering of older ages may indicate a period of high-frequency but low amplitude lake-level oscillations. In contrast, the younger ages (<29.2 ± 0.9 ka according the 1-sigma of the Monte Carlo simulation) suggest a period of large-scale and rapid reduction in water level. Both periods are separated by a distinct episode during which the lake-level rose by ∼100 m at a rate of ∼60 m/Kyr between 30 and 31 ka. After a short (∼2 Kyrs) highstand period at a level of ∼−180 masl, the lake-level then started to fall at ∼28.5 ka. The first phase of this fall in the water level was extremely rapid, with the water level falling about 80 m within about 1.5 Kyr at a rate between 70 and 50 m/Kyr. However, this rate was still two orders of magnitude lower than the present-day rate of the ongoing lake-level drop (Lensky et al., 2005). The initial rapid fall in lake-level was followed by a deceleration from ∼27 ka with a rate of 20–25 m/Kyr, reaching a quasi-stable (∼3 m/Kyr) lake-level at ∼−315 masl for the period between 24.5 and 21.5 ka. A subsequent short period of lake-level fall occurred between 21 and 19 ka at a rate of ∼12 m/kyr, followed by a quasi-stable lake-level of −350 masl at ∼19 ka (Figure 8d).

In summary, the pattern of lake-level changes in the Dead Sea basin suggests that the older stromatolites were formed under a regime of low amplitude and high frequency lake level variations. This variability probably intensified coastal erosion resulting in an irregular cliff, defined as the "central cliff." Afterward, this cliff was

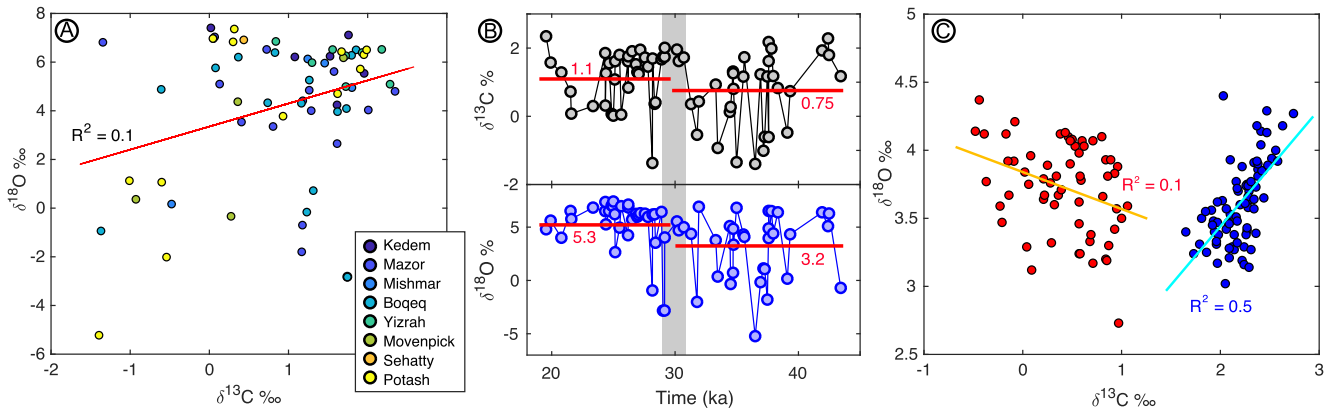

Figure 9. Stable isotope values from fossil stromatolites. (a) Plot of $\delta^{13}C$ against $\delta^{18}O$ from individual samples, color-coded by site; no clear covariance can be seen. (b) Plot of stable isotopes against time, the red lines show the mean values before and after the highstand. (c) Plot of $\delta^{13}C$ against $\delta^{18}O$ of along track measurements in samples (UJD192, red and JD1910 blue).

drowned in the course of the rapid lake-level rise that occurred after ~31 ka. This episode was followed by a rapid lake drop where the old cliff was subsequently overprinted by a new sequence of regressive lake shorelines and associated stromatolites. Nevertheless, remnants of the older fossil stromatolites in fractures and in the form of pavements in the central cliff zone may have been preserved as a result of the rapid water level changes. This would explain the overlap between older and younger ages.

4.7. O and C Stable Isotopes

We performed 207 measurements of $\delta^{18}O$ and $\delta^{13}C$ on carbonates, 139 of which were obtained along tracks in two samples of layered stromatolites (UJD192 and JD1910) and 68 from individual samples. The $\delta^{13}C$ values ranged between −4.2 and 3.7‰ and the $\delta^{18}O$ values ranged between −5 and 7.5‰. When plotting $\delta^{13}C$ against $\delta^{18}O$ for individual samples, the resulting linear regression revealed very low R-squared values, suggesting a lack of correlation (Figure 9a). Furthermore, there are no evident clusters of stable isotope values related to different sites, suggesting the absence of any geographic control on the isotopic variability (Figure 9a). Samples younger than 30 ka (calibrated ages) generally tended to have $\delta^{18}O$ values 2‰ higher than the samples older than 30 ka, which had variable $\delta^{18}O$ values and higher levels of dispersion. Ages younger than 30 ka usually had positive $\delta^{13}C$ values, whereas older ages were broadly dispersed but had slightly lower values (Figure 9b). When comparing the stable isotope measurements along individual tracks of stromatolites, we noted a slightly higher correlation ($R^2 = 0.5$) between $\delta^{18}O$ and $\delta^{13}C$ for sample JD1910 in comparison to UJD192 (Figure 9c). Further discussion on the meaning of this correlation is provided in Section 5.4.

5. Discussion

5.1. Reliability of Fossil Stromatolites for Reconstructing Lake-Level Changes in the Dead Sea

Although our lake-level reconstruction included both temporal calibrations and spatial corrections, there are two critical factors that argue against the use of fossil stromatolites for rigorous reconstructions of lake-level changes in the past: (a) uncertainties regarding the water depths at which the stromatolites were formed, and (b) the effects of contamination by old carbon and diagenesis, which can significantly compromise the radiometric age determination of stromatolites. Photosynthetic microorganisms, predominantly cyanobacteria and occasionally eukaryotic algae, are crucial for the development of stromatolites in lacustrine and marine environments (Riding, 1991). During the Quaternary stromatolites had a wide distribution in lacustrine settings, where they have mostly grown in the littoral and shallow-water photic zones, although exceptional occurrences at 60 m water depth in Lake Tanganyika have also been reported (Cohen et al., 1997). The fossil stromatolites analyzed in this study exhibit a wide variation of morphologies and internal fabrics that presumably reflect the complex interplay of both abiotic and biotic processes (see SP3 and Figures SP3 and SP4 in Supporting Information S1). In addition, the saline and hypersaline conditions of paleolake Lisan and the Dead Sea, respectively, have fostered the development of atypical and unique microbial imprints (Häusler et al., 2014; Ionescu et al., 2012; Thomas

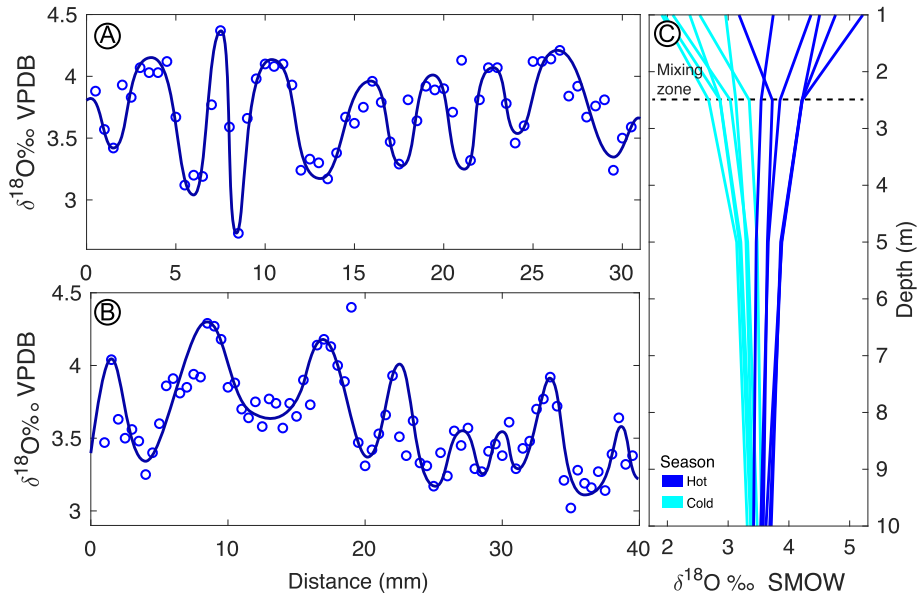

Figure 10. Seasonal isotopic variability in fossil stromatolites. (a and b) Analysis of $\delta^{18}O$ along a track of samples UJD192 and JD1910, respectively, note the rhythmic variability at millimetric-scale. (c) Water column stratification in the Dead Sea (depth in meters below the lake-level); the mixing zone is subject to high seasonal $\delta^{18}O$ variability (based on Gat, 1984).

et al., 2016). Although there is no direct information concerning the species of microorganisms that may have been responsible for the Lisan stromatolites, their macro and microfabrics as well as their compositional characteristics suggest that photosynthetic microbes might have been involved in their formation (SP3 and Figures SP4A-O in Supporting Information S1). These organisms usually live within the photic zone, which in the Dead Sea is limited to approximately 2 m water-depth (Oren & Shilo, 1982); however, the depth of the photic zone may vary seasonally depending on the sediment input and physicochemical conditions of the lake. Therefore, elucidating the depth of formation of fossil stromatolites based on their fabrics and type of microorganisms remains speculative. Consequently, additional criteria are necessary to adequately estimate their positions with respect to the past lake-levels.

In the context of the geomorphic conditions that were conducive for stromatolite formation, we observed that fossil stromatolites occur in direct association with lake paleo-shorelines and most of the samples were collected from shoreline treads that represent the shallow marginal lake floor. The stromatolites and lake paleo-shorelines may therefore be considered to be coeval, and we thus can relate each stromatolite location to a specific paleo-shoreline level. The elevation of the riser foot represents the lake-level position at the time of stromatolite formation; the maximum height difference between the stromatolites and the foot of the corresponding shoreline riser was less than 7 m and on average 1.3 m (see Section 4.1 and SP2 in Supporting Information S1), which is close to the ∼2 m depth range of the photic zone (Oren & Shilo, 1982), suggesting that these stromatolites lived under rather shallow water conditions.

From a paleoclimatic point of view, if the stromatolites are formed under shallow-water conditions, then their stable isotopic signature is likely to reflect atmospheric interchange. Measurements of $\delta^{18}O$ in the present-day water column of the Dead Sea indicate a shallow mixed zone characterized by variable $\delta^{18}O$ values in response to seasonality and atmospheric interchange, and a deeper zone characterized by quasi-stable $\delta^{18}O$ values (Gat, 1984) (Figure 10c). The results of our along-track analyses of $\delta^{18}O$ reveals a rhythmic millimetric-scale pattern of isotopic variability that most likely represents seasonal variations, as can be observed in surface waters during alternating cold and hot seasons (Figures 10a and 10b). Gat (1984) showed that the mixed water layer extends to 2.5 m depth. Therefore, the isotopic variability in the stromatolites may further indicate that they lived in shallow-water environments.

With regard to paleoclimatic conditions, previous studies suggested that stromatolites in the Dead Sea basin appear only during high lake levels when the lake salinity was lower than the present Dead Sea (Lisker

et al., 2009). Our study, however, shows the presence of fossil stromatolites throughout the entire analyzed interval, with variable distribution along fossil shorelines. Larger accumulations were observed near delta areas such as the Mazor, Boquec, and Yizrah sites, where they appear at almost every shoreline level, while they are less abundant in areas such as Movenpick and Kedem, which are distant from river outlets. These observations suggest that the presence of stromatolites does not only seem to be linked with the lake salinity but also with the local site conditions.

5.2. Old Carbon and Diagenesis

Bookman et al. (2007) identified old detrital carbonate fragments within the aragonite layers of the Lisan Formation that could produce temporal offsets ranging from hundreds to thousands of years in radiocarbon-age estimates. The authors proposed a correction factor based on the ratio of authigenic aragonite to calcite from old carbonate. However, it should be emphasized that these old fragments have only been found in the Lisan Formation and not yet in stromatolites. The analysis of stromatolite thin sections indicates relatively clean material composed mainly of carbonates (aragonite and calcite) such as micrite, peloids, and coarse spar, with only a minor proportion of detrital material corresponding mostly to siliciclastic grains (quartz and silicates) (see Supplementary Materials SP3). Moreover, if calcite from old rocks were present, one would expect a large disagreement between U-series ages and radiocarbon measurements. However, both dating methods show consistent results. In addition, the reservoir ages from the stromatolites are within the same range as the values obtained from the Lisan Formation (See Section 5.4); therefore, we disregarded the effect of old radiocarbon in our radiocarbon age corrections.

Post-depositional processes such as diagenesis (i.e., recrystallization) can also produce open-system conditions, resulting in erroneous age estimates for both U-series and radiocarbon methods. The stromatolites sampled were exposed directly at the surface and had not been affected by depositional processes since their formation. However, carbonates can also be affected by diagenesis when exposed at the surface due to the effect of infiltrating meteoric water. LMC is a stable species of calcite usually formed by the recrystallization of metastable primary carbonates such as aragonite and HMC, or in special conditions, can be associated to the metabolism of the microorganisms and the microenvironmental conditions inside the microbial mat. Regarding the first possibility, the presence of LMC suggests that the stromatolites underwent some degree of recrystallization during their exposure at the surface, indicating open-system conditions that may result in inaccurate radiocarbon and U-Series ages. Open-system conditions may usually produce a loss of uranium isotopes, which will result in older U-series ages. Conversely, in the case of radiocarbon geochronology, open-system conditions will result in the incorporation of modern carbon and hence, younger radiocarbon ages. On the other hand, the presence of dead carbon from dust or old limestone formations would result in older radiocarbon ages. The samples, which were dated using both methods, however, seem to agree well. Regarding the possibility of open-system conditions for carbon, it is certainly difficult to assess with confidence the primary origin of the micrite and of some of the sparry fabrics, especially when composed of LMC. Microbial mats can induce the precipitation of any type of biominerals and LMC, independently of the environmental conditions of the lake. However, the presence of blocky mosaics of LMC and/or microspar observed in some of the samples suggests that the stromatolites underwent at least some degree of recrystallization.

In order to evaluate the potential effect of recrystallization on the stromatolite ages, we attempted to reproduce the lake-level curve using the Monte Carlo model and selected samples with different percentages of primary carbonates (Figure 11). We observed that the general pattern of the lake-level curve is rather similar for the different samples, displaying a highstand period at ∼29 ka (Figure 11). This experiment suggests that despite of the potential effects of diagenesis, the trend and overlap of the U-series and radiocarbon ages during and after the highstand phase are persistent. Furthermore, if diagenesis was present, it apparently had a minor impact as the isochron approach highlighted a linear relationship (Figure 5), which would not be the case under the influence of open-system conditions. Furthermore, there are no younger stromatolite radiocarbon ages compared to atmospheric radiocarbon ages (as derived at the U-series dated specimen), which would be an expected result if diagenesis had a major influence on the stromatolites. Additionally, geomorphic observations and radiometric dating suggest that the younger shorelines (<29 ka) were not reoccupied; they represent a period of continuous lake drop. This implies that after their formation, the stromatolites were continuously exposed above the water level. The absence of water reduces the rate of carbonate recrystallization because water facilitates the dissolution and reprecipitation process essential for transforming aragonite to calcite. To reconciliate the effect of

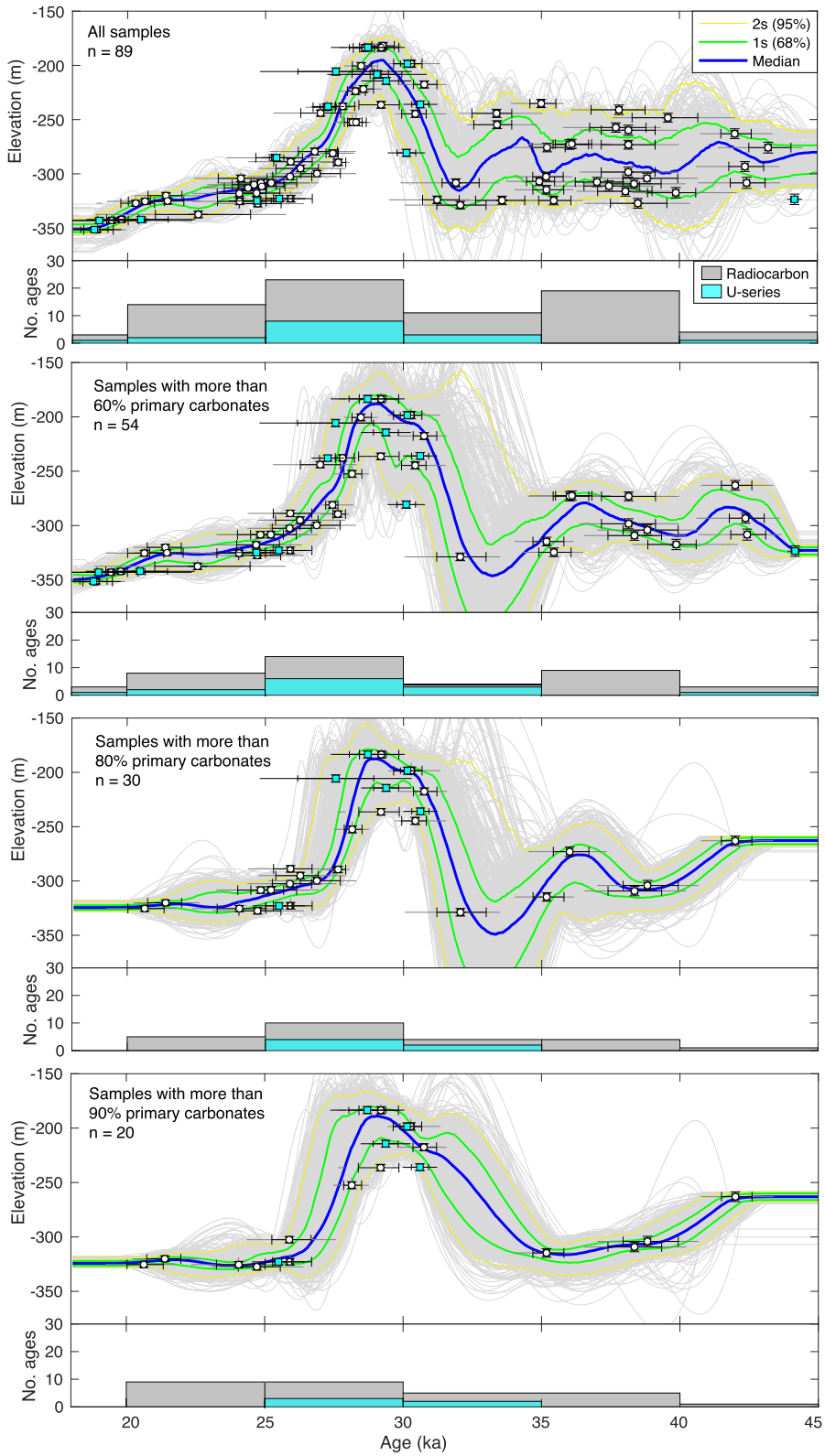

Figure 11. Lake-level reconstructions using samples with different percentages of primary carbonates. White-filled circles are radiocarbon samples and blue filled squares represent U-series samples. n: number of samples.

recrystallization and the observed agreement between ages, we propose that some degree of recrystallization probably occurred during or shortly after subaerial exposure (early diagenesis). This probably affected the ages but of a lesser magnitude than their associated uncertainties.

Alternatively, paleo-shorelines can be viewed as isochronous lines, making them valuable for assessing the accuracy of radiocarbon dating and the impact of recrystallization, which could lead to significant age discrepancies among coeval samples. To investigate this, we analyzed 12 samples from six paired locations along a single paleo-shoreline. Our findings reveal consistently similar ages within the respective uncertainty intervals of the samples (refer to Figure SP10 in Supporting Information S1). We therefore suggest that fossil stromatolites can provide reliable temporal and spatial information and that they can be used as lake-level index points for reconstructing lake-level variations in the Dead Sea depression.

5.3. Comparison of the Stromatolite-Based Lake-Level Curve With Previous Studies

5.3.1. Stratigraphy of the Lisan Formation and the Stromatolite-Based Lake-Level Curve

To evaluate the consistency of our results, we compared the lake-level reconstructions derived from the Lisan Formation and the chronostratigraphy of the Lisan Formation itself with the stromatolite-based lake-level reconstruction. The best exposures of the Lisan Formation are in the Perazim Creek and at Masada (Figure 12a), where it comprises three dated stratigraphic units or members (Bartov et al., 2002; Haase-Schramm et al., 2004; Machlus et al., 2000; Stein, 2001). The lower member is ∼5 m thick and consists of laminated aragonite-detritus with an age between ∼70 and 55 ka. This member is overlain by distinctive gypsum layers of 3–5 m thick that is in turn overlain by the ∼25 m thick, ∼48-31 ka middle member, which is coeval with the pre-highstand phase in our lake-level reconstruction (Figure 12b). The middle member consists of intercalations between laminated and coarse facies such as sand, gravel, pebbles and silty detritus, which has been interpreted as a low lake-level period (Bartov et al., 2002, 2003; Torfstein, Goldstein, Kagan, Stein, & Enzel, 2013). Similarly, we associate the presence of clastic material with a relatively low lake-level (∼-360 m) overprinted by low-amplitude and high-frequency lake-level oscillations that occurred prior to 30 ka. However, Torfstein, Goldstein, Kagan, and Stein (2013) interpreted the middle member differently, extending its duration between ∼60 and ∼39 ka. According to these authors, the middle member is capped by a gypsum intercalation defined as the broken gypsum unit, which is present in Masada and other sections northward but not at Perazim Creek. We can tentatively correlate the broken gypsum with a short lake-level drop occurred between ∼41 and ∼39 ka in our lake level curve.

The upper member is 10–20 m thick and consists mostly of laminated aragonite detritus with ages ranging between ∼31 and 18 ka (Bartov et al., 2002; Torfstein, Goldstein, Kagan, Stein, & Enzel, 2013), coeval with the highstand and post-highstand periods of our lake-level reconstruction. Nevertheless, Torfstein, Goldstein, Kagan, and Stein (2013) interpreted the age of the upper member between ∼39 and ∼15 ka, which includes part of the pre-highstand, highstand and post-highstand periods of our lake level curve. According to the stratigraphic descriptions of Torfstein, Goldstein, Kagan, and Stein (2013), at PZ1 this member comprises intercalations of halite layers between ∼30 and ∼37 ka representing lowstand conditions, which can be tentatively correlated with the sharp fall in water level that occurred at ∼32 ka in our lake level curve (Figures 12b and 12g). The laminated facies of the upper member have been previously considered to be associated with the paleolake Lisan highstand (e.g., Bartov et al., 2002; Torfstein, Goldstein, Kagan, & Stein, 2013), considering that the presence of laminated aragonite indicates offshore depositional environments and that aragonite precipitation requires the addition of bicarbonate-rich freshwater (e.g., Stein et al., 1997) (see Section 2.2). The presence of laminated aragonite in the upper Lisan Formation is therefore difficult to explain in the context of the sharp fall in lake level resulting from our stromatolite-based lake-level reconstruction.

However, recent studies suggest that aragonite deposition is not solely controlled by lake and runoff waters but also by the contribution of carbonate dust that may be dissolved in the runoff (Belmaker et al., 2019). The dissolution of calcite dust blown from the Sahara and adjacent deserts can be a viable source of bicarbonate, and might explain the thick laminated aragonite sequence in the upper member. Furthermore, this is also in accordance with speleothem records that indicate drier and colder conditions during the LGM, which were associated with higher dust input in the Levant region (Frumkin & Stein, 2004). The upper member is capped by two prominent gypsum layers with an age of ∼16 ka (Bookman et al., 2006; Haase-Schramm et al., 2004; Stein, 2001;

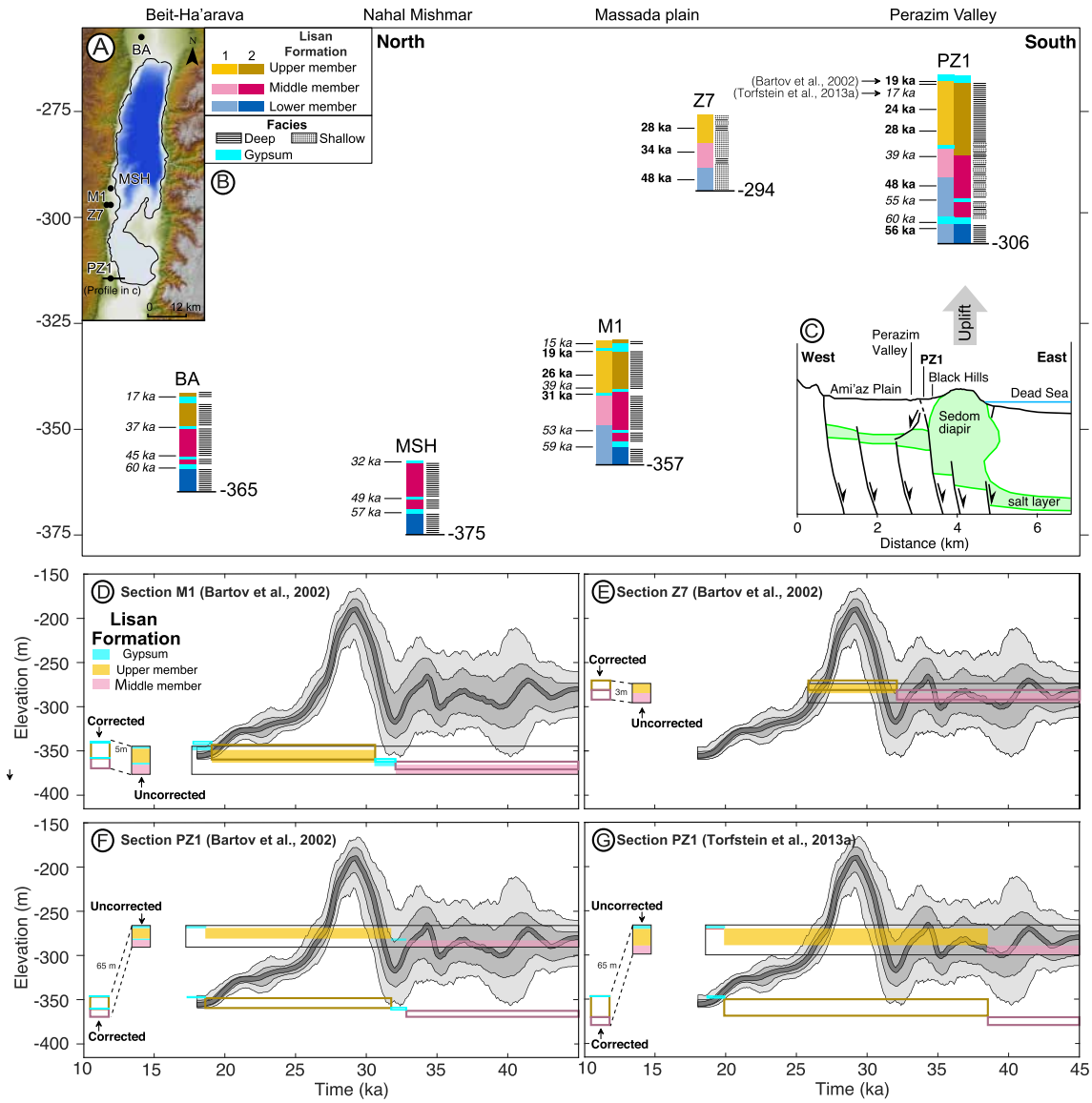

Figure 12. Comparison of the stratigraphy of the Lisan Formation with our stromatolite-based lake-level curve. (a) Location of stratigraphic sections along the western coast of the Dead Sea. (b) Simplified stratigraphic sections modified from Torfstein, Goldstein, Kagan, and Stein (2013) and Bartov et al. (2002). BA: Beit Ha'arava, MSH: Nahal Mishmar, M1 and Z7: Masada, PZ1: Perazim Creek. The elevation of the base of each section is indicated by a black line. 1: members by Bartov et al. (2002), 2: members by Torfstein, Goldstein, Kagan, and Stein (2013). (c) Schematic geological profile at Mt. Sedom indicating the position of PZ1 modified after Weinberger, Begin, et al. (2006). (d–g) Position of corrected and uncorrected stratigraphic section with respect to our stromatolite-based lake-level curve. The filled semi-transparent stratigraphic sections represent the original uncorrected elevations, and the color-outlined sections are vertically corrected using uplift or subsidence (See text for details).

Torfstein, Goldstein, Kagan, & Stein, 2013), which are coeval with the minimum lake-level positions (~-360 m) in our lake-level curve (Figures 12b–12d, 12f and 12g).

Bartov et al. (2002) inferred a lake level drop at ~28 ka based on sequential stratigraphy of the upper stratigraphic sections at the Masada plain (Section Z7), which agrees with the lake level drop observed in our reconstruction (Figure 12e). Nevertheless, these facies are subsequently overlain by ˜2m thick deep lake facies that evince a subsequent lake level rise. Distinguishing between shallow and deep lacustrine environments based on facies may be particularly difficult because the Lisan Formation lacks any trace fossils that could be used to support paleo-environmental interpretations. In this regard, in the present-day beach environments of the Dead Sea, it is possible to find layered aragonite-detritus, associated with bacterial mats in ponds near the coastline, with a similar laminated structure as those of the upper member of the Lisan Formation (Thomas et al., 2016), suggesting that

laminated facies may not be exclusively dependent on depth but also on local energy conditions and water chemistry. On the other hand, the lake level was about 60 m higher than section Z7 between 30 and 26 ka (Figure 12e), which probably resulted in the accumulation of deep lake sediments. The intercalations of deep facies overlaying shallow facies described by Bartov et al. (2002) may be possibly linked to the lake highstand period identified in our reconstruction or alternatively, sedimentation in a distal pond perched above the lake level.

Previously studied stratigraphic sections of the Lisan Formation along the Dead Sea coast are distributed at rather similar elevations (Torfstein, Goldstein, Kagan, & Stein, 2013) with differences of <10 m, except for sections Z7 and PZ1 (Figure 12b). Section Z7 is characterized by shallow sedimentary facies and is located toward the edge of the basin and approximately below our lake-level curve (Figure 12e). Instead, PZ1 is characterized by deep facies (Upper member; Figure 12a) and is located several meters above our lake-level curve (Figures 12f and 12g). We note that the ∼30 to ∼16 ka upper member of the PZ1 section in the Perazim Creek is located 30–60 m above the post-highstand interval of our lake-level reconstruction (Figures 12f and 12g), suggesting that the lake-levels of our reconstruction are underestimated (Figure 12b).

The PZ1 section is located in the Ami'az plain adjacent to Mount Sedom (Figure 12c), a salt diapir that has been actively uplifting since the late Pleistocene (Frumkin, 2009; Weinberger, Begin, et al., 2006). There have been no previous vertical deformation-rate estimates in the Perazim Valley and Ami'az plain; however, the area is characterized by the presence of radial clastic dikes cutting through the Lisan Formation and associated with the salt intrusion. The dikes converge toward the Black Hills area, whose topography and cumulative dike width suggest 70 to 50 m of local uplift (Marco et al., 2002). In this regard, the difference between our curve and PZ1 could be a result of differential subsidence/uplift between PZ1 and the sections northward. We would expect that areas that have undergone faster subsidence would display thicker sedimentary sequences associated with the Lisan Formation because of increased accommodation space. However, the M1, MSH and BA sections within the Lisan Formation are 10–20 m thinner than in PZ1 (Figure 12a). A possible explanation would be that differential subsidence/uplift occurred after the deposition of the Lisan Formation at ∼16 ka. Interestingly, this age has also been suggested for the rise of Mount Sedom (Frumkin et al., 2009; Weinberger et al., 2006; Zucker et al., 2019).

After correcting the elevation of the M1 section using the 0.3 m/kyr mean subsidence rate at Masada (Bartov, Agnon, et al., 2006) and an arbitrary subsidence rate of 0.2 m/Kyr for Z7, considering subsidence rate decrease westwards (Bartov et al., 2002; Bartov, Agnon, et al., 2006), we notice that M1 and Z7 are relocated 5 and 3 m above its original position, respectively, but still below the reconstructed lake-level curve (Figures 12d and 12e). We observe that the difference between the corrected elevation of M1 and the uncorrected PZ1 (−306 m) is ∼65 m. Under the assumption that both sections were deposited at similar depths and that differential subsidence/uplift occurred after 16 ka, this difference in elevation would suggest that PZ1 experienced an uplift rate of ∼4 m/Kyr. When correcting PZ1 with this rate, we note that the upper member is relocated below the stromatolite-based lake-level reconstruction (Figures 12f and 12g). This differential uplift scenario of the Ami'az plain agrees with the 70 m uplift at Black Hills (Marco et al., 2002) and reconciles the vertical differences between the stromatolite-based lake-level reconstruction and the section PZ1.

5.3.2. Comparison With Previous Lake-Level Reconstructions

We compared the stromatolite-based lake-level reconstruction with previous lake-level curves and proxies based on the stratigraphy of the Lisan Formation in order to evaluate and interpret similarities and differences. We selected the lake-level curves of Torfstein and Enzel (2017) and Bartov, Agnon, et al. (2006), which are the most detailed lake-level reconstructions over the period covered by our investigations. The curve of Bartov, Agnon, et al. (2006) is based on sequence stratigraphy of the Lisan Formation at Masada and in the Perazim Creek, aided by a combination of U-series and radiocarbon ages and corrected for tectonic subsidence (−0.3 m/kyr) at Masada. The curve of Torfstein, Goldstein, Kagan, Stein, and Enzel, (2013) and its updated version in Torfstein and Enzel (2017) is also based on the stratigraphy and chronology of the Lisan Formation and a compilation of lake-level indicators; it is vertically tied to the lake-level curve of Bartov, Agnon, et al. (2006) and the age of fossil stromatolites from caves around the Dead Sea (Lisker et al., 2009). To facilitate the comparisons, we subdivided the lake-level history of the Lake Lisan-Dead Sea system into three intervals based on our lake-level reconstruction. The pre-highstand interval between 31 and 45 ka, the highstand interval between 31 and 28.5 ka, and the post-highstand interval between 28.5 and 18 ka (Figure 12b).

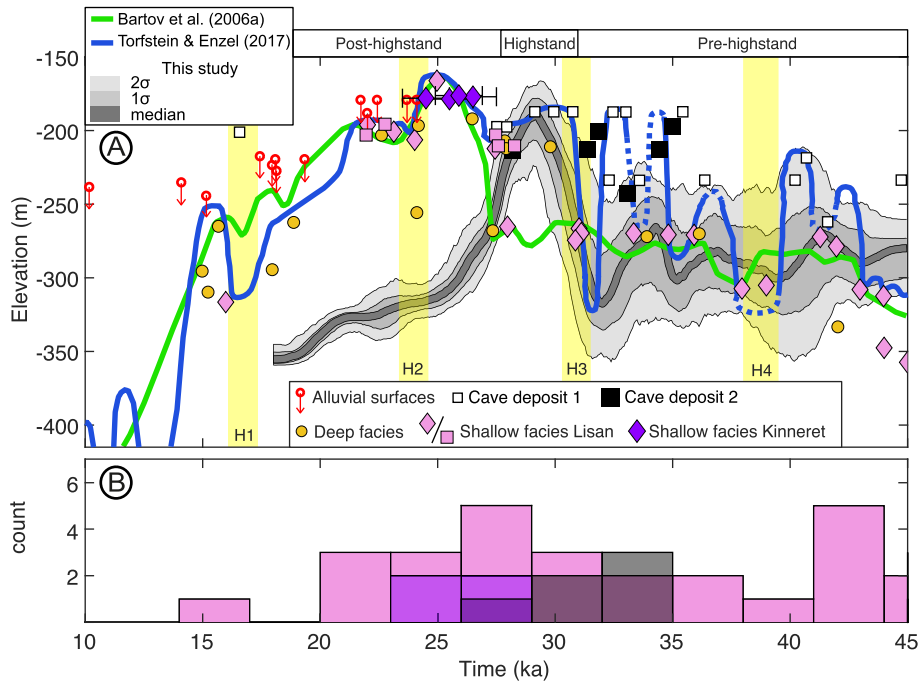

Figure 13. Comparison between our lake level reconstruction, previous lake-level curves and proxies. (a) Lake-level curves of Bartov, Agnon, et al. (2006), Torfstein and Enzel (2017), our stromatolite-based lake-level reconstruction and other lake-level proxies. Symbols are lake-level indicators of deep and shallow environments based on the compilation of Torfstein and Enzel (2017), corrected for tectonic subsidence. Cave deposits 1: single sample U-series ages. Cave deposits 2: isochron and averaged single sample U-series ages, both from Lisker et al. (2009). The dashed intervals in the blue curve indicate that the reconstruction is not robust. The gray colored curve in the background is the stromatolite-based lake-level reconstruction and confidence intervals. The yellow bands represent Heinrich stadials (h). Rosa diamonds and squares are shallow facies of the Lisan Formation by Bartov, Agnon, et al. (2006) and Bartov (2004), respectively. Purple diamonds are shallow facies described by Hazan et al. (2005) at the site Tel Qazir near Lake Kinneret. (b) Histogram of shallow water lake level indicators, including shallow facies (rosa and purple) and isochron dated cave deposits (black). Note the scarcity of shallow indicators between 25 and 15 ka.

For the pre-highstand interval, our lake-level reconstruction and the lake-level curve of Bartov, Agnon, et al. (2006) overlap for the entire interval with a similar pattern of low-amplitude and high-frequency lake-level variations. The curve of Torfstein and Enzel (2017) indicates higher amplitude lake-level oscillations than our reconstruction, with vertical maximum differences of ~50 m, however, within intervals where the reconstruction is not robust (Figure 13a). Despite of these differences, there is a notable match in the polarity of lake-level oscillations between both lake-level reconstructions, for instance during the cold Heinrich (H) stadial H4 (Figure 13a). The oscillations also involve an episode of a fast decrease during H3 at about the same time as suggested by our lake-level reconstruction and reaching a similar elevation (~-320 masl, Figure 13a). The highstand interval of our reconstruction matches approximately with the beginning of the highstand interval in the reconstruction of Torfstein and Enzel (2017), both reaching ~-180 m. Instead, in the lake-level curve of Bartov, Agnon, et al. (2006), this event occurs ~5 Kyrs later than in our reconstruction and the one by Torfstein and Enzel (2017). The post-highstand interval shows the greatest dissimilarities between our and the other two lake-level reconstructions, particularly regarding the duration of the Lake Lisan highstand. According to our reconstruction, lake regression started at ~28.5 ka, that is, ~5 Kyrs earlier than previously suggested, resulting in maximum vertical differences of ~140 m during the H2 interval at ~25 ka. On the other hand, Hazan et al. (2005) reported radiocarbon ages from the Lake Kinneret sediments, including the Lisan highstand at 24–27 ka (Figure 13a). These ages, however, conflict with our lake level reconstruction, suggesting a higher lake level during the post-highstand period. Importantly, these ages were obtained solely from the Tel Qazir site near the Kinneret-Lisan separation sill. Additionally, Hazan et al. (2005) acknowledged a large (3 Kyrs) reservoir effect at Tel Qazir, raising uncertainty. In addition, Hazan et al. (2005) used the radiocarbon calibration curve from 1998. When using the Intcal2020 calibration curve (Reimer, 2020) and applying a 1500 years of reservoir effect for the

Melanopsis, none of the Tel Qazir samples would be younger than 25ka and some of them would fit our dated lake level peak. Due to these limitations, the validity of the Tel Qazir highstand records remains inconclusive. Finally, during the youngest part of the post-highstand our reconstruction and the lake-level curve of Torfstein and Enzel (2017) tend to converge toward H1 with vertical differences reaching ∼20 m. The observed ∼140 m difference could be due to a variety of mechanisms, first related to a problem with the radiocarbon dating; second, vertical displacements that have not been considered in our or previous corrections; and third, potential inaccuracies of previous lake-level reconstructions, as discussed below.

Regarding the first possibility calibration issues may produce consistent temporal offsets and older radiocarbon ages. However, there is no consistent temporal offset visible in the age distribution. For example, the pre-highstand and highstand intervals match the previous lake-level reconstructions relatively well, while the post-highstand intervals show bigger differences. Furthermore, as explained in Section 5.2, the effect of diagenesis seems to have most likely only a negligible effect on the radiometric dating results. But, even if the quality of the radiocarbon ages had been affected by an unidentified process, the effects of such a process would be reflected in an increase in scatter; instead, our reconstruction reveals a distinct trend between 30 and 18 ka as well as consistency with the new U-series ages. We therefore discard the possibility that faulty radiocarbon calibration is responsible for the differences between our lake-level reconstruction and the previous lake-level curves. Another reason for the difference between lake-level curves could be the uncertainty in the radiocarbon ages used in the reconstruction of Bartov et al. (2002). The authors used the "Lisan calibration curve" and 1 Kyr RA based on Schramm et al. (2000) to correct the radiocarbon ages. We tentatively corrected the original ages from Bartov et al. (2002) using a more recent atmospheric calibration curve (Intcal2020, Reimer (2020)) and the RA from fossil stromatolites. On average, the corrected ages differ <1 Kyr from the original corrections, which is insufficient to explain the differences between our reconstruction and the previous lake-level curves.

With respect to the second possibility, we note that subsidence could occur as a result of crustal loading associated with an increase in water depth. However, even assuming the existence of an unreasonably thin lithosphere, a difference of 100–140 m between lake-level reconstructions cannot be explained by hydro-isostasy. On the other hand, Bartov, Agnon, et al. (2006) suggested that Late Pleistocene subsidence rates at Masada vary between 0.6 and 0.3 m/Kyr increasing toward the basin center. In this regard, our stromatolites at the nearest site, Mishmar, are located northwards of the Masada plain and toward the west. By extrapolating the western edge of the Masada plain northwards, the site Mishmar would be located within the peripheral area of the basin and probably subject to subsidence rates of 0.3 m/Kyr. On the other hand, the work of Lisker et al. (2009) considers the elevations of stromatolites in caves located distant from the basin center and westwards of our stromatolite sites. This author suggests lake stands up to 80 m higher than previously proposed during the paleolake Lisan period, corresponding to 2.2 m/Kyr subsidence rates for areas toward the basin center. However, even considering the subsidence rates by Lisker et al. (2009) or higher, they are insufficient to explain the vertical difference observed between lake-level curves, as shown by sensitivity tests (Figure SP9 in Supporting Information S1). The reconstruction by Torfstein, Goldstein, Kagan, and Stein (2013) and Torfstein and Enzel (2017) improved the vertical accuracy of the lake-level reconstruction using fossil stromatolites from caves, presumably formed close to the former lake-levels that reached the cave elevation in order to deposit stromatolites (Lisker et al., 2009). However, the position of the water table in relation to the water level in the lake may have varied depending on the local coastal slope, chemical contrasts, and variations in permeability (Kafri & Yechieli, 2010). This could have favored the formation of freshwater ponds inside the caves and the growth of stromatolites at higher elevations than the lake-level. On the other hand, some stromatolites could have grown when the caves were flooded and below the lake-level (Lisker et al., 2009). These factors add further uncertainty to the cave position with respect to the lake-level and may explain some of the vertical differences between our reconstruction and the lake-levels of Torfstein and Enzel (2017).

Third, while recognizing the enormous effort and the resulting high temporal resolution of previous lake-level reconstructions, there are a number of possible inaccuracies that could increase their vertical uncertainty. For instance, the shallow water lake level indicators described by Bartov et al. (2002) and other authors are generally older than 25 ka (Figure 13a), and the ages of the shallow lacustrine deposits during the highstand of this reconstruction are only constrained by a small number of samples (Figure 13b). Additional observations of shallow and subaerial facies during the Lake Lisan highstand were included in later studies (Bartov et al., 2003; Bartov, Agnon, et al., 2006) but no details were reported concerning their nature, age, or the dating method used. In this regard, the PhD thesis of Bartov (2004) describes an additional site at Yizrah. The ages obtained by Bartov

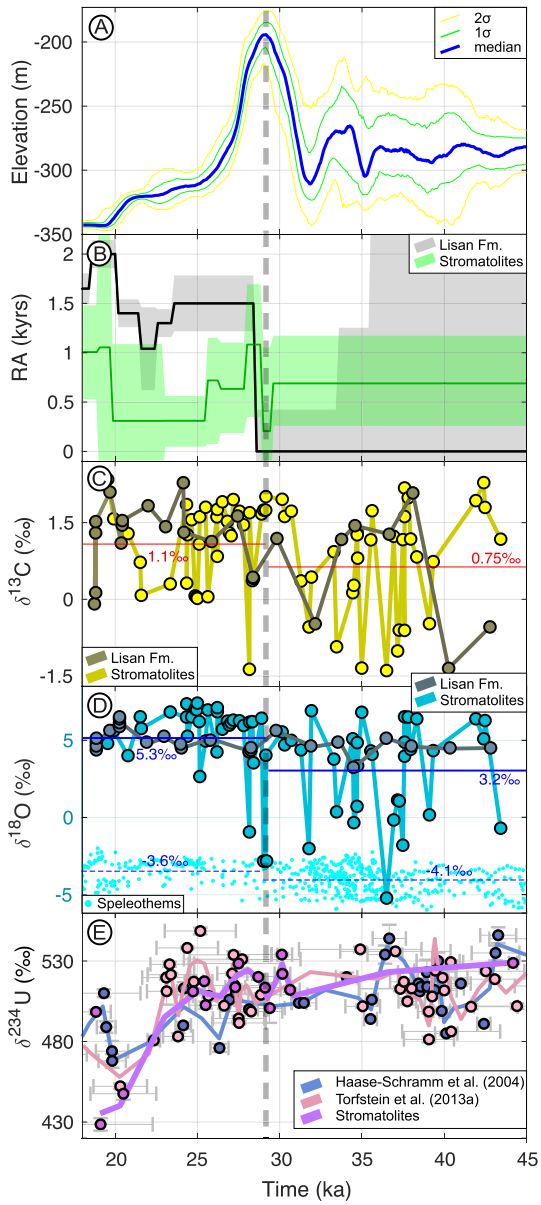

Figure 14. Comparison of paleoclimatic proxies and the lake-level curve based on fossil stromatolites. (a) Lake level curve based on fossil stromatolites, (b) Radiocarbon reservoir ages (RA). The colored bounds are the 1-sigma confidence intervals of RA, and the black line and gray shaded area are based on a compilation of RA estimates (Prasad et al., 2004, 2009; Schramm et al., 2000; Stein et al., 2004; Van der Borg et al., 2004). (c) and (d) Carbon and oxygen stable isotopes from stromatolites and Lisan Formation, Gray markers and lines in c and d are stable isotopes in the PZ1 section from Kolodny et al. (2005). Red lines in c are the median $\delta^{13}C$ values. The solid blue lines in d mark mean $\delta^{18}O$ values from stromatolites, the blue dashed lines in d denote mean values from the speleothems, including records from Soreq (Bar-Matthews et al., 1999); Ma'ale Efrayim (Vaks et al., 2003); Tzavoa (Vaks et al., 2006); Peqiin (Bar-Matthews et al., 2003); Zalmon (Keinan et al., 2019) caves. (e) $\delta^{234}U$ values of the Lisan Formation (Haase-Schramm et al., 2004; Torfstein, Goldstein, Kagan, & Stein, 2013) and the fossil stromatolites.

in the sequences of Lisan Formation in the Yizrah basin display ages between 22 and 28.2 ka at elevations between −213 and −194 m (Figure 13a). These ages diverge from our lake level reconstruction, suggesting higher lake-levels. Interestingly, the paleoshorelines that we described at site Yizrah are directly east of the outcrops that Bartov (2004) analyzed. The higher shoreline is located at a lower elevation (−180 m) than the −165 m reach of the lake documented by Bartov (2004), but at higher elevation than the sequences of Lisan Formation. We clearly observe the lateral continuity between the Yizrah basin and the flat upper topographic surface immediately south and is capped by a crust of stromatolites that we dated at 29 ka. Bartov (2004) describes in his thesis this event that is, (translation from Hebrew): "the filling of the basin indicates a significant flooding about 28 thousand years ago that reached the edge of the basin up to a height of 165 m below sea level followed by a drying event." An interesting point not described by Bartov (2004) is the presence of an eroded sill at the northern outlet of the Yizrah basin. The presence of this sill suggests that during and the LGM the Yizrah basin probably persisted as an independent lake even under a decaying Lisan lake level. This adds an additional uncertainty to the chronology of the Lisan records at this site, specifically those younger than 27 ka, which may explain the difference between the ages of the Yizrah basin and our lake-reconstruction.

Finally, as shown in the compilation by Torfstein and Enzel (2017), apart from the fossil cave stromatolites and shallow facies, most of the chronological control for the paleolake Lisan highstand is based on deep lacustrine facies (Figures 13a and 13b), which suggests that there is likely to be some degree of uncertainty regarding their position in relation to the shoreline and the paleo-depth.

5.4. Lake-Level Changes and Paleoclimatic Proxies

The Lisan Formation and fossil stromatolites yielded variable isotopic values, which in addition to temporal variations in the RA, may reflect climatic control on the past limnological and hydrological activity in the Dead Sea depression (see Figures 14a–14f). We noted similar patterns of RA variability in the Lisan Formation and in the fossil stromatolites. The Lisan Formation mostly yielded higher RAs than the stromatolites (Figure 14b), except for the oldest RA from stromatolites (0.69 Kyrs), which is higher than the 0 kyrs estimated in previous studies (Haase-Schramm et al., 2004; Stein et al., 2004; Van der Borg et al., 2004) but still within the error range of these previous estimates (Figure 14b). Both, the RA from the Lisan Formation and from the stromatolites increase during the highstand period of our reconstruction to 1 and 1.5 Kyrs for the fossil stromatolites and the Lisan sediments, respectively. The abrupt increase in RAs suggests that the source of old carbon during this period may have been derived from freshwater that flowed or percolated through carbonate aquifers, transporting dissolved old inorganic carbon to the Dead Sea depression (e.g., Schramm et al., 2000). The RA from the Lisan Formation remained relatively constant until 23 ka (Haase-Schramm et al., 2004; Prasad et al., 2004; Van der Borg et al., 2004), while the RA from stromatolites decreased gradually between 28.5 and 25 ka, reaching a value of 0.28 Kyrs that lasted until 20 ka (Figure 14b). This decrease in the RA may be related to a reduction in the input of old carbon from freshwater sources and continuous interactions between the epilimnion and the atmosphere. After 20 ka, the RA from stromatolites increased to 0.9 Kyrs, which is lower than the 2 Kyrs RA estimated by Stein et al. (2004), Prasad et al. (2009, 2004), and

Haase-Schramm et al. (2004) for the Lisan Formation over the same period. We tentatively link the higher RA from the Lisan sediments with the effects of the meromictic conditions that existed during and after the Lake Lisan highstand. The shallow-water epilimnion where the stromatolites were formed probably interacted more effectively with the atmosphere, reducing the RA. In contrast, the sediments of the Lisan Formation were deposited in deeper waters within the confined hypolimnion, where the C-input from the atmosphere was less effective, which consequently resulted in higher RAs. However, it remains unclear why the RA from stromatolites and the Lisan Formation were similar during the highstand. This could possibly be related to the freshwater inflow; during periods of stable or rising lake-levels, enough freshwater may have entered the lake to produce a well-mixed water column and holomictic conditions.

The stable isotope composition of lake carbonates may yield information on temperature, precipitation, and lake productivity (e.g., Kolodny et al., 2005; Leng & Marshall, 2004; McCormack et al., 2019). The diverse factors controlling isotope values can, however, complicate direct climatic interpretations. The covariance between $\delta^{18}O$ and $\delta^{13}C$ can be useful for retrieving information on the residence time of lake water (Talbot, 1990) and evaporation (Leng & Marshall, 2004). However, as shown by previous analyses of stable isotopes in the Lisan Formation (Kolodny et al., 2005) and the results of our study, $\delta^{13}C$ and $\delta^{18}O$ values exhibit no clear covariance over centennial to millennial timescales (Figures 9a and 9b). This is possibly related to pronounced changes in water balance and high CO_2 from freshwater inflow, resulting in a lack of sensitivity of $\delta^{13}C$ to changes in lake volume (Kolodny et al., 2005; Li & Ku, 1997). However, covariance appears to exist over shorter timescales, as can be seen in Figure 9c. It is interesting to note that the sample that shows the covariance (JD1910) has an age of 31 ka, during the lowstand and associated with higher evaporation, while the sample that does not show any covariance (UJD192) has an age of 29 ka, which correlates with the highstand, thus providing additional evidence that water inflow may control the sensitivity of $\delta^{13}C$ at annual to millennial timescales.

In order to deconvolve the climatic signal of stable isotope variability, we further compared $\delta^{18}O$ from stromatolites with isotope records from the Lisan Formation (Kolodny et al., 2005). The $\delta^{18}O$ from stromatolites is depleted, with values ranging between −5 and 5‰, in contrast to the $\delta^{18}O$ from the Lisan Formation sediments, which range between 3 and 6‰ (Figure 14d). This difference may be related to the atmospheric interaction with the lake-water mixing zone, resulting in high $\delta^{18}O$ variability (e.g., Figure 10c). Although both these records have different temporal resolutions, they exhibit similar variability patterns and a slight but continuous increase in $\delta^{18}O$ during the post-highstand phase.

Previous studies of stable isotopes have suggested a link between $\delta^{18}O$ records from speleothems, $\delta^{18}O$ of marine deposits from the Eastern Mediterranean, and sediments from Lake Lisan (Frumkin et al., 1999; Kolodny et al., 2005), all of which are probably controlled by the "source effect", where variations in $\delta^{18}O$ may reflect the isotopic composition of their common marine reservoir. With regard to the isotope variability in the lake water, Katz et al. (1977) proposed that aragonites that precipitated from the more diluted paleolake Lisan water may have been more enriched in ^{18}O than those generated from lake-lowstand waters, such as during the Holocene. Gat (1984) also suggested that the $\delta^{18}O$ from paleolake Lisan was higher because the lake was more diluted. Likewise, Kolodny et al. (2005) suggested that during major lake regressions the steady-state condition is not achieved and high $\delta^{18}O$ values are established, as for instance, the higher $\delta^{18}O$ values measured at ∼20 ka, below the gypsum layer in PZ1, which represents a pronounced drying event (H1). Similarly, we observed relatively high $\delta^{18}O$ from stromatolites after the lake highstand (∼28–20 ka). In contrast, the highstand period itself exhibits a low $\delta^{18}O$ peak (−2.6‰, Figure 14d), which may relate to high rainfall, to high rates of freshwater inflow from the paleo-Jordan River, or to less effective evaporation. The rainfall during this period was also enriched in $\delta^{18}O$, as can be seen in the records from Soreq cave (Bar-Matthews et al., 1997, 2003). However, as indicated by Kolodny et al. (2005) and Frumkin et al. (1999), the source effect may reduce the validity of $\delta^{18}O$ as an independent climate indicator in speleothems, lake sediments, and probably in stromatolites as well.

On the other hand, the relative shift in $\delta^{18}O$ between speleothems and Lisan paleolake-surface waters derived from the stromatolites provides further evidence for strong evaporation during the period of decreasing lake levels. When comparing the mean $\delta^{18}O$ from speleothems in the Dead Sea depression (Figure 2d), we observed a shift from −4.1‰ in the pre-highstand period to −3.6‰ in the post-highstand. Instead, we observed a shift of mean $\delta^{18}O$ values between 3.2 and 5.1‰ for the stromatolites from the pre- and post-highstand lake-level phases, respectively. This change is about 1.5‰ larger compared to the speleothems and cannot be explained solely by the source effect. Given that the freshwater-isotope values in this region are fairly similar, another effect must be

inferred to account for this additional increase. The most meaningful explanation may involve the effects of evaporation during the post-highstand period, which could have contributed to the fast decrease in lake level after ~28 ka.

The $\delta^{13}C$ compositions from stromatolites display a rather similar pattern to those from the Lisan Formation (Kolodny et al., 2005), both ranging between −1.5 and 1.9‰, with gradually increasing trends toward the present (Figure 14c). Katz et al. (1977) suggested a link between an increase in the $\delta^{13}C$ of aragonite in the Lisan Formation and reductions in the Na/Ca ratio, possibly associated with evaporation and CO_2 loss, triggering carbonate precipitation. Kolodny et al. (2005) suggested that increases in the $\delta^{13}C$ may relate to increases in lake productivity and algal bloom, with ^{13}C being enriched as a result of ^{12}C removal from the lake water by photosynthesis, which is supported by the sparse occurrence of C3 vegetation during this period (Miebach et al., 2019). A similar scenario occurred during the Dead Sea overturn between 1975 and 1978, which was also associated with enhanced carbonate precipitation (Talma et al., 1997). The $\delta^{13}C$ values from fossil stromatolites were slightly higher during the post-highstand interval than during the pre-highstand period (Figure 14c), suggesting an increase in lake productivity and intensified carbonate precipitation during the period of falling water levels, a scenario which is consistent with the presence of aragonite-rich laminated facies in the upper member of the Lisan Formation. It remains unclear whether or not the increase in lake productivity alone would have been sufficient to explain the increase in the rate of aragonite deposition in the Lisan Formation, which was at least six times higher compared to the present day (Barkan et al., 2001). We propose that this increased rate of deposition may also have been controlled by an increase in calcite dust blown from the Saharan and surrounding deserts during the LGM (See Section 5.3.1).

The initial $\delta^{234}U$ is a climate proxy that may provide additional hydrologic and paleoclimatic information with respect to the relative proportions of groundwater and surface waters flowing into a lake or chemical weathering of rocks within the lake catchment area (e.g., McGee et al., 2012). Previous studies in the Dead Sea have shown that $\delta^{234}U$ values are strongly influenced by freshwater input. For instance, the present-day Dead Sea has $\delta^{234}U$ values of ~440‰, whereas the Jordan River has $\delta^{234}U$ values of ~700‰ (Haase-Schramm et al., 2004), and local springs along the western Dead Sea coast display varying $\delta^{234}U$ values of between 200 and 750‰ (Kronfeld et al., 1991). These observations suggest that freshwater sources generally contribute with high $\delta^{234}U$ values, while the lake brines have low $\delta^{234}U$ values. Furthermore, decreasing trends of $\delta^{234}U$ values have been observed in the Lisan Formation, preceding hiatuses and gypsum layers that marked periods of negative freshwater balance (Haase-Schramm et al., 2004). On the other hand, high $\delta^{234}U$ values of up to 800‰ were identified by Waldmann et al. (2007) in primary aragonites precipitated at about 80 ka, which were interpreted to reflect periods of high freshwater input.

Following these observations, the high and relatively stable $\delta^{234}U$ values of ~500‰, between 45 and 30 ka, recorded from both fossil stromatolites and the Lisan Formation sediments, suggest a stable or positive water balance. These values remained relatively constant until the highstand period, followed by a slight and progressive decrease of $\delta^{234}U$ values during the post-highstand period (Figure 14e). However, this change in $\delta^{234}U$ is not as sharp as would be expected for the pronounced lake drop in our lake-level reconstruction. In this regard, the paleoclimatic interpretations based on $\delta^{234}U$ variability can be very complex, especially in the Dead Sea basin. We propose two possible mechanisms that could explain the unexpected high $\delta^{234}U$ values despite the sharp lake drop recorded by the fossil stromatolites: (a) Lake drop can occur by decrease of rainfall and run off, by increased evaporation, or by a combination of both. As indicated previously, the main source of $\delta^{234}U$ comes from rivers and freshwater input; if the Lisan Lake was affected by high evaporation rates and the runoff remained relatively constant, then we would expect no correlation between lake level drop and $\delta^{234}U$. (b) During high lake levels, it is possible that $\delta^{234}U$ from other sources can enter the lake. For instance, the redissolution of evaporites with high $\delta^{234}U$ can act as a secondary source of $\delta^{234}U$, this could buffer the drop of $\delta^{234}U$ during the post-highstand period.

5.5. Climatic Implications in the Levant

Our results provide additional data for a large body of investigations on the late Pleistocene lake-level changes in the Dead Sea depression. Combined, this information has implications for the previously proposed global-scale forcing mechanisms that may have influenced the magnitude and timing of lake-level variations. Because of lower temperatures during the LGM, it has been suggested that the resulting enhanced latitudinal thermal gradient led to an increase in the intensity and frequency of cyclones in the eastern Mediterranean (Enzel et al., 2008). This

mechanism would have resulted in an increase in the amount of moisture delivered to the southern Levant and may therefore have caused high lake levels in the Dead Sea depression. On the other hand, $\delta^{18}O$ records from speleothems indicate drier and colder conditions during the LGM compared with the Holocene (Bar-Matthews et al., 1997, 1999). Pollen records from the ICDP core in the Dead Sea also suggest a reduction in rainfall of about ∼30% over the Dead Sea depression, and hence arid conditions during the LGM (Miebach et al., 2019). Furthermore, at a more regional scale, paleoclimate studies in the central and western Mediterranean suggest that sea-surface salinity was higher during the LGM than at present (e.g., Emeis et al., 2000; Kallel et al., 1997), also indicating dry, more evaporative conditions. In this context, it is interesting that the northern Red Sea also appears to have experienced cooler temperatures and increased salinity during the LGM (Arz et al., 2003). Finally, global circulation models suggest drier conditions in the Levant during the LGM (Robinson et al., 2006). Our lake-level reconstruction suggests that the beginning of the LGM was wet (30–28.5 ka), immediately followed by a period drier than previously envisaged. This interpretation agrees in part with the above-mentioned proxy records, while it partly agrees with the notion of a wet LGM proposed by others. Our results thus reconcile the apparent discrepancy between a Dead Sea highstand during times of increased aridity. This study further highlights the importance of assessing the temporal and spatial uncertainties involved in lake-level reconstructions and the applicability of combined multi-proxy data to estimate paleo lake-level positions and their associated uncertainties.

6. Conclusions

In this study, we re-examined the lake-level changes during the transition between paleolake Lisan and the Holocene Dead Sea using lake-level index points based on fossil stromatolites and the morphometry of lake paleo-shorelines. Our results can be summarized as follows.

1. We surveyed and sampled lake paleo-shorelines in eight areas distributed along the eastern and western coasts of the Dead Sea, collecting 84 samples for radiocarbon dating and 15 samples for U-series dating of in situ fossil stromatolites.
2. Temporal corrections were applied based on radiocarbon age reservoirs derived from paired U-series and radiocarbon ages and isochrons for U-series ages. Vertical corrections were applied considering the effect of hydro-isostatic adjustments and vertical tectonic displacements.
3. Our lake-level reconstruction suggests a pre-highstand period (45–32 ka) characterized by high frequency lake-level variations, a highstand period (30–28.5 ka) that lasted for ∼2 Kyr reaching −180 masl, and a post-highstand period (28.5–18 ka) that involved a rapid lake-level drop. The transition between paleolake Lisan and the Dead Sea occurred ∼5 Kyrs earlier than estimated by previous reconstructions.
4. Paleoclimatic proxies such as stable isotopes, radiocarbon reservoir age, and uranium isotopic ratios based on analyses of fossil stromatolites suggest low inflow and high evaporation during the Lisan post-highstand period, which is in good agreement with the pattern of lake-level changes in our reconstruction.
5. Our results suggest initial wet conditions during the LGM in the Dead Sea basin followed by abrupt drier conditions, which reconcile the apparent discrepancy between a Dead Sea highstand during times of increased aridity.

Data Availability Statement

The Matlab® scripts and formatted data used for the analyses and the creation of the main figures of this study are deposited in the Zenodo database via Jara-Muñoz (2023).

Acknowledgments
This study was supported by the Deutsche Forschungsgemeinschaft (DFG) project "LIFE", Grant JA2860/1-2. This project was also supported by the German–Israeli Foundation for Scientific Research and Development "GIF", Grant I-1280-301.8/2014. D.M. was supported by the Millennium Scientific Initiative (ICM) of the Chilean government through Grant C160025 "Millennium Nucleus CYCLO The Seismic Cycle Along Subduction Zones." We would like to thank Arnold Barach and Roland Freisleben for their help in the field, Prof. Adi Torfstein for introducing us into the geology of the Dead Sea and Prof. Regina Katsman for her feedback. We would also like to thank Christina Fisher for their help preparing the slabs and thin sections of fossil stromatolites and Christina Günther for her help with the analysis and interpretation of microprobe and X-ray diffraction data. We would like to thank Dr. Daniel Petrash for his insightful review and the anonymous reviewers that helped to improve this manuscript.

References

Arz, H. W., Pätzold, J., Müller, P. J., & Moammar, M. O. (2003). Influence of Northern Hemisphere climate and global sea level rise on the restricted Red Sea marine environment during termination I. *Paleoceanography*, *18*(2). https://doi.org/10.1029/2002pa000864

Barkan, E., Luz, B., & Lazar, B. (2001). Dynamics of the carbon dioxide system in the Dead Sea. *Geochimica et Cosmochimica Acta*, *65*(3), 355–368. https://doi.org/10.1016/s0016-7037(00)00540-8

Bar-Matthews, M., Ayalon, A., Gilmour, M., Matthews, A., & Hawkesworth, C. J. (2003). Sea–land oxygen isotopic relationships from planktonic foraminifera and speleothems in the Eastern Mediterranean region and their implication for paleorainfall during interglacial intervals. *Geochimica et Cosmochimica Acta*, *67*(17), 3181–3199. https://doi.org/10.1016/s0016-7037(02)01031-1

Bar-Matthews, M., Ayalon, A., & Kaufman, A. (1997). Late Quaternary paleoclimate in the eastern Mediterranean region from stable isotope analysis of speleothems at Soreq Cave, Israel. *Quaternary Research*, *47*(2), 155–168. https://doi.org/10.1006/qres.1997.1883

Bar-Matthews, M., Ayalon, A., Kaufman, A., & Wasserburg, G. J. (1999). The Eastern Mediterranean paleoclimate as a reflection of regional events: Soreq cave, Israel. *Earth and Planetary Science Letters*, *166*(1–2), 85–95. https://doi.org/10.1016/s0012-821x(98)00275-1

Bartov, Y. (2004). *Sedimentary fill analysis of a continental basin -the late Pleistocene Dead Sea [Ph.D. thesis]* (p. 126). The Hebrew University of Jerusalem.

Bartov, Y., Agnon, A., Enzel, Y., & Stein, M. (2006). Late quaternary faulting and subsidence in the central Dead Sea basin. *Israel Journal of Earth Sciences*, *55*(1), 18–31. https://doi.org/10.1560/k74u-0772-1642-6282

Bartov, Y., Bookman, R., & Enzel, Y. (2006). Current depositional environments at the Dead Sea margins as indicators of past lake levels. *Geological Society of America Special Paper*, *401*, 127–140. https://doi.org/10.1130/2006.2401(08)

Bartov, Y., Goldstein, S. L., Stein, M., & Enzel, Y. (2003). Catastrophic arid episodes in the Eastern Mediterranean linked with the North Atlantic Heinrich events. *Geology*, *31*(5), 439–442. https://doi.org/10.1130/0091-7613(2003)031<0439:caeite>2.0.co;2

Bartov, Y., Stein, M., Enzel, Y., Agnon, A., & Reches, Z. e. (2002). Lake levels and sequence stratigraphy of Lake Lisan, the late Pleistocene precursor of the Dead Sea. *Quaternary Research*, *57*(1), 9–21. https://doi.org/10.1006/qres.2001.2284

Begin, Z. B., Broecker, W., Buchbinder, B., Druckman, Y., Kaufman, A., Magaritz, M., & Neev, D. (1985). *Dead Sea and Lake Lisan levels in the last 30 000 years, a preliminary report*. Report GSI/29/85 (p. 18). Geological Survey of Israel, Jerusalem.

Belmaker, R., Lazar, B., Stein, M., Taha, N., & Bookman, R. (2019). Constraints on aragonite precipitation in the Dead Sea from geochemical measurements of flood plumes. *Quaternary Science Reviews*, *221*, 105876. https://doi.org/10.1016/j.quascirev.2019.105876

Ben-Avraham, Z., Lyakhovsky, V., & Schubert, G. (2010). Drop-down formation of deep basins along the Dead Sea and other strike-slip fault systems. *Geophysical Journal International*, *181*(1), 185–197. https://doi.org/10.1111/j.1365-246x.2010.04525.x

Bentor, Y., & Vroman, A. (1960). *Geological map of Israel, 1: 100,000* (p. 117). Geological Survey of Israel.

Blanckenhorn, M. L. P. (1912). *Naturwissenschaftliche Studien am Toten Meer und im Jordental: Bericht über eine im Jahre 1908 (im Auftrage SM des Sultans der Türkei Abdul Hamid II. und mit Unterstützung der Berliner Jagor-Stiftung) unternommene Forschungsreise in Palästina, Friedlander*. R. Friedländer & Sohn.

Bookman, R., Bartov, Y., Enzel, Y., & Stein, M. (2006). Quaternary lake levels in the Dead Sea basin: Two centuries of research. *Geological Society of America Special Paper*, *401*, 155–170. https://doi.org/10.1130/2006.2401(10)

Bookman Ken Tor, R., Enzel, Y., Agnon, A., & Stein, M. (2004). Late Holocene lake levels of the Dead Sea. *Geological Society of America Bulletin*, *116*(5–6), 555–571. https://doi.org/10.1130/b25286.1

Bookman, R., Filin, S., Avni, Y., Rosenfeld, D., & Marco, S. (2014). Possible connection between large volcanic eruptions and level rise episodes in the Dead Sea Basin. *Quaternary Science Reviews*, *89*, 123–128. https://doi.org/10.1016/j.quascirev.2014.02.009

Bookman, R., Lazar, B., Stein, M., & Burr, G. (2007). Radiocarbon dating of primary aragonite by sequential extraction of CO2. *The Holocene*, *17*(1), 131–137. https://doi.org/10.1177/0959683607073295

Bowman, D. (1971). Geomorphology of the shore terraces of the late Pleistocene Lisan Lake (Israel). *Palaeogeography, Palaeoclimatology, Palaeoecology*, *9*(3), 183–209. https://doi.org/10.1016/0031-0182(71)90031-9

Bowman, D., & Gross, T. (1992). The highest stand of Lake Lisan:∼ 150 meter below MSL. *Israel Journal of Earth-Sciences*, *41*(2–4), 233–237.

Brock, F., Higham, T., Ditchfield, P., & Ramsey, C. B. (2010). Current pretreatment methods for AMS radiocarbon dating at the Oxford radiocarbon Accelerator Unit (ORAU). *Radiocarbon*, *52*(1), 103–112. https://doi.org/10.1017/s0033822200045069

Buchbinder, B. (1981). Morphology, microfabric and origin of stromatolites of the Pleistocene precursor of the Dead Sea, Israel, In C. M. (Ed.), *Phanerozoic stromatolites*, (pp. 181–196). Springer-Verlag.

Buchbinder, B., Begin, Z. B., & Friedman, G. M. (1974). Pleistocene algal tufa of lake Lisan, Dead Sea area, Israel. *Israel Journal of Earth Sciences*, *23*, 131–138.

Cheng, H., Edwards, R. L., Hoff, J., Gallup, C. D., Richards, D., & Asmerom, Y. (2000). The half-lives of uranium-234 and thorium-230. *Chemical Geology*, *169*(1–2), 17–33. https://doi.org/10.1016/s0009-2541(99)00157-6

Chiba, T., Sugihara, S., Matsushima, Y., Arai, Y., & Endo, K. (2020). Crustal subsidence inferred from reconstruction of the Pleistocene–Holocene palaeogeography in the northern Lake Inba area, central Japan. *Quaternary Research*, *94*, 61–79. https://doi.org/10.1017/qua.2019.69

Choi, S., Götze, H.-J., Meyer, U., & Group, D. (2011). 3-D density modelling of underground structures and spatial distribution of salt diapirism in the Dead Sea Basin. *Geophysical Journal International*, *184*(3), 1131–1146. https://doi.org/10.1111/j.1365-246x.2011.04939.x

Cohen, A. S., Talbot, M. R., Awramik, S. M., Dettman, D. L., & Abell, P. (1997). Lake level and paleoenvironmental history of Lake Tanganyika, Africa, as inferred from late Holocene and modern stromatolites. *Geological Society of America Bulletin*, *109*(4), 444–460. https://doi.org/10.1130/0016-7606(1997)109<0444:llapho>2.3.co;2

Dupraz, C., Reid, R. P., Braissant, O., Decho, A. W., Norman, R. S., & Visscher, P. T. (2009). Processes of carbonate precipitation in modern microbial mats. *Earth-Science Reviews*, *96*(3), 141–162. https://doi.org/10.1016/j.earscirev.2008.10.005

Emeis, K., Struck, U., Schulz, H., Bernasconi, S., Sakamoto, T., Martinez-Ruiz, F., et al. (2000). Temperature and salinity of Mediterranean sea surface waters over the last 16,000 years: Constraints on the physical environment of S1 sapropel formation based on stable oxygen isotopes and alkenone unsaturation ratios. *Palaeogeography, Palaeoclimatology, Palaeoecology*, *158*(3–4), 259–280. https://doi.org/10.1016/s0031-0182(00)00053-5

Engelhart, S. E., Horton, B. P., & Kemp, A. C. (2011). Holocene sea level changes along the United States' Atlantic Coast. *Oceanography*, *24*(2), 70–79. https://doi.org/10.5670/oceanog.2011.28

Enzel, Y., Amit, R., Dayan, U., Crouvi, O., Kahana, R., Ziv, B., & Sharon, D. (2008). The climatic and physiographic controls of the eastern Mediterranean over the late Pleistocene climates in the southern Levant and its neighboring deserts. *Global and Planetary Change*, *60*(3–4), 165–192. https://doi.org/10.1016/j.gloplacha.2007.02.003

Enzel, Y., Bookman, R., Sharon, D., Gvirtzman, H., Dayan, U., Ziv, B., & Stein, M. (2003). Late Holocene climates of the Near East deduced from Dead Sea level variations and modern regional winter rainfall. *Quaternary Research*, *60*(3), 263–273. https://doi.org/10.1016/j.yqres.2003.07.011

Ferry, M., Meghraoui, M., Karaki, N. A., Al-Taj, M., Amoush, H., Al-Dhaisat, S., & Barjous, M. (2007). A 48-kyr-long slip rate history for the Jordan Valley segment of the Dead Sea Fault. *Earth and Planetary Science Letters*, *260*(3), 394–406. https://doi.org/10.1016/j.epsl.2007.05.049

Frumkin, A. (1996). Uplift rate relative to base-levels of a salt diapir (Dead Sea basin, Israel) as indicated by cave levels. *Geological Society, London, Special Publications*, *100*(1), 41–47. https://doi.org/10.1144/gsl.sp.1996.100.01.04

Frumkin, A. (2001). The cave of the Letters sediments—Indication of an early phase of the Dead Sea depression? *The Journal of Geology*, *109*(1), 79–90. https://doi.org/10.1086/317962

Frumkin, A. (2009). Formation and dating of a salt pillar in Mount Sedom diapir, Israel. *Geological Society of America Bulletin*, *121*(1–2), 286–293. https://doi.org/10.1130/B26376.1

Frumkin, A., & Fischhendler, I. (2005). Morphometry and distribution of isolated caves as a guide for phreatic and confined paleohydrological conditions. *Geomorphology*, *67*(3–4), 457–471. https://doi.org/10.1016/j.geomorph.2004.11.009

Frumkin, A., Ford, D. C., & Schwarcz, H. P. (1999). Continental oxygen isotopic record of the last 170,000 years in Jerusalem. *Quaternary Research*, *51*(3), 317–327. https://doi.org/10.1006/qres.1998.2031

Frumkin, A., & Stein, M. (2004). The Sahara–East Mediterranean dust and climate connection revealed by strontium and uranium isotopes in a Jerusalem speleothem. *Earth and Planetary Science Letters*, *217*(3–4), 451–464. https://doi.org/10.1016/s0012-821x(03)00589-2

Gardosh, M., Reches, Z. e., & Garfunkel, Z. (1990). Holocene tectonic deformation along the western margins of the Dead Sea. *Tectonophysics*, *180*(1), 123–137. https://doi.org/10.1016/0040-1951(90)90377-k

Garfunkel, Z. (1981). Internal structure of the Dead Sea leaky transform (rift) in relation to plate kinematics. *Tectonophysics*, *80*(1–4), 81–108. https://doi.org/10.1016/0040-1951(81)90143-8

Garrett, E., Melnick, D., Dura, T., Cisternas, M., Ely, L. L., Wesson, R. L., et al. (2020). Holocene relative sea-level change along the tectonically active Chilean coast. *Quaternary Science Reviews*, *236*, 106281. https://doi.org/10.1016/j.quascirev.2020.106281

Gat, J. R. (1984). The stable isotope composition of Dead Sea waters. *Earth and Planetary Science Letters*, *71*(2), 361–376. https://doi.org/10.1016/0012-821x(84)90103-1

Ghazleh, S. A., & Kempe, S. (2009). Geomorphology of lake Lisan terraces along the eastern coast of the Dead Sea, Jordan. *Geomorphology*, *108*(3), 246–263. https://doi.org/10.1016/j.geomorph.2009.02.015

Gilbert, G. (1890). Geological Survey Monograph. (438 p).

Green, P. J., & Silverman, B. W. (1993). *Nonparametric regression and generalized linear models: A roughness penalty approach*. Crc Press.

Haase-Schramm, A., Goldstein, S. L., & Stein, M. (2004). U-Th dating of Lake Lisan (late Pleistocene Dead Sea) aragonite and implications for glacial East Mediterranean climate change. *Geochimica et Cosmochimica Acta*, *68*(5), 985–1005. https://doi.org/10.1016/j.gca.2003.07.016

Hall, J. K. (1997). Topography and bathymetry of the Dead Sea depression: Oxford monographs on geology and geophysics, v. *36*, p. 11–21.

Häusler, S., Weber, M., de Beer, D., & Ionescu, D. (2014). Spatial distribution of diatom and cyanobacterial mats in the Dead Sea is determined by response to rapid salinity fluctuations. *Extremophiles*, *18*(6), 1085–1094. https://doi.org/10.1007/s00792-014-0686-1

Hazan, N., Stein, M., Agnon, A., Marco, S., Nadel, D., Negendank, J. F., et al. (2005). The late quaternary limnological history of Lake Kinneret (Sea of Galilee), Israel. *Quaternary Research*, *63*(1), 60–77. https://doi.org/10.1016/j.yqres.2004.09.004

Horton, B. P., Engelhart, S. E., Hill, D. F., Kemp, A. C., Nikitina, D., Miller, K. G., & Peltier, W. R. (2013). Influence of tidal-range change and sediment compaction on Holocene relative sea-level change in New Jersey, USA. *Journal of Quaternary Science*, *28*(4), 403–411. https://doi.org/10.1002/jqs.2634

Huntington, E. (1911). *Palestine and its Transformation*. Houghton Mifflin, p. 443.

Ionescu, D., Siebert, C., Polerecky, L., Munwes, Y. Y., Lott, C., Häusler, S., et al. (2012). Microbial and chemical characterization of underwater fresh water springs in the Dead Sea. *PLoS One*, *7*(6), e38319. https://doi.org/10.1371/journal.pone.0038319

Jara-Muñoz, J. (2023). Lake-level reconstruction during the transition between paleolake-Lisan and Dead Sea (1.0). *Zenodo*. https://doi.org/10.5281/zenodo.7568096

Kafri, U., & Yechieli, Y. (2010). The role of hydrogeological base level in the formation of sub-horizontal caves horizons, example from the Dead Sea Basin, Israel. *Environmental Earth Sciences*, *61*(6), 1145–1152. https://doi.org/10.1007/s12665-009-0435-4

Kallel, N., Paterne, M., Labeyrie, L., Duplessy, J.-C., & Arnold, M. (1997). Temperature and salinity records of the Tyrrhenian Sea during the last 18,000 years. *Palaeogeography, Palaeoclimatology, Palaeoecology*, *135*(1–4), 97–108. https://doi.org/10.1016/s0031-0182(97)00021-7

Katz, A., Kolodny, Y., & Nissenbaum, A. (1977). The geochemical evolution of the Pleistocene lake Lisan-Dead Sea system. *Geochimica et Cosmochimica Acta*, *41*(11), 1609–1626. https://doi.org/10.1016/0016-7037(77)90172-7

Katz, A., & Starinsky, A. (2009). Geochemical history of the Dead Sea. *Aquatic Geochemistry*, *15*(1–2), 159–194. https://doi.org/10.1007/s10498-008-9045-0

Kaufman, A. (1971). U-series dating of Dead Sea basin carbonates. *Geochimica et Cosmochimica Acta*, *35*(12), 1269–1281. https://doi.org/10.1016/0016-7037(71)90115-3

Kaufman, A., Yechieli, Y., & Gardosh, M. (1992). Reevaluation of the Lake-sediment chronology in the Dead Sea basin, Israel, based on new 230 Th/U dates. *Quaternary Research*, *38*(3), 292–304. https://doi.org/10.1016/0033-5894(92)90039-I

Keinan, J., Bar-Matthews, M., Ayalon, A., Zilberman, T., Agnon, A., & Frumkin, A. (2019). Paleoclimatology of the levant from Zalmon cave speleothems, the northern Jordan Valley, Israel. *Quaternary Science Reviews*, *220*, 142–153. https://doi.org/10.1016/j.quascirev.2019.07.018

Kiro, Y., Goldstein, S. L., Garcia-Veigas, J., Levy, E., Kushnir, Y., Stein, M., & Lazar, B. (2017). Relationships between lake-level changes and water and salt budgets in the Dead Sea during extreme aridities in the Eastern Mediterranean. *Earth and Planetary Science Letters*, *464*, 211–226. https://doi.org/10.1016/j.epsl.2017.01.043

Klinger, Y., Avouac, J., Karaki, N. A., Dorbath, L., Bourles, D., & Reyss, J. (2000). Slip rate on the Dead Sea transform fault in northern Araba valley (Jordan). *Geophysical Journal International*, *142*(3), 755–768. https://doi.org/10.1046/j.1365-246x.2000.00165.x

Kolodny, Y., Stein, M., & Machlus, M. (2005). Sea-rain-lake relation in the last glacial east Mediterranean revealed by δ18O-δ13C in Lake Lisan aragonites. *Geochimica et Cosmochimica Acta*, *69*(16), 4045–4060. https://doi.org/10.1016/j.gca.2004.11.022

Kronfeld, J., Ilani, S., & Strull, A. (1991). Radium precipitation and extreme 238U-series disequilibrium along the Dead Sea coast, Israel. *Applied Geochemistry*, *6*(3), 355–361. https://doi.org/10.1016/0883-2927(91)90011-d

Kushnir, Y., & Stein, M. (2010). North Atlantic influence on 19th - 20th century rainfall in the Dead Sea watershed, teleconnections with the Sahel, and implication for Holocene climate fluctuations. *Quaternary Science Reviews*, *29*(27), 3843–3860. https://doi.org/10.1016/j.quascirev.2010.09.004

Lazar, B., Sivan, O., Yechieli, Y., Levy, E., Antler, G., Gavrieli, I., & Stein, M. (2014). Long-term freshening of the Dead Sea brine revealed by porewater Cl- and in ICDP Dead Sea deep-drill. *Earth and Planetary Science Letters*, *400*, 94–101. https://doi.org/10.1016/j.epsl.2014.03.019

Lazar, M., Ben-Avraham, Z., & Schattner, U. (2006). Formation of sequential basins along a strike-slip fault, Geophysical observations from the Dead Sea basin. *Tectonophysics*, *421*(1), 53–69. https://doi.org/10.1016/j.tecto.2006.04.007

Leng, M. J., & Marshall, J. D. (2004). Palaeoclimate interpretation of stable isotope data from lake sediment archives. *Quaternary Science Reviews*, *23*(7–8), 811–831. https://doi.org/10.1016/j.quascirev.2003.06.012

Lensky, N., Dvorkin, Y., Lyakhovsky, V., Gertman, I., & Gavrieli, I. (2005). Water, salt, and energy balances of the Dead Sea. *Water Resources Research*, *41*(12). https://doi.org/10.1029/2005wr004084

Lev, L., Stein, M., Ito, E., Fruchter, N., Ben-Avraham, Z., & Almogi-Labin, A. (2019). Sedimentary, geochemical and hydrological history of Lake Kinneret during the past 28,000 years. *Quaternary Science Reviews*, *209*, 114–128. https://doi.org/10.1016/j.quascirev.2019.02.015

Li, H.-C., & Ku, T.-L. (1997). δ13C–δ18C covariance as a paleohydrological indicator for closed-basin lakes. *Palaeogeography, Palaeoclimatology, Palaeoecology*, *133*(1–2), 69–80. https://doi.org/10.1016/s0031-0182(96)00153-8

Lisker, S., Vaks, A., Bar-Matthews, M., Porat, R., & Frumkin, A. (2009). Stromatolites in caves of the Dead Sea Fault escarpment: Implications to latest Pleistocene lake levels and tectonic subsidence. *Quaternary Science Reviews*, *28*(1), 80–92. https://doi.org/10.1016/j.quascirev.2008.10.015

Lougheed, B., & Obrochta, S. (2016). MatCal: Open source Bayesian 14 C age calibration in MatLab. *Journal of Open Research Software*, *4*(1), 42. https://doi.org/10.5334/jors.130

Lu, Y., Bookman, R., Waldmann, N., & Marco, S. (2020). A 45 kyr laminae record from the Dead Sea: Implications for basin erosion and floods recurrence. *Quaternary Science Reviews*, *229*, 106143. https://doi.org/10.1016/j.quascirev.2019.106143

Lu, Y., Moernaut, J., Waldmann, N., Bookman, R., Ian Alsop, G., Hubert-Ferrari, A., et al. (2021). Orbital-and millennial-scale changes in Lake-levels facilitate earthquake-Triggered mass Failures in the Dead Sea basin. *Geophysical Research Letters*, *48*(14), e2021GL093391. https://doi.org/10.1029/2021gl093391

Machlus, M., Enzel, Y., Goldstein, S. L., Marco, S., & Stein, M. (2000). Reconstructing low levels of Lake Lisan by correlating fan-delta and lacustrine deposits. *Quaternary International*, *73*, 137–144. https://doi.org/10.1016/s1040-6182(00)00070-7

Mackey, T., Sumner, D., Hawes, I., Leidman, S., Andersen, D., & Jungblut, A. D. (2018). Stromatolite records of environmental change in perennially ice-covered Lake Joyce, McMurdo Dry Valleys, Antarctica. *Biogeochemistry*, *137*(1), 73–92. https://doi.org/10.1007/s10533-017-0402-1

Marco, S., Stein, M., Agnon, A., & Ron, H. (1996). Long-term earthquake clustering: A 50,000-year paleoseismic record in the Dead Sea Graben. *Journal of Geophysical Research*, *101*(B3), 6179–6191. https://doi.org/10.1029/95jb01587

Marco, S., Weinberger, R., & Agnon, A. (2002). Radial fractures formed by a salt stock in the Dead Sea Rift, Israel. *Terra Nova*, *14*(4), 288–294. https://doi.org/10.1046/j.1365-3121.2002.00423.x

Masson, F., Hamiel, Y., Agnon, A., Klinger, Y., & Deprez, A. (2015). Variable behavior of the Dead Sea Fault along the southern Arava segment from GPS measurements. *Comptes Rendus Geoscience*, *347*(4), 161–169. https://doi.org/10.1016/j.crte.2014.11.001

McCormack, J., Nehrke, G., Jöns, N., Immenhauser, A., & Kwiecien, O. (2019). Refining the interpretation of lacustrine carbonate isotope records: Implications of a mineralogy-specific Lake Van case study. *Chemical Geology*, *513*, 167–183. https://doi.org/10.1016/j.chemgeo.2019.03.014

McGee, D., Quade, J., Edwards, R. L., Broecker, W. S., Cheng, H., Reiners, P. W., & Evenson, N. (2012). Lacustrine cave carbonates: Novel archives of paleohydrologic change in the Bonneville Basin (Utah, USA). *Earth and Planetary Science Letters*, *351*, 182–194. https://doi.org/10.1016/j.epsl.2012.07.019

Mechie, J., Abu-Ayyash, K., Ben-Avraham, Z., El-Kelani, R., Mohsen, A., Rümpker, G., et al. (2005). Crustal shear velocity structure across the Dead Sea Transform from two-dimensional modelling of DESERT project explosion seismic data. *Geochemistry, Geophysics, Geosystems*, *160*(3), 910–924. https://doi.org/10.1111/j.1365-246x.2005.02526.x

Miebach, A., Stolzenberger, S., Wacker, L., Hense, A., & Litt, T. (2019). A new Dead Sea pollen record reveals the last glacial paleoenvironment of the southern Levant. *Quaternary Science Reviews*, *214*, 98–116. https://doi.org/10.1016/j.quascirev.2019.04.033

Migowski, C., Stein, M., Prasad, S., Negendank, J. F., & Agnon, A. (2006). Holocene climate variability and cultural evolution in the Near East from the Dead Sea sedimentary record. *Quaternary Research*, *66*(3), 421–431. https://doi.org/10.1016/j.yqres.2006.06.010

Morin, E., Ryb, T., Gavrieli, I., & Enzel, Y. (2019). Mean, variance, and trends of Levant precipitation over the past 4500 years from reconstructed Dead Sea levels and stochastic modeling. *Quaternary Research*, *91*(2), 751–767. https://doi.org/10.1017/qua.2018.98

Neev, D., & Emery, K. O. (1967). *The Dead Sea: Depositional processes and environments of evaporites* (Vol. 41, p. 147). Bulletin of the Geological Survey of Israel.

Neev, D., & Langozky, Y. (1961). Tufa deposits (algal bioherms?) of the Lisan Lake. In *Proceedings Symposium on the Pleistocene in Israel. Association for the Advancement of Science in Israel* (pp. 10–11). The Hebrew University.

Neugebauer, I., Brauer, A., Schwab, M. J., Waldmann, N. D., Enzel, Y., Kitagawa, H., et al. (2014). Lithology of the long sediment record recovered by the ICDP Dead Sea deep Drilling project (DSDDP). *Quaternary Science Reviews*, *102*, 149–165. https://doi.org/10.1016/j.quascirev.2014.08.013

Niemi, T. M. (1997). Fluctuations of Late Pleistocene lake Lisan in the Dead Sea rift. *Oxford Monographs on Geology and Geophysics*, *36*, 226–236.

Nof, R. N., Ziv, A., Doin, M.-P., Baer, G., Fialko, Y., Wdowinski, S., et al. (2012). Rising of the lowest place on Earth due to Dead Sea water-level drop: Evidence from SAR interferometry and GPS. *Journal of Geophysical Research*, *117*, B5. https://doi.org/10.1029/2011jb008961

Oren, A., & Shilo, M. (1982). Population dynamics of Dunaliella parva in the Dead Sea. *Limnology & Oceanography*, *27*(2), 201–211. https://doi.org/10.4319/lo.1982.27.2.0201

Osmond, J., May, J. P., & Tanner, W. (1970). Age of the Cape Kennedy Barrier-and-Lagoon complex. *Journal of Geophysical Research*, *75*(2), 469–479. https://doi.org/10.1029/jb075i002p00469

Pérez-Gussinyé, M., Metois, M., Fernández, M., Vergés, J., Fullea, J., & Lowry, A. (2009). Effective elastic thickness of Africa and its relationship to other proxies for lithospheric structure and surface tectonics. *Earth and Planetary Science Letters*, *287*(1–2), 152–167. https://doi.org/10.1016/j.epsl.2009.08.004

Petrunin, A. G., Meneses Rioseco, E., Sobolev, S. V., & Weber, M. (2012). Thermomechanical model reconciles contradictory geophysical observations at the Dead Sea Basin. *Geochemistry, Geophysics, Geosystems*, *13*(4). https://doi.org/10.1029/2011gc003929

Petryshyn, V. A., Rivera, M. J., Agić, H., Frantz, C. M., Corsetti, F. A., & Tripati, A. E. (2016). Stromatolites in Walker Lake (Nevada, Great Basin, USA) record climate and lake level changes∼ 35,000 years ago. *Palaeogeography, Palaeoclimatology, Palaeoecology*, *451*, 140–151. https://doi.org/10.1016/j.palaeo.2016.02.054

Picard, L. (1943). Structure and evolution of Palestine: Bulletin of the geological Department Hebrew University, Jerusalem, *4*(2–3), 187.

Prasad, S., Negendank, J. F., & Stein, M. (2009). Varve counting reveals high resolution radiocarbon reservoir age variations in palaeolake Lisan. *Journal of Quaternary Science: Published for the Quaternary Research Association*, *24*(7), 690–696. https://doi.org/10.1002/jqs.1289

Prasad, S., Vos, H., Negendank, J. F., Waldmann, N., Goldstein, S. L., & Stein, M. (2004). Evidence from Lake Lisan of solar influence on decadal-to centennial-scale climate variability during marine oxygen isotope stage 2: Geology. *Geology*, *32*(7), 581–584. https://doi.org/10.1130/g20553.1

Reimer, P. J. (2020). Composition and consequences of the IntCal20 radiocarbon calibration curve. *Quaternary Research*, *96*, 22–27. https://doi.org/10.1017/qua.2020.42

Riding, R. (1991). *Classification of microbial carbonates, Calcareous algae and stromatolites* (pp. 21–51). Springer-Verlag.

Riding, R. (1999). The term stromatolite: Towards an essential definition. *Lethaia*, *32*(4), 321–330. https://doi.org/10.1111/j.1502-3931.1999.tb00550.x

Robinson, S. A., Black, S., Sellwood, B. W., & Valdes, P. J. (2006). A review of palaeoclimates and palaeoenvironments in the levant and eastern Mediterranean from 25,000 to 5000 years BP: Setting the environmental background for the evolution of human civilisation. *Quaternary Science Reviews*, *25*(13–14), 1517–1541. https://doi.org/10.1016/j.quascirev.2006.02.006

Rosholt, J. (1976). *230TH/234U dating of travertine and caliche rinds* (Vol. 8, p. 1076). Geolological Society America Abstracts with Programs.
Schramm, A., Stein, M., & Goldstein, S. L. (2000). Calibration of the 14 C time scale to> 40 ka by 234 U, 230 Th dating of Lake Lisan sediments (last glacial Dead Sea). *Earth and Planetary Science Letters*, *175*(1), 27–40. https://doi.org/10.1016/s0012-821x(99)00279-4
Sharon, M., Sagy, A., Kurzon, I., Marco, S., Ben-Avraham, Z., & Rosensaft, M. (2018). *Quaternary fault map of Israel*. Geological Survey of Israel.
Shennan, I. (1986). Flandrian sea-level changes in the Fenland. II: Tendencies of sea-level movement, altitudinal changes, and local and regional factors. *Journal of Quaternary Science*, *1*(2), 155–179. https://doi.org/10.1002/jqs.3390010205
Soulet, G. (2015). Methods and codes for reservoir–atmosphere 14C age offset calculations. *Quaternary Geochronology*, *29*, 97–103. https://doi.org/10.1016/j.quageo.2015.05.023
Stanford, J. D., Hemingway, R., Rohling, E. J., Challenor, P. G., Medina-Elizalde, M., & Lester, A. (2011). Sea-Level probability for the last deglaciation: A statistical analysis of far-field records. *Global and Planetary Change*, *79*(3–4), 193–203. https://doi.org/10.1016/j.gloplacha.2010.11.002
Stein, M. (2001). The sedimentary and geochemical record of Neogene-Quaternary water bodies in the Dead Sea Basin-inferences for the regional paleoclimatic history. *Journal of Paleolimnology*, *26*(3), 271–282. https://doi.org/10.1023/a:1017529228186
Stein, M., Migowski, C., Bookman, R., & Lazar, B. (2004). Temporal changes in radiocarbon reservoir age in the Dead Sea-Lake Lisan system. *Radiocarbon*, *46*(2), 649–655. https://doi.org/10.1017/s0033822200035700
Stein, M., Starinsky, A., Katz, A., Goldstein, S. L., Machlus, M., & Schramm, A. (1997). Strontium isotopic, chemical, and sedimentological evidence for the evolution of Lake Lisan and the Dead Sea. *Geochimica et Cosmochimica Acta*, *61*(18), 3975–3992. https://doi.org/10.1016/s0016-7037(97)00191-9
Steinberg, J., Gvirtzman, Z., & Garfunkel, Z. (2014). Flexural response of a continental margin to sedimentary loading and lithospheric rupturing: The mountain ridge between the Levant Basin and the Dead Sea Transform. *Tectonics*, *33*(2), 166–186. https://doi.org/10.1002/2013tc003330
Street-Perrott, F. A., & Perrott, R. A. (1990). Abrupt climate fluctuations in the tropics: The influence of Atlantic ocean circulation. *Nature*, *343*(6259), 607–612. https://doi.org/10.1038/343607a0
Stuiver, M., Pearson, G. W., & Braziunas, T. (1986). Radiocarbon age calibration of marine samples back to 9000 cal yr BP. *Radiocarbon*, *28*(2B), 980–1021. https://doi.org/10.1017/s0033822200060264
Talbot, M. (1990). A review of the palaeohydrological interpretation of carbon and oxygen isotopic ratios in primary lacustrine carbonates. *Chemical Geology: Isotope Geoscience section*, *80*(4), 261–279. https://doi.org/10.1016/0168-9622(90)90009-2
Talma, A., Vogel, J., & Stiller, M. (1997). The radiocarbon content of the Dead Sea: Oxford monographs on geology and geophysics, *36*(1), 193–198.
Thomas, C., Ebert, Y., Kiro, Y., Stein, M., Ariztegui, D., & Record, D. S. T. J. T. D. (2016). Microbial sedimentary imprint on the deep Dead Sea sediment. *The Depositional Record*, *2*(1), 118–138. https://doi.org/10.1002/dep2.16
Torfstein, A., & Enzel, Y. (2017). *Dead Sea lake level changes and levant palaeoclimate, Quaternary of the Levant-environments, climate change, and Humans* (pp. 115–126). Cambridge University Press.
Torfstein, A., Gavrieli, I., Katz, A., Kolodny, Y., & Stein, M. (2008). Gypsum as a monitor of the paleo-limnological–hydrological conditions in Lake Lisan and the Dead Sea. *Geochimica et Cosmochimica Acta*, *72*(10), 2491–2509. https://doi.org/10.1016/j.gca.2008.02.015
Torfstein, A., Gavrieli, I., & Stein, M. (2005). The sources and evolution of sulfur in the hypersaline Lake Lisan (paleo-Dead Sea). *Earth and Planetary Science Letters*, *236*(1–2), 61–77. https://doi.org/10.1016/j.epsl.2005.04.026
Torfstein, A., Goldstein, S. L., Kagan, E. J., & Stein, M. (2013). Integrated multi-site U/Th chronology of the last glacial Lake Lisan. *Geochimica et Cosmochimica Acta*, *104*, 210–231. https://doi.org/10.1016/j.gca.2012.11.003
Torfstein, A., Goldstein, S. L., Kushnir, Y., Enzel, Y., Haug, G., & Stein, M. (2015). Dead Sea drawdown and monsoonal impacts in the Levant during the last interglacial. *Earth and Planetary Science Letters*, *412*, 235–244. https://doi.org/10.1016/j.epsl.2014.12.013
Torfstein, A., Goldstein, S. L., Stein, M., & Enzel, Y. (2013). Impacts of abrupt climate changes in the levant from last glacial Dead Sea levels. *Quaternary Science Reviews*, *69*, 1–7. https://doi.org/10.1016/j.quascirev.2013.02.015
Torfstein, A., Haase-Schramm, A., Waldmann, N., Kolodny, Y., & Stein, M. (2009). U-series and oxygen isotope chronology of the mid-Pleistocene Lake Amora (Dead Sea basin). *Geochimica et Cosmochimica Acta*, *73*(9), 2603–2630. https://doi.org/10.1016/j.gca.2009.02.010
Vaks, A., Bar-Matthews, M., Ayalon, A., Matthews, A., Frumkin, A., Dayan, U., et al. (2006). Paleoclimate and location of the border between Mediterranean climate region and the Saharo–Arabian Desert as revealed by speleothems from the northern Negev Desert, Israel. *Earth and Planetary Science Letters*, *249*(3–4), 384–399. https://doi.org/10.1016/j.epsl.2006.07.009
Vaks, A., Bar-Matthews, M., Ayalon, A., Schilman, B., Gilmour, M., Hawkesworth, C. J., et al. (2003). Paleoclimate reconstruction based on the timing of speleothem growth and oxygen and carbon isotope composition in a cave located in the rain shadow in Israel. *Quaternary Research*, *59*(2), 182–193. https://doi.org/10.1016/s0033-5894(03)00013-9
Van der Borg, K., Stein, M., de Jong, A., Waldmann, N., & Goldstein, S. (2004). Near-zero $\Delta^{14}C$ values at 32 kyr cal BP observed in the high-resolution ^{14}C record from U-Th dated sediment of lake Lisan. *Radiocarbon*, *46*(2), 785–795. https://doi.org/10.1017/s0033822200035827
Ventsel, E., Krauthammer, T., & Carrera, E. (2002). Thin plates and shells: Theory, analysis, and applications. *Applied Mechanics Reviews*, *55*(4), B72–B73. https://doi.org/10.1115/1.1483356
Waldmann, N., Starinsky, A., & Stein, M. (2007). Primary carbonates and Ca-chloride brines as monitors of a paleo-hydrological regime in the Dead Sea basin. *Quaternary Science Reviews*, *26*(17–18), 2219–2228. https://doi.org/10.1016/j.quascirev.2007.04.019
Waldmann, N., Stein, M., Ariztegui, D., & Starinsky, A. (2009). Stratigraphy, depositional environments and level reconstruction of the last interglacial Lake Samra in the Dead Sea basin. *Quaternary Research*, *72*(1), 1–15. https://doi.org/10.1016/j.yqres.2009.03.005
Waldmann, N., Torfstein, A., & Stein, M. (2010). Northward intrusions of low-and mid-latitude storms across the Saharo-Arabian belt during past interglacials. *Geology*, *38*(6), 567–570. https://doi.org/10.1130/g30654.1
Walter, M. R. (1976). *Introduction, developments in sedimentology* (Vol. 20, pp. 1–3). Elsevier. https://doi.org/10.1016/s0070-4571(08)71123-3
Wefing, A.-M., Arps, J., Blaser, P., Wienberg, C., Hebbeln, D., & Frank, N. (2017). High precision U-series dating of scleractinian cold-water corals using an automated chromatographic U and Th extraction. *Chemical Geology*, *475*, 140–148. https://doi.org/10.1016/j.chemgeo.2017.10.036
Weinberger, R., Begin, Z., Waldmann, N., Gardosh, M., Baer, G., Frumkin, A., & Wdowinski, S. (2006). *Quaternary rise of the sedom diapir, Dead Sea basin* (Vol. 401, p. 33). Geological Society of America Special Papers. https://doi.org/10.1130/2006.2401(03)
Weinberger, R., Lyakhovsky, V., Baer, G., & Begin, Z. (2006). Mechanical modeling and InSAR measurements of Mount Sedom uplift, Dead Sea basin: Implications for effective viscosity of rock salt. *Geochemistry, Geophysics, Geosystems*, *7*(5). https://doi.org/10.1029/2005gc001185

Wetzler, N., Sagy, A., & Marco, S. (2014). The association of micro-earthquake clusters with mapped faults in the Dead Sea basin. *Journal of Geophysical Research: Solid Earth*, *119*(11), 8312–8330. https://doi.org/10.1002/2013jb010877

Wetzler, N., Sagy, A., Sagy, Y., Nahmias, Y., & Lyakhovsky, V. (2015). Active transform fault zone at the fringe of the Dead Sea Basin. *Tectonics*, *34*(7), 1475–1493. https://doi.org/10.1002/2015tc003827

Zak, I. (1967). *The geology of the sedom mountain [Ph. D. Thesis]*. The Hebrew University.

Zucker, E., Frumkin, A., Agnon, A., & Weinberger, R. (2019). Internal deformation and uplift-rate of salt walls detected by a displaced dissolution surface, Dead Sea basin. *Journal of Structural Geology*, *127*, 103870. https://doi.org/10.1016/j.jsg.2019.103870